Iron Garnet Thin Films for Integrated Photonics and Spintronics

By

Takian Fakhrul

B.S. and M.S. in Materials and Metallurgical Engineering
Bangladesh University of Engineering and Technology (2014)

Submitted to the Department of Materials Science and Engineering
in partial fulfillment of the requirements for the degree of

Doctor of Philosophy in Materials Science and Engineering

at the

Massachusetts Institute of Technology

February 2022

Signature of author_____
Department of Materials Science and Engineering
December 21st, 2021

Certified by_____
Caroline A. Ross
Toyota Professor of Materials Science and Engineering
Thesis Supervisor

Accepted by_____
Frances M. Ross
Ellen Swallow Richards Professor in Materials Science and Engineering
Chair, Departmental Committee on Graduate Studies

This thesis is dedicated to the two most important ladies in my life:

Ammu, the person behind all my small and big achievements

& Aaveen, for inspiring me to be a better version of myself every day.

Iron Garnet Thin Films for Integrated Photonics and Spintronics

by
Takian Fakhrul

Submitted to the Department of Materials Science and Engineering
on Dec 21st, 2022, in Partial Fulfillment of the
Requirements for the Degree of Doctor of Philosophy
in Materials Science and Engineering

Abstract

In pursuit of beyond CMOS computing, this thesis aims to provide material solutions for both photonic interconnects and ultra-fast spintronic memory. Iron garnet thin films are uniquely suited for both applications as they have: 1) strong magneto-optic (MO) response and low optical absorption at communication wavelengths making them enablers for nonreciprocal devices essential in photonic integrated circuits. 2) Low Gilbert damping and perpendicular anisotropy (PMA) that promote fast DW dynamics making them exciting candidates for next generation spintronic memory.

We first study polycrystalline in-plane magnetized iron garnets for optical isolation. The first successful demonstration of top-down crystallized polycrystalline BiYIG/YIG films on Si exhibit a record high MO figure of merit (FoM) of up to 770° dB^{-1} at 1550 nm wavelength. Growth of single phase BiYIG on the sidewalls of waveguides is also demonstrated, which can be used in transverse electric-mode devices. $Tb_3Fe_5O_{12}$ (TbIG), CeTbIG, and BiTbIG films are grown directly on Si substrates without any seed layers. The Faraday rotation at 1550 nm of the $Bi_{0.03}$TbIG films is 6200 ± 300° cm^{-1}, which is the highest reported for polycrystalline films, and absorption can be engineered by composition control that may reduce Fe^{2+} and Tb^{4+} absorption pathways. We then study single crystal BiYIG with PMA and ultra-low Gilbert damping in the order 1.3×10^{-4} . These films exhibit record spin-orbit torque-driven domain wall (DW) velocities of up to 4300 m/s, but require an in-plane field. We show that Dzyaloshinskii–Moriya interaction (DMI) can be introduced in heterostructures of BiYIG and TmIG and report the first proof-of-concept of field-free current induced DW motion in Pt/BiYIG/TmIG stacks, as well as formation of room temperature skyrmions.

Thesis Supervisor: Caroline A. Ross
Title: Toyota Professor of Materials Science and Engineering

Acknowledgements

The 6 years I spent at MIT, was one of the most rewarding experiences of my life. In the process of getting a PhD, I worked with and befriended some of the kindest, smartest and most extraordinary people in the world. The research I present in this thesis is the culmination of the efforts and contribution from a large group of people who were either involved with my research or my PhD journey while I navigated through MIT.

Firstly, I would like to thank my advisor Professor Caroline A. Ross whose research guidance paved the way for all the work presented in this thesis. I am grateful to her for inviting me into her group with open arms, introducing me to the field of magneto-optics and spintronics and for teaching me most of what I know about magnetic materials and more specifically garnets. She helped me understand the importance of being a careful researcher who asks the right questions and the importance of building useful and impactful things. I would especially like to thank her for the kindness and patience she showed me during my pregnancy and afterwards. Without her unconditional support I would not have been able to complete this PhD while also raising an almost three-year-old toddler.

I am grateful to my thesis committee members Professor Geoffrey Beach and Professor Juejun Hu for their invaluable feedback and collaborations and for asking me hard questions that pushed me to my limits and made me think harder about research problems. I specially thank Prof. Beach for allowing me to work in his labs and collaborate with his students.

I thank my best friends at DMSE: Seong Soon Jo and Yusu Liu for making this PhD so enjoyable. Studying quals was bearable because I got to do it with you, and I am so happy we all made it through. I am especially grateful to Soon who has always looked out for me and stood with me through thick and thin. I will miss coffee breaks at the DMSE lounge with the girls and Eric Fadel and hearing all about the entrance exam at École Polytechnique! A special thanks to the DMSE PhD incoming class of 2015. You were all amazing and bonding with all of you while studying for quals was one of the highlights of my PhD.

Ross group has been a huge part of my PhD and I am grateful for being able to befriend some incredible people who have helped me grow as a researcher. The discussions and collaborations I had with them are responsible for greatly improving the quality of this thesis. I thank Bharat, Ethan, Jackson, Astera, Shuchi, Yabin, Shuai, Eunsoo, Miela, Allison, Edwardo, Lukas, Taichi Goto, Li-Chen Cheng, Kun-Hua Tu and Enno. I will miss our Friday outings to Toscanini's and all the end of semester lunches at (now closed) Kendall Legal Seafoods and Za. I will specially miss all the fun we used to have while attending MMM/Intermag conferences. If any of you want to visit Bangladesh (I personally encourage you to!), I would love to be your host to home of some of the most vibrant and culturally rich cities and the longest sea beach in the world!

I would also like to take the time to thank my collaborators: Prof. Martin Veis for help with ellipsometry. Prof. Luqiao Liu for letting us use his ion miller, MOKE microscope and SMR set-up. Hans Nembach and Justin Shaw from NIST for FMR measurements. Siying Huang for persevering with me on DW motion measurements. We both discovered that Murphy's Law applied to us when it came to research, but it was good to have a partner while I floundered and found myself back again! And Byunghun Lee for BLS measurements.

My work at MIT would have been impossible if it had not been for some amazing staff who trained me to use equipment and helped me troubleshoot. I would like to thank Charlie Settens for teaching me everything I know about XRD equipment, measurements and data fitting. I am grateful to David Bono for all his help with trouble shooting VSM and Faraday measurement problems and letting me use his laser MOKE. I cannot think of a single PhD student in magnetism who got through without crossing paths with this incredibly smart and helpful individual and I am grateful I was able to learn from him. I am grateful to Alan F. Schwartzman for help with AFM analysis and always making time for appointments on short notice. I also thank Libby Shaw for help with XPS and Yong Zhang for TEM. I would also like to thank the MTL and MIT nano staff Kurt Broderick, Dennis Ward and Dave Terry for facilitating my device fabrication processes and for training me on various tools. A special shout out to DMSE graduate administrator Angelita for not only taking care of all the administrative behind the scenes but also for always looking out for me even when it came to ensuring the length of maternity leave, I needed.

A special thanks to MIT BSA and MSA for being a huge part of my life at MIT and for making me feel included in a place that is so far away from home. As a president of BSA I thoroughly enjoyed organizing BSA events with other members and introducing the "Taste of Bangladesh" to the MIT community for the first time ever. I will terribly miss all the folks I met through BSA and our numerous free-food events. A shout out to my Westgate neighbors and road trip partners Usama, Ayesha and Nuwairah. I am also immensely grateful to MIT MSA for hosting iftars and Taraweeh prayers during Ramadan and giving me a sense of community in this special month. I am so grateful that I was able to continue the tradition of praying Taraweeh at the mosque and breaking my Fast without having to worry about what to cook after a long day of fasting and working.

A special thanks to my friends in the greater Boston area: Xisan, Sadi, Proma apu, Farabi bhai, Nazir bhai , Mou and Hasin. These were the people who took care of us through thick and thin and were our shoulder to cry on when my mother-in-law passed away. I will always miss our late night addas and hangouts and all of you will forever have a special place in my heart.

Finally, I would like to thank my family who are the sole reason I am at MIT today. I am grateful to God for giving me parents who have taught me and my sister (Aaveen's Monty) to dream big and encouraged us to work hard to make those dreams come true. I thank my dad for inspiring me to study Materials Science and Ammu for inculcating in me her love for physics. Words fall short to describe all the sacrifices she made to help me chase my dreams and her unwavering support is the reason behind all the achievements in my life.

Last but not the least, I thank my husband, Nadim, for being my best friend at MIT and my go-to person for help with anything and everything. I thank him for teaching me everything I know about Matlab and for helping me troubleshoot problems in both research and life. His contagious passion for science inspires me every day and my journey at MIT would not have been half as fun without him. Above all I thank him for giving me the best gift ever: Aaveen. She is without a shadow of doubt the biggest blessing of our lives and I hope she can someday come back to her birthplace (InshaAllah!). I cannot thank God enough for giving us not only one, but two PhD degrees and one beautiful baby girl after the 6 years or so we spent in this super intense but magical place called MIT. Alhamdulillah!

Table of Contents

1. Motivation

Over the last half a century, microprocessor chips have become smaller, cheaper and more energy efficient and this proliferation has enabled the ubiquitous computing we enjoy today. Since 1965, the semiconductor industry has been governed by Moore's law that predicts the number of transistors in a microprocessor double about every two years, thereby doubling the processing power without increasing the energy consumption. However, with the dramatic scaling in feature sizes, we now face two major roadblocks to achieving faster and cheaper computing:

1) interconnect bottleneck
2) memory architecture causing "memory wall"

In this thesis, we develop materials, namely iron garnets, that will address aspects of both of these bottlenecks. One of the aims of this thesis is to provide material solutions that allows integration of high-performance optical isolators on to chips. The materials of interest for this purpose are polycrystalline Bi substituted yttrium iron garnet (BiYIG) and polycrystalline Bi and Ce substituted terbium iron garnets (BiTbIG, CeTbIG). For spintronic memory, the material system of interest is single crystal BiYIG and Thulium iron garnet (TmIG) heterostructure thin films.

1.1 Interconnect bottleneck

As the chips become smaller and smaller, the wiring between microprocessors becomes more tightly packed which causes difficulties such as heat dissipation due to metal interconnect resistance and signal leakage. As transistors continue to scale down to 7-5nm there is an exponential increase in electrical interconnection time due to RC delay which is known as the "interconnect bottleneck" as shown in Fig. 1-1. [1,2] Further improvement in integrated circuits performance depends not only on individual device performance like transistor gate delay, but rather the ability to swiftly get signals in and out of the microprocessor. The inherent material limitations of metallic interconnects affect the ability of communication solutions based on electronics to transfer high bandwidth data from one place to another in both a fast and power efficient way that keeps pace with Moore's law.

Replacing metallic interconnects with photonics for communication is one promising way to tackle this problem. Silicon photonics is a form of integrated circuit where photonic integrated circuits (PICs) are built on silicon. In these circuits, data is transmitted and moved around the chip via light through waveguides as opposed to electrical signals through copper interconnects. Rapid development in photonic integrated circuit (PIC) technology using silicon waveguides has been made possible by an advanced library of photonic elements including low-loss waveguides, modulators, and photodetectors. These elements serve as building blocks for PICs on chip for applications beyond interconnects [3,4] such as sensing [5], and quantum optics [6] .

In most of the reported work on PICs, an external laser is used with a bulk optical isolator, which limits the size, power consumption, and cost of the product. Optical isolators, that are photonic counterparts of electrical diodes, are key components in PICs because they prevent back-reflected light from adversely affecting and destabilizing the laser and the optical system. Today, integrated optical isolators are still the missing links on semiconductor PICs.[7-13] As photonic integration continues to scale, the need for on-chip isolation becomes more and more imperative, since unwanted reflections between the numerous integrated devices in a PIC can be highly disruptive in a complex optical network. Thus, one of the aims of this thesis is to provide material solutions that allows integration of high-performance optical isolators on to chips. The materials of interest for this purpose are polycrystalline Bi substituted yttrium iron garnet (BiYIG) and polycrystalline Bi and Ce substituted terbium iron garnets (BiTbIG, CeTbIG).

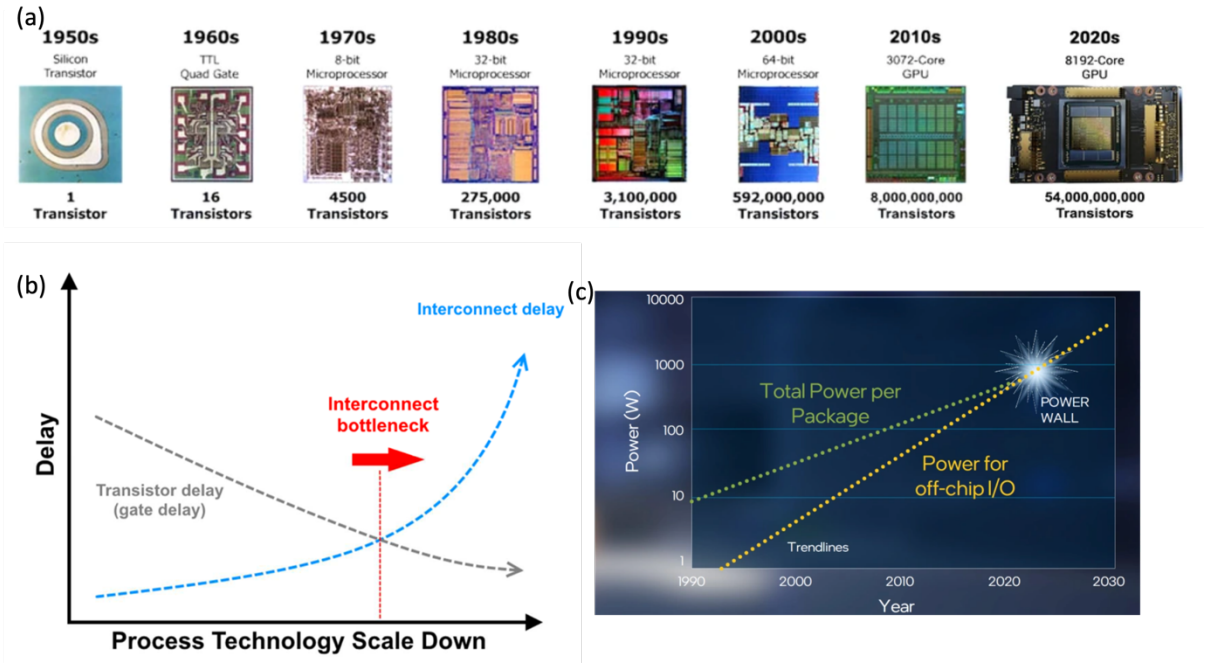

Figure 1-1: *a) Evolution of transistors in computers b) Trends in transistor gate delay (switching time) and interconnect delay with IC fabrication technology. The crossover point represents the start of the "interconnect bottleneck", where photonic interconnects becomes helpful.* [2] *Over time, the power requirements of electrical interconnects are trending larger than the total available socket power.*

1.2 Memory wall

Another critical bottleneck in attaining faster and cheaper computing is what we know as the memory wall. While the actual processors speed (instructions per second) is roughly doubling, the current chip-based memory that is centered on traditional complementary metal oxide semiconductors (CMOS) devices is improving at only about 1.1 times every two years.[14] This result is a gap between processor speed and memory speed that is often called the memory wall [15] as shown in Fig. 1-2.

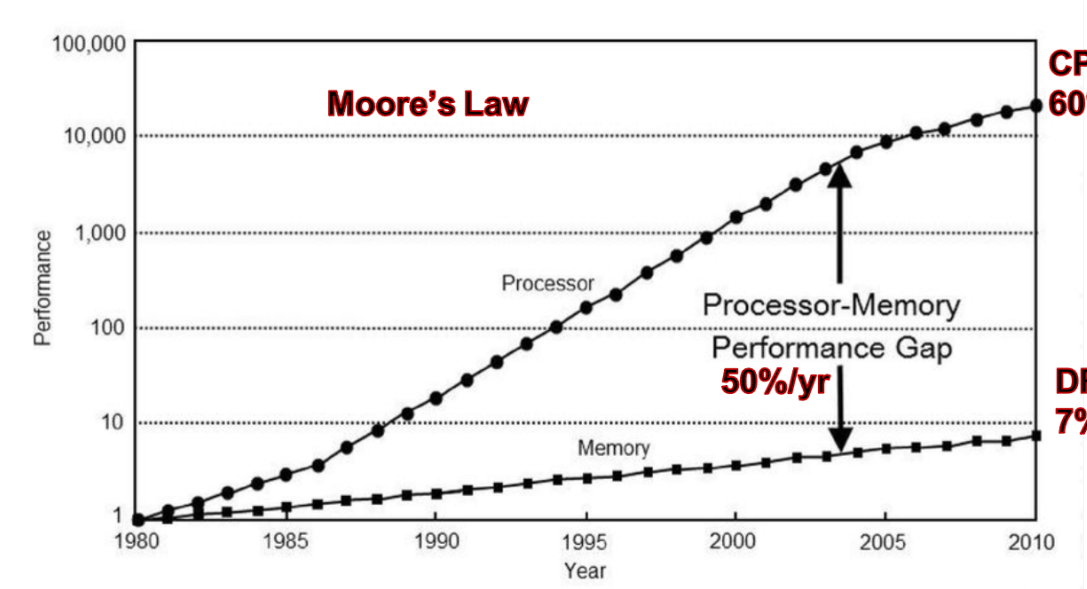

Figure 1-2: *Processor-DRAM memory gap.* [16]

A strong contender emerging to memory based on CMOS chips is spintronics, a technology that works by manipulating the spin of electrons, instead of relying on their charge, to store, control, and read information. Spintronic memory can offer higher computing speeds and storage capacities, at lower power consumption, than conventional CMOS-based memory known as solid-state random access memory (RAM). As magnetic materials are hysteretic in nature, spintronics devices are non-volatile, meaning they retain their magnetic state when powered off, making them ideal for memory devices.

Today's computer architectures rely on two types of data storage, a volatile primary storage (RAM) and a non-volatile secondary storage (hard drive discs, HDD) to obtain a trade-off between cost and performance. Primary storage comprises fast access memories namely, static random access memory (SRAM, 6 transistors and 1 capacitor) and dynamic random access memory (DRAM, 1 transistor and 1 capacitor) and are located close to processors for fast data processing. On the other hand, secondary storage are cheap slow access devices that have high density and are usually located on a separate chip as they are fabricated with a different technology than the processor. The different types of computer memory are shown in Fig. 1-3.

For the past few decades, SRAM and DRAM have been the main workhouses of computer memory where memory is stored in the form of charge in capacitors. As SRAM is static volatile memory it retains its memory while power is supplied. On the other hand, DRAM needs to be

regularly refreshed. SRAM is used in caches because of its speed while DRAM is used for main memory because of its higher densities.

HDDs are non-volatile and inexpensive, but have access times 6 orders of magnitude slower than that of SRAM [17,18]. This kind of memory is limited in its speeds by the requirement to physically move the read/write head with respect to the bit-storing disc. The architecture of computer systems could be drastically improved if there were a single memory device that had the high performance and reliability of solid-state RAM but the low cost of HDD.

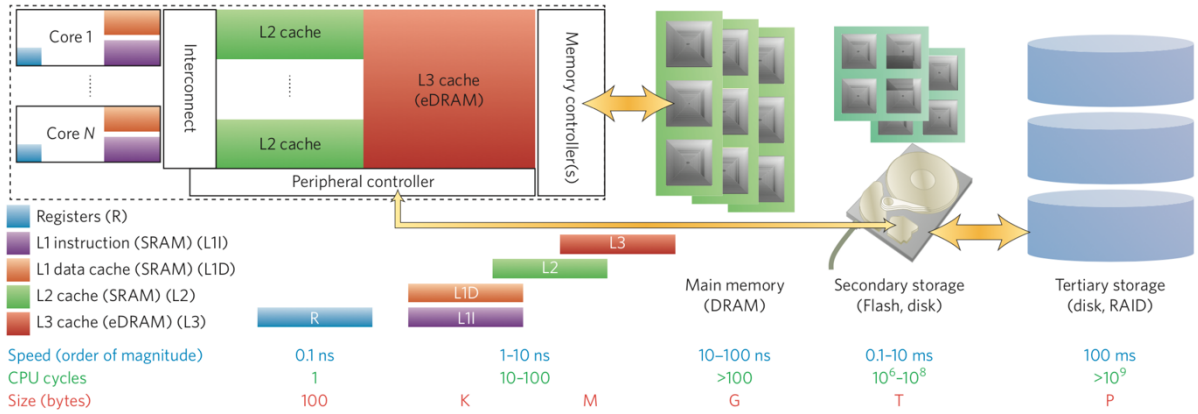

Figure 1-3: *The memory hierarchy and various memory types in a computer.Adapted from [18].*

With this vision in mind, in 2008, Parkin et al. [19] proposed racetrack memory where magnetic domains are used as data bits in columns of magnetic materials perpendicular to a silicon wafer as shown in Fig. 1-4. Information is stored as bits of "0" and "1" by two distinct states of magnetization "up" and "down". The domain walls can be moved along the length of the wires by nano second current pulses and intersect with reading or writing elements without the need to mechanically move read/write heads like in HDDs. Therefore, Parkin proposed that racetrack memory could attain information storage density and manufacturing cost comparable to HDDs, while attaining speed, mechanical robustness and low power consumption like solid-state RAM. The average access time for racetrack memory projected by Parkin et al. is 10-50ns versus 5ms for a HDD. This access time can be improved by attaining higher domain wall velocities.

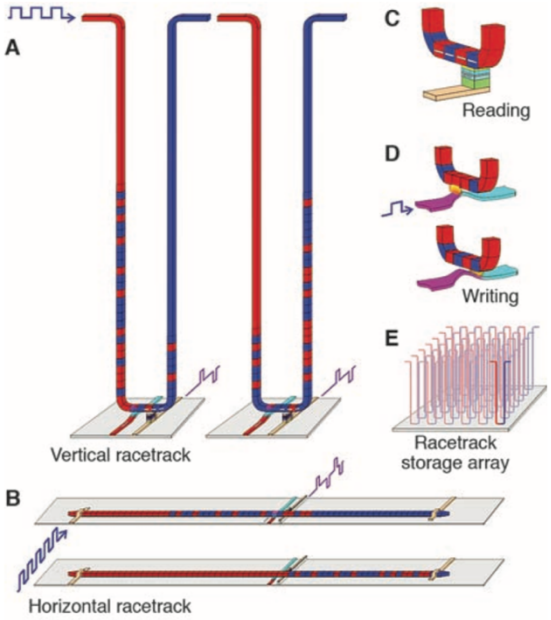

Figure 1-4: *Racetrack memory proposed by Parkin el. al. [19] A) vertical-configuration racetrack memory offering highest storage density. The two cartoons show the domain walls before and after passing a current pulse along the U-shaped nanowire. (B) A horizontal configuration racetrack memory. (C) Reading and (D) writing operation. E) racetrack storage array built on a chip to enable high-density storage.*

A year later in 2009**,** Fukami *et al*. experimentally demonstrated a new magnetic random access memory based on current induced domain wall motion [20]**.** The device consisted of a three terminal Magnetic Tunnel Junction (MTJ) and two transistors (T) as shown in Figure 4b. The reading is performed by the MTJ, that electrically reads the spin orientation of the magnetic domain under the tunnel barrier. The device consists of three regions: two fixed regions whose magnetization are oppositely aligned by pinning layers and a free layer in which the domain wall moves during writing. Based on the position of the domain wall the MTJ resistance can be high (low) thus representing '0' ('1'). The authors report a potential DW velocity of ~50m/s and 0.1mA , 2 ns writing with adequate thermal stability.

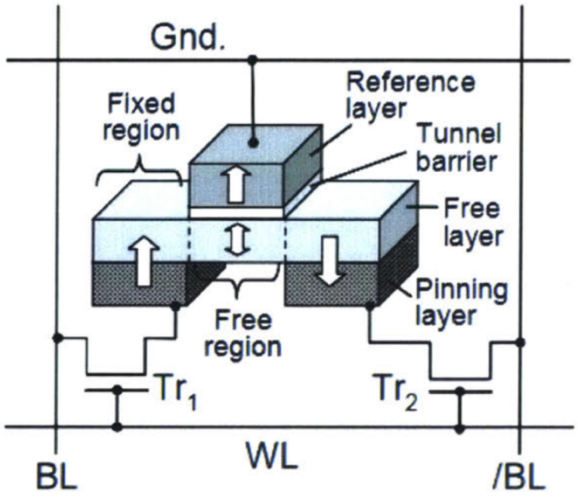

Figure 1- 5: *Cell structure proposed for solid state memory consisting of two transistors and one magnetic tunnel junction.* [20]

Most of the modern memory consist of magnetic thin films with perpendicular magnetic anisotropy grown on a variety of substrates. I will discuss the growth and characterization of BiYIG and BiYIG-TmIG thin films that allow record high domain wall velocities for fast and energy efficient spintronic memory.

Iron garnet are unique because of their strong magneto-optical response and transparency at communication wavelength that makes them important for use in non-reciprocal photonic devices. Moreover, by engineering the strain of Bi substituted iron garnet films on substituted gadolinium gallium substrates they can have perpendicular magnetic anisotropy and low damping making them invaluable for spintronics as well.

This thesis is divided into two sections:

1) Iron garnets for integrated photonics
2) Iron garnets for spintronic memory

1.3 Outline of Thesis

In Chapter 1, the motivation for this research and the outline for the thesis are presented.

Chapter 2 covers the necessary background on iron garnets, magneto-optics and spintronics to familiarize the reader in these topics.

Chapter 3 lists and explains the experimental methods used to grow and characterize the polycrystalline BiYIG, TbIG, BiTbIG, CeTbIG films and single crystal BiYIG and BiYIG-TmIG heterostructure thin films. It also describes the fabrication of hall crosses and domain wall tracks of the single crystal BiYIG films for electrical measurements.

Chapter 4 covers the research on the magneto-optical properties of polycrystalline bottom-up and top-down crystallized BiYIG/Si with high figure of merit.

Chapter 5 presents the research on seedlayer-free polycrystalline TbIG, BiTbIG and CeTbIG for nonreciprocal photonics

Chapter 6 covers the growth and magnetic property characterization of single crystal ultra-low damping BiYIG thin films that allow record domain wall velocities of up to 4500 m/s.

Chapter 7 discusses the work on heterostructure BiYIG-TmIG thin films. The introduction of DMI in BiYIG by introducing small amounts of Tm is discussed in this chapter.

Chapter 8 summarizes all the work concluded in this thesis and provides a conclusion and outlook for future work in this field.

References

[1] Kirchain, R. and Kimerling, L., 2007. A roadmap for nanophotonics. Nature Photonics, 1(6), pp.303-305.

[2] Grzela, T., 2015. Comparative STM-based study of thermal evolution of Co and Ni germanide nanostructures on Ge (001).

[3] Sun, C., Wade, M.T., Lee, Y., Orcutt, J.S., Alloatti, L., Georgas, M.S., Waterman, A.S., Shainline, J.M., Avizienis, R.R., Lin, S. and Moss, B.R., 2015. Single-chip microprocessor that communicates directly using light. Nature, 528(7583), pp.534-538.

[4] Atabaki, A.H., Moazeni, S., Pavanello, F., Gevorgyan, H., Notaros, J., Alloatti, L., Wade, M.T., Sun, C., Kruger, S.A., Meng, H. and Al Qubaisi, K., 2018. Integrating photonics with silicon nanoelectronics for the next generation of systems on a chip. Nature, 556(7701), pp.349-354.

[5] Sun, J., Timurdogan, E., Yaacobi, A., Hosseini, E.S. and Watts, M.R., 2013. Large-scale nanophotonic phased array. Nature, 493(7431), pp.195-199.

[6] Wang, J., Paesani, S., Ding, Y., Santagati, R., Skrzypczyk, P., Salavrakos, A., Tura, J., Augusiak, R., Mančinska, L., Bacco, D. and Bonneau, D., 2018. Multidimensional quantum entanglement with large-scale integrated optics. Science, 360(6386), pp.285-291.

[7] Hu, J., Zhang, Y., Du, Q., Wang, C., Fakhrul, T., Zhang, Y., Liu, S., Deng, L., Goncalves, C., Blanco, C. and Richardson, K., 2020, February. Filling in the missing link: monolithic optical isolators on silicon with high performance, broadband operation, and polarization diversity. In Photonic and Phononic Properties of Engineered Nanostructures X (Vol. 11289, p. 112891L). International Society for Optics and Photonics.

[8] Du, Q., Fakhrul, T., Zhang, Y., Hu, J. and Ross, C.A., 2018. Monolithic magneto-optical oxide thin films for on-chip optical isolation. MRS Bulletin, 43(6), pp.413-418.

[9] Fakhrul, T., Tazlaru, S., Beran, L., Zhang, Y., Veis, M. and Ross, C.A., 2019. Magneto-optical Bi: YIG films with high figure of merit for nonreciprocal photonics. Advanced Optical Materials, 7(13), p.1900056.

[10] Zhang, Y., Du, Q., Wang, C., Fakhrul, T., Liu, S., Deng, L., Huang, D., Pintus, P., Bowers, J., Ross, C.A. and Hu, J., 2019. Monolithic integration of broadband optical isolators for polarization-diverse silicon photonics. Optica, 6(4), pp.473-478.

[11] Fakhrul, T., Tazlaru, S., Khurana, B., Beran, L., Bauer, J., Vančík, M., Marchese, A., Tsotsos, E., Kučera, M., Zhang, Y. and Veis, M., 2021. High Figure of Merit Magneto-Optical Ce-and Bi-Substituted Terbium Iron Garnet Films Integrated on Si. Advanced Optical Materials, p.2100512.

[12] Du, Q., Wang, C., Zhang, Y., Zhang, Y., Fakhrul, T., Zhang, W., Gonçalves, C., Blanco, C., Richardson, K., Deng, L. and Ross, C.A., 2018. Monolithic on-chip magneto-optical isolator with 3 dB insertion loss and 40 dB isolation ratio. ACS photonics, 5(12), pp.5010-5016.

[13] Huang, D., Pintus, P. and Bowers, J.E., 2018. Towards heterogeneous integration of optical isolators and circulators with lasers on silicon. Optical Materials Express, 8(9), pp.2471-2483.

[14] https://medium.com/adamedelwiess/high-performance-computer-architecture-3-introduction-to-the-computer-architecture-moores-law-625a70bb0caf#:~:text=One%20of%20the%20consequences%20of,also%20doubling%20every%20two%20years.

[15] Xie, Y., 2013, March. Future memory and interconnect technologies. In 2013 Design, Automation & Test in Europe Conference & Exhibition (DATE) (pp. 964-969). IEEE.

[16] Hennessy, J.L. and Patterson, D.A., 2011. Computer architecture: a quantitative approach. Elsevier.

[17] Zhu, J.G.J. and Park, C., 2006. Magnetic tunnel junctions. Materials today, 9(11), pp.36-45.

[18] Wong, H.S.P. and Salahuddin, S., 2015. Memory leads the way to better computing. Nature nanotechnology, 10(3), pp.191-194.

[19] Parkin, S.S., Hayashi, M. and Thomas, L., 2008. Magnetic domain-wall racetrack memory. Science, 320(5873), pp.190-194.

[20] Fukami, S., Suzuki, T., Nagahara, K., Ohshima, N., Ozaki, Y., Saito, S., Nebashi, R., Sakimura, N., Honjo, H., Mori, K. and Igarashi, C., 2009, June. Low-current perpendicular domain wall motion cell for scalable high-speed MRAM. In 2009 Symposium on VLSI Technology (pp. 230-231). IEEE.

2. Background

This chapter will cover all the necessary background on iron garnets. As iron garnets thin films are being studied in this thesis for both magneto-optical isolators and spintronic memory, the theory on magneto-optics and domain wall motion for spintronic memory will also be discussed.

2.1 Iron Garnets

Magnetic garnets are cubic crystals having large unit cells containing 8 formula units and a total of 160 ions/unit cell as shown in Fig. 2-1. The chemical formula of the garnet is $\{c^{3+}\}_3[a^{3+}]_2(d^{3+})_3O_{12}$ which means that there are three different lattice sites for the cations with respect to the surrounding oxygen anions (Fig. 2-1). The cubic unit cell of iron garnet structure comprises of;

- 24{c}dodecahedral sites with 8 oxygen neighbors
- 16[a] octahedral sites with 6 oxygen neighbors occupied by Fe^{3+}
- 24(d) tetrahedral sites with 4 oxygen neighbors also occupied by Fe^{3+}

In this thesis work, the dodecahedral sites {c} are occupied by Y^{3+}, Bi^{3+} or by rare-earth cations (Fig. 2-1). The octahedral [*a*] and tetrahedral (*d*) sites are occupied by Fe^{3+} and are coupled antiferromagnetically through O^{2-} ions due to superexchange[21,22] . As there are a higher number of tetrahedral sites than octahedral sites (ratio 3:2) this yields a ferrimagnetic crystal where the net magnetization is due to the dominant tetrahedral sublattice. The temperature-dependent saturation magnetization M_S of the crystal is given by the vectorial sum of the sublattice magnetizations. Assuming that the dodecahedral lattice is occupied by non-magnetic ions like Y^{3+} or Bi^{3+} one obtains

$$M_S\,(T) = M_d\,(T) - M_a\,(T)$$

where Md and Ma denote the saturation magnetizations of the tetrahedral and octahedral sublattices, respectively. When the {c} are occupied by magnetic ions like rare earths they couple antiferromagnetically to the tetrahedral site ions, and a compensation temperature can occur in the magnetization versus temperature curve as shown in Fig. 2-2(a, b). This happens when the magnetic moment of the c sublattice equals and then surpasses the net moment of the opposing d and a sublattice. The net magnetization in this case would be;

$$M_S\,(T) = |\, M_d\,(T) - M_a\,(T) - M_c\,(T)\,|$$

where, M_c denotes the saturation magnetization of the dodecahedral sublattice.

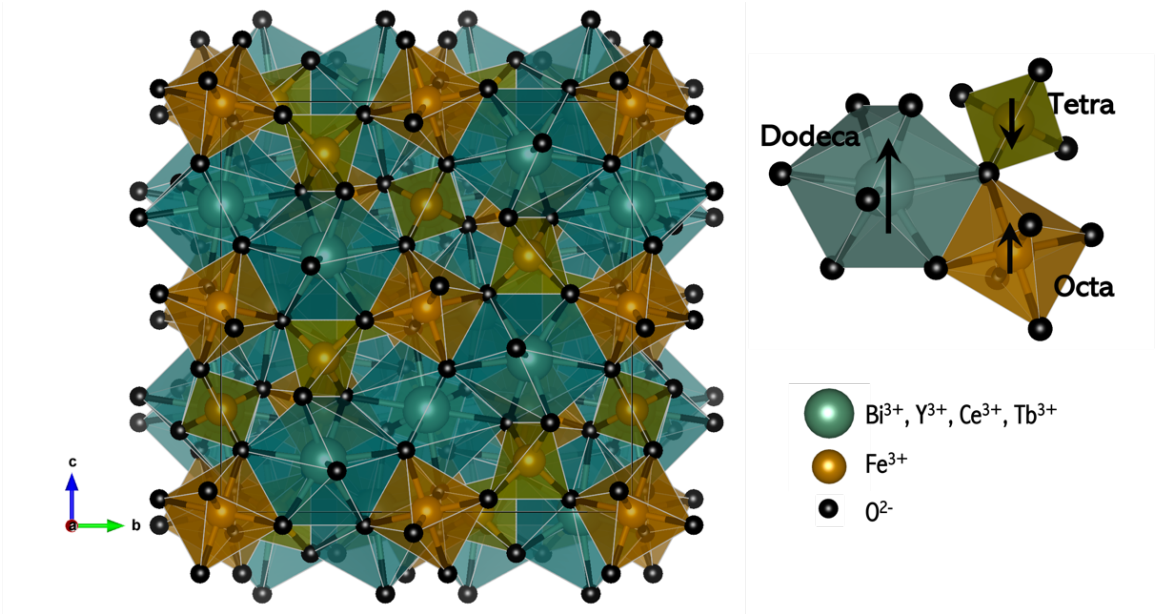

Figure 2-1: *Cubic unit cell of iron garnet showing octahedral, tetrahedral, and dodecahedral cation sites. The cation sites are surrounded by O^{2-} (indicated by black spheres) at the vertices of the polyhedrons. Magnetization directions of the sublattices are shown using black arrows.*

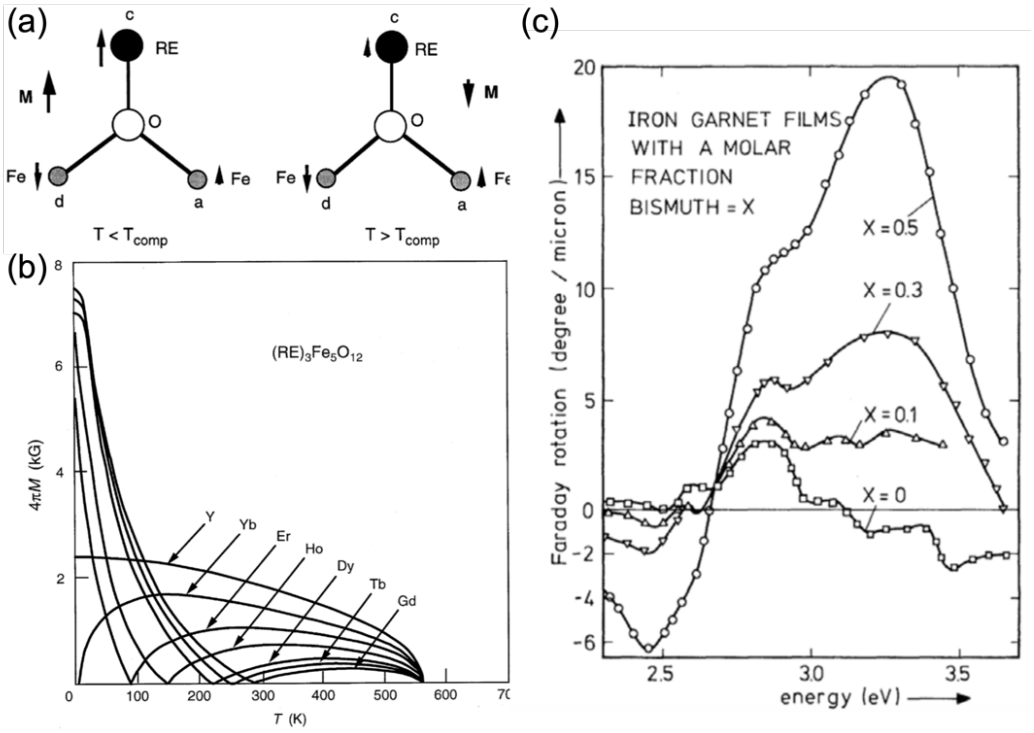

Figure 2-2: *a) The anatomy of the sublattice magnetic moment cancellation in rare-earth garnets that causes the compensation temperature.* [23] *b) Temperature dependent magnetization of the rare-earth series occupying c sites in the iron garnet system.*[23] *c) The Faraday rotation of Bismuth substituted yttrium iron garnet.* [24]

Iron garnets commonly used in optical isolator and circulators are yttrium iron garnet (YIG, $Y_3Fe_5O_{12}$) with substituents such as Ce or Bi to enhance its MO performance [4-20] as shown in Fig. 1-7(c). What makes garnets even more promising for optical isolation is their high transparency around communication wavelength with polycrystalline BiYIG reported to have Faraday rotations as high as 2000deg/cm with absorption as low as 1.26 dB cm^{-1}.[7]

Rare earth iron garnets with perpendicular magnetic anisotropy have also lately attracted a great deal of attention for spintronic devices for their low power and high-frequency magnetization dynamics [21-24]. Conventional PMA metallic ferromagnets pose a problem because of their stray fields limit bit size and their considerably high damping losses which limit their read/write speeds and energy efficiency [24,25]. Soumah et at. [26] showed that Bismuth substituted yttrium iron garnet (BiYIG) combines the advantages of PMA in conventional rare earth iron garnets while also demonstrating low damping shown in YIG. More recently, we reported that low damping BiYIG can allow record current-driven domain wall velocities of 4.5 km/s. [27]

2.2 Iron garnets for integrated photonics

2.2.1 Magneto-optic effects

Magneto-optic (MO) effect is defined as the change in the state of polarization of light upon interaction with a magnetic material. There are three kinds of magneto-optic effects:

1) Faraday effect
2) Voight effect
3) Kerr effect

Faraday effect was first discovered in 1845 by Michael Faraday who found that the polarization of light was rotated upon transmission through a piece of glass where a magnetic field was applied in the direction of propagation. In Faraday effect the incident wave vector direction **k** is parallel to the magnetization direction of the magneto-optical material. In Voigt effect, the incident wave vector direction **k** is perpendicular to the magnetization as shown in Fig. 2-3 (a,b).

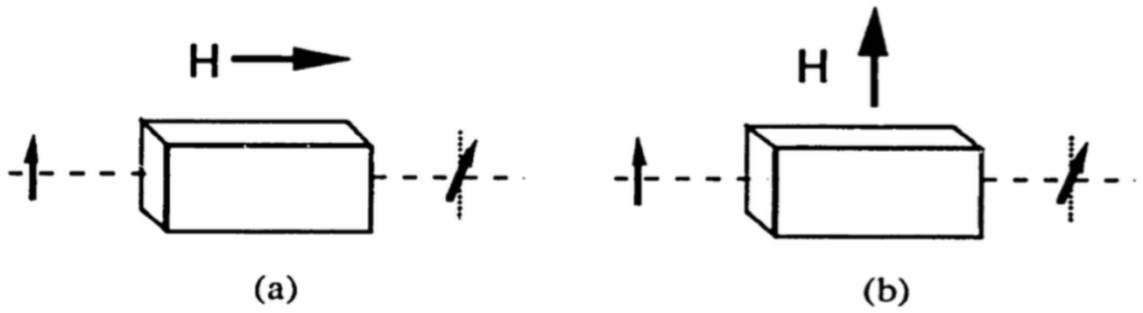

Figure 2-3: *a) Faraday effect b) Voight effect.* [28]

In contrast to Faraday and Voight effect, in Kerr effect there is a rotation in the plane of polarization of light being reflected from a magneto-optical material. There are three different configurations possible for the magneto-optical Kerr effect: polar, longitudinal and transverse as shown in Fig. 2-4.

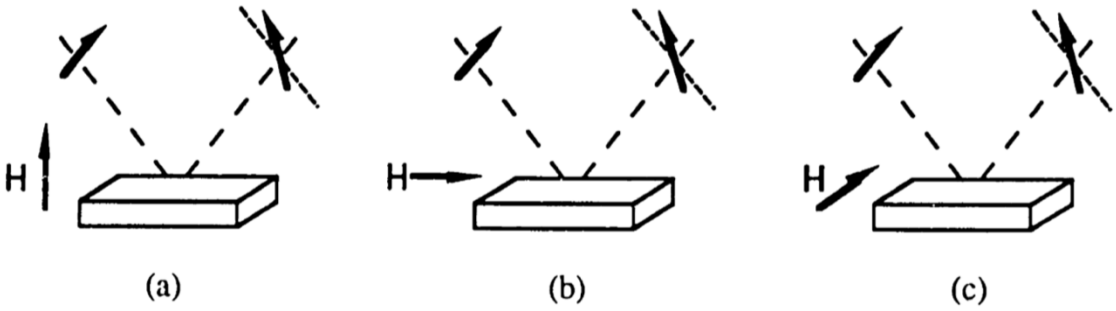

Figure 2-4: *Magneto-optical Kerr effects. (a) Polar, (b) longitudinal and (c) transverse Kerr effect.* [28]

In Faraday effect when a magnetic field is applied to a magneto-optical material in the direction of propagation (in the z direction), the resulting dielectric tensor of the material takes the form [29] :

$$\varepsilon = \varepsilon_0 \begin{pmatrix} n^2 & j\varepsilon_{xy} & 0 \\ -j\varepsilon_{xy} & n^2 & 0 \\ 0 & 0 & n^2 \end{pmatrix}$$

where n is the index of refraction and ε_{xy} is the off-diagonal element in the permittivity tensor. The diagonal elements represent the optical properties of the material in the absence of magneto-optic effects. The presence of non-zero off-diagonal element ε_{xy} is the origin of the Faraday Effect. The eigenmodes for this antisymmetric dielectric tensor are left and right circularly polarized and the Faraday rotation is a consequence of the phase difference between these two eigenmodes. Under the assumption that ε_{xy} is much smaller than n^2 than by Taylor expansion of the propagation constants for the eigenmodes (β_l and β_r), the Faraday coefficient or rotation per unit length is given by [29] :

$$\theta_F = \frac{\beta_r - \beta_l}{2} = \frac{\omega}{c}\frac{\varepsilon_{xy}}{2n}$$

For weak magnetic fields the Faraday rotation can be defined as the rotation per unit length per unit magnetic field that is known as the Verdet coefficient. Then, rotation θ through a medium of length l becomes

$$\theta = \theta_F l = VBl$$

where V is the Verdet constant and B is the magnetic field.

2.2.2 Origin of magneto-optic effects

Conventionally, all MO effects are a consequence of electron energy level splitting when a magneto-optical medium is subjected to a magnetic field [1]. In magnetic oxides, these energy levels can be split due to spin orbit coupling. The light with different polarizations will cause different electron dipole transitions between electronic states that follow the selection rule. Linearly polarized light passing through a magneto-optical material can be considered as a superposition of left and right circularly polarized light (LCP, RCP). The orientation of the plane of polarization of the incoming light is a function of the relative phases of the two components. In Faraday effect, LCP and RCP components of light experience different refractive indexes which translates to the retardation of one component compared to the other resulting in a phase difference between the two polarized components. A difference in phase between the two components induces ellipticity and thus optical rotation of the output light as shown in Fig. 2-5.

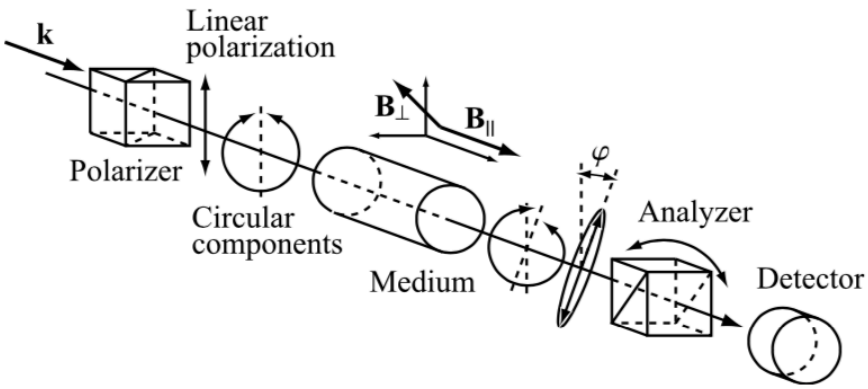

Figure 2-5: *Rotation of plane of polarization of linearly polarized light due to Faraday ($B_{||}$) and Voigt ($B\_ \perp$) effects.* [30]

2.2.3 Magneto-optical Isolator

A MO isolator is simply a diode for light, which allows light propagation in only the forward direction. Optical isolators as well as circulators are based on non-reciprocal phenomena, most commonly magnetooptical, that break the symmetry between forward and backward propagating light. The phenomenon used in commercial bulk isolators is Faraday rotation. This is a non-reciprocal rotation of the plane of polarization of light. It is non-reciprocal in the sense that the rotation is independent of the direction of light propagation. If light propagates through a Faraday rotating medium (bulk magneto-optical crystal), after a single pass its polarization is rotated by an angle θ, and after a round-trip it is rotated by 2θ. The simplest bulk isolator design involves two polarizers and a Faraday rotator. Fig. 2-6 shows the schematic of the conventional bulk isolator. In the forward direction, light passes through the first polarizer and then through the Faraday rotator, upon which it is rotated 45°. A second polarizer is aligned with this rotated polarization, allowing the light to pass through unattenuated. In the reverse direction, the light hits the 45° polarizer first. Then, after passing through the Faraday rotator, the light's polarization is rotated 45° and is orthogonal to the initial polarizer. The first polarizer, providing the isolation, then blocks the light. Commercial isolators consist of birefringent beam displacers and half-wave plates that allow polarization independent isolation as shown in Fig. 2-6 c. and can achieve isolations ranging from 30 to 40 dB with insertion loss less than 1dB. Standard Faraday isolators are convenient for a fixed wavelength operation and are usually narrowband (Fig. 2-6 c). However, broadband isolation can also be achieved by coupling the 45° Faraday nonreciprocal rotator with a 45° reciprocal quartz rotator. In the forward direction the two rotations (Faraday rotator and quartz rotator) happen in the same direction and add up to 90° rotation. The light is then transmitted through the output polarizer with its polarization axis rotated at 90° with respect to the input polarizer. In the opposite direction the net rotation is now equal to 0°, and thus the light is blocked by input polarizer. The wavelength dependence of the two rotator materials work together to produce a flat-top isolation profile as shown in Fig 2-6d.

Unfortunately, commercially available isolators are costly, have poor mechanical stability and are bulky with numerous components including MO crystals and polarizers. This makes them incompatible for on-chip integration. Monolithic integration of nonreciprocal devices like optical isolators can help resolve the problems associated with bulk isolators. In designing material for magneto-optical isolators, there are two main requirements. First of all the material

should possess a large Faraday rotation per unit length, i.e. it must rotate a linearly polarized beam of light through a large angle in a short distance and do so in a nonreciprocal fashion. The other requirement is that the material should be transparent to the wavelength in use so that loss due to the isolator is minimized. Therefore, to evaluate the usefulness of a MO material, the figure of merit (FoM) is defined as:

$$FoM = \theta/\alpha$$

where, θ and α are the Faraday rotation and absorption coefficient per length of the material. For semiconductor integration of optical isolators, another criterion is the compatibility with semiconductor substrates and fabrication techniques to achieve high FoM magneto-optical materials. A simultaneous satisfaction of both high FoM and semiconductor compatibility is a prerequisite for material applications in high quality semiconductor integrated magneto-optical devices[5-13,32]. This thesis will discuss in detail high FoM materials that will allow on-chip integration of high-performance isolators.

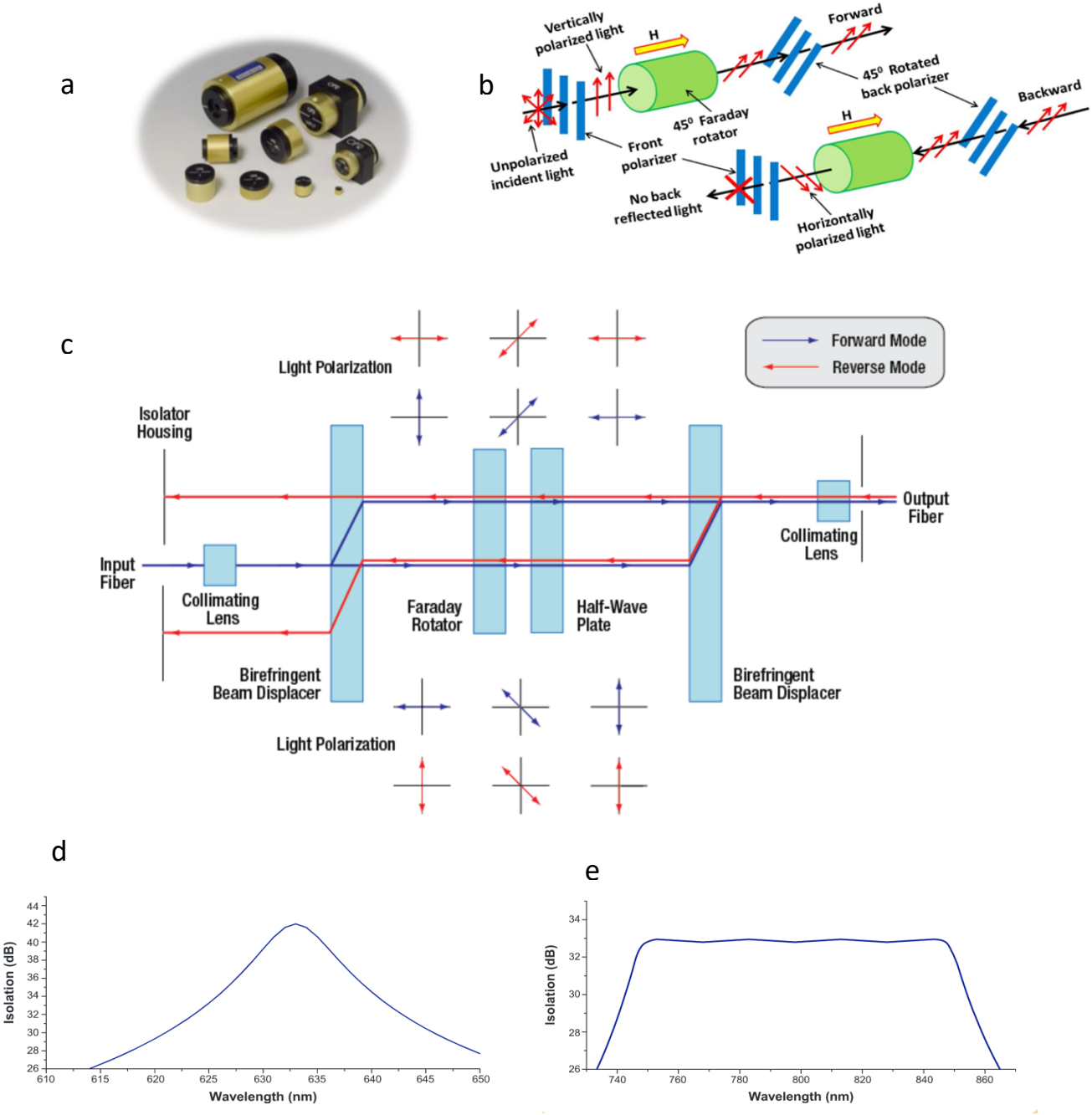

Figure 2-6: *a) Commercial bulk optical isolator b) Isolator working principle.[31] c) Polarization independent isolator. Isolation profile versus wavelength for d) fixed narrow band isolator e) fixed broadband isolator. Figures adapted from Thor Labs website.*

2.3 Iron garnets for spintronic memory

2.3.1 Magnetic domain walls

Magnetic domains are regions within a magnetic material that have uniform magnetization. A magnetic domain wall is a boundary between two adjacent domains of different orientation. In magnetic materials, domain walls (DWs) exist to reduce the magnetostatic energy arising from the large stray fields as can be seen in Fig. 2-7.

In thin films and patterned structures with perpendicular magnetic anisotropy, magnetostatic energy of the wall itself stabilizes two different types of walls: Bloch walls and Néel walls as shown in Fig. 2-8. In Bloch domain walls the magnetic moment rotates around an axis perpendicular to the domain wall and in Néel domain walls it rotates around an axis parallel to the domain wall as illustrated in Fig. 2-8. Bloch domain walls are preferred magneto statically in thicker films which have smaller DW width while Néel walls generally form in thinner films with wider domain wall widths.

The formation of domain walls cost a finite amount of energy as the moments inside the DW are not all aligned parallel with respect to each other therefore costing exchange energy. At the same time they deviate from the easy axis of the material at the expense of anisotropy energy. The energy required to from a Bloch domain wall is a function of the exchange stiffness A and the uniaxial anisotropy constant K and is given by:

$$\sigma_{DW} = \pi\sqrt{AK}$$

The domain walls have a finite width that is also a function of A and K and is given by:

$$\Delta = \sqrt{(A/K)}$$

From the above equation it is evident that the anisotropy competes with the exchange stiffness. The anisotropy prefers an infinitesimally small domain wall as this ensures more moments are

aligned along the easy axis while the exchange stiffness energetically prefers a wide domain wall that keeps more moments in the DW closer to parallel alignment.

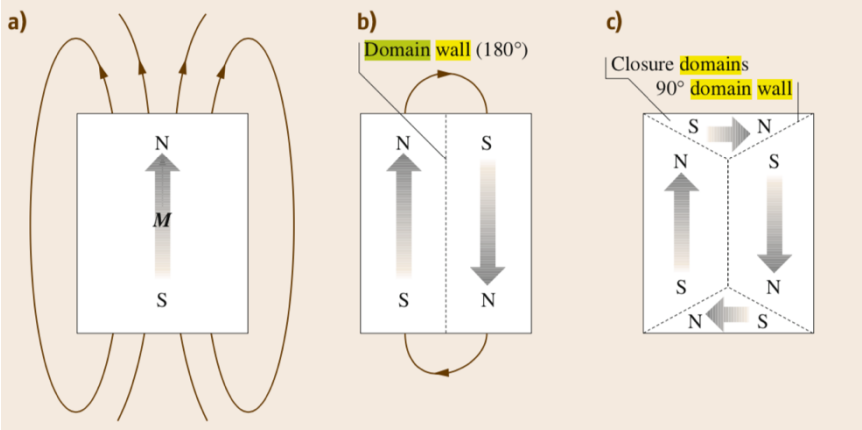

Figure 2-7: *Schematic illustration of the break-up of magnetisation into domains a) Uniformly magnetized single domain material with high magnetostatic energy (stray fields) b) two-domain material with lower magnetostatic energy c) multi-domain material with zero stray fields.* [33]

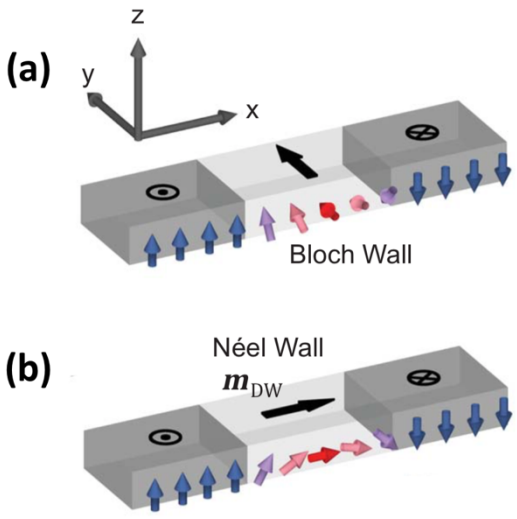

Figure 2-8*: Domain wall configurations illustrated for a perpendicularly magnetized thin film (a) Bloch domain wall (b) Néel domain wall.* [27]

2.3.2 Moving domain walls

The traditional way to move domain walls is by applying an external field and expand one domain while shrinking another. Current is used to generate Oersted fields generated from wires. This kind of manipulation of DWs is very power inefficient. Uniform magnetic fields cannot be used to translate a series of bits/DWs along a racetrack as adjacent DWs move in opposite directions annihilate one another. Moreover, as devices continue to scale down and the device density per unit area increases it becomes difficult to manipulate DWs in one device without impacting DWs in a neighboring device.

Fortunately, there are more power efficient alternatives to drive DWs. Electric currents can drive domain walls in metallic ferromagnets by spin-transfer torque effects. By patterning electrical contacts on devices one can manipulate DWs in a device while leaving neighboring devices intact. Moreover, with current-driven motion, multiple DWs can be moved uniformly without annihilating stored information. The driving force on DWs scales with current density making current-driven motion appealing for scaling down. Spin polarized currents generated from a magnetic material or a non-magnetic heavy metal can be used to apply a torque and change the state of magnetization of an adjacent magnetic layer.

The two kinds of spin torque (angular momentum transfer) are:

Spin-transfer torque: Torque originates from spin polarization originating from a magnetic material.

Spin-orbit torque: Torque originates from spin polarization coming from spin Hall effect in a non-magnetic heavy metal material

For the scope of this thesis, we will only be discussing spin-orbit torque induced current-driven motion.

2.3.2.1 Spin-orbit Torque (SOT)

The possibility to use a spin-polarized current to apply torques on magnetic moments by direct transfer of spin angular momentum dates back to the seminal work of Slonczewski [34] and Berger [35]. This enables manipulation of magnetic devices with currents that are orders of magnitude lower than that required by magnetic field driven motion [34-38].

One of the acknowledged mechanisms of spin orbit torque was proposed by Liu et al. [39] Spin currents can be generated in non-magnetic heavy material (Pt, Ta, W) by the spin Hall effect (SHE) in which spin orbit coupling in heavy metals generates a pure spin current transverse to the applied charge current as shown in Fig. 2-9(a). This spin current arises from spin-dependent scattering of conduction electrons in the heavy metal, where "up" spins scatter in a particular direction and "down" spins scatter in the opposite direction. This accumulation of spins at the interface of the heavy metal and adjacent ferromagnet can be used to exert a magnetic torque on the magnetic moment of the ferromagnet/ferromagnet known as the damping-like torque. The damping-like torque from the spin hall effect acts like an out-of-plane magnetic field on the DW (Fig) that can be written as

$$H_{SHE} = \chi_O \, j \cos \Phi$$

Here χ_O is proportional to the spin hall angle (ratio of the spin current to the charge current) of the heavy metal, Φ is the azimuthal DW angle between the DW moment and the current

direction as shown in Fig 2-9c. The spin hall symmetry is such that it only acts on domain walls that are completely Néel in configuration or have some Néel component [41]. Spin orbit torque cannot drive a DW with Bloch configuration as H_{SHE} becomes zero for fully Bloch DWs where $\Phi = \pm\frac{\pi}{2}$ as shown in Fig 2-8a. Regardless, spin Hall induced DW motion can be achieved in Bloch walls by applying an in-plane bias field and forcing Néel configuration (Fig 2-9c) [42]. Emori et al [43] discovered Dzylaloshinskii-Moriya interaction (DMI) present in asymmetrical films can stabilize homochiral Néel DW allowing up-down and down-up domain walls to move in the same direction with very high speeds.

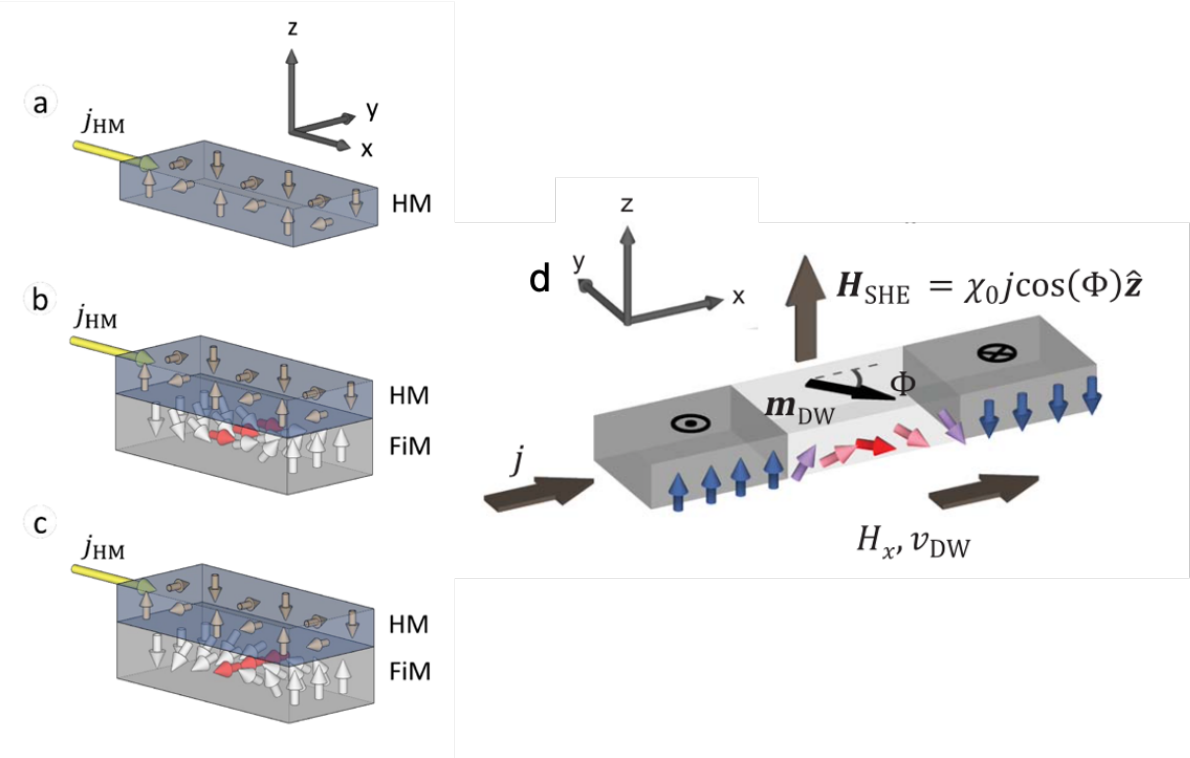

Figure. 2-9: *a) Spin Hall effect in heavy metal (HM) with arrows depicting accumulated spin orientation in each interface. Charge current j_{HM} is converted into a transverse spin current. Spin Hall effect acting on a Domain Wall. HM film interfaced with a ferrimagnet (FiM) domain wall of b) Néel and c) Bloch orientation. [40]* ***d)*** *Equilibrium domain wall orientation Φ when traveling at velocity v_{DW} under applied $\boldsymbol{H}_x\hat{\boldsymbol{x}}$ and driven by $\boldsymbol{H}_{SHE} = \chi_0 j\cos\Phi\,\hat{\boldsymbol{z}}$. Domain wall moment $\boldsymbol{m}_{DW}$ under an applied longitudinal in-plane field $\boldsymbol{H}_x\hat{\boldsymbol{x}}$ which forces Neel configuration. [27]*

2.3.3 Dzyaloshinskii-Moriya interaction (DMI)

In order to reduce exchange energy magnetic spins align parallel to each other in ferromagnets. This exchange energy can be written in terms of the Hamiltonian, which is often referred to as the Heisenberg exchange interaction Hamiltonian;

$$\widehat{H} = -\sum_{ij} J_{ij} S_i \times S_j$$

where J_{ij} is the exchange energy integral between two adjacent spins S_i and S_j. A positive J_{ij} indicates parallel spin alignment while a negative J_{ij} favors an anti-parallel spin configuration.

However, in some materials with broken inversion symmetry in their lattice or at interfaces in engineered materials, an additional interaction known as the Dzyaloshinskii-Moriya interaction (DMI) can be dominant. DMI is induced by two main ingredients namely a lack of inversion symmetry in the material and a strong spin-orbit coupling and its corresponding Hamiltonian is given by

$$\widehat{H_{DMI}} = -\sum_{ij} D_{ij} S_i \times S_j$$

where D_{ij} is the Dzyaloshinskii-Moriya tensor and S_i , S_j are adjacent tensors. DMI favors a perpendicular spin arrangement in order to minimize its cross product in contrast to Heisenberg exchange interaction that aligns neighboring spins in a parallel/anti-parallel configuration. Hence uniaxial ferromagnetic or antiferromagnetic structures fail to exist in DMIs, and instead are replaced by a directional non-collinear magnetic order of one specific chirality, either right-handed or left-handed depending on the sign of D_{ij}. When both the Heisenberg exchange interaction and the DMI are significant and compete in some materials, asymmetric magnetic twists and spirals can form like skyrmions and chiral domain walls as shown in Fig. 2-10 (a-d).

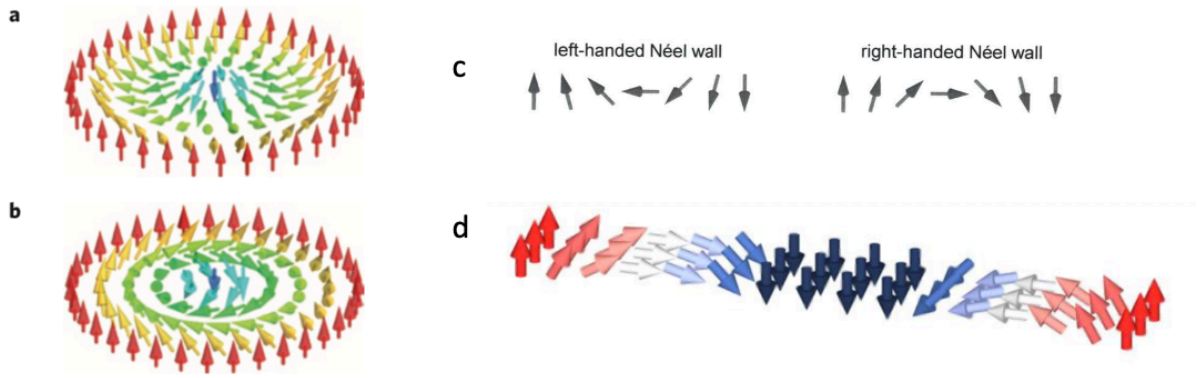

Figure 2-10: *a) Bloch and c) Néel skyrmions [44]. c) left and right-handed domain walls [45]. d) A pair of right-handed homochiral Néel domain walls. [46]*

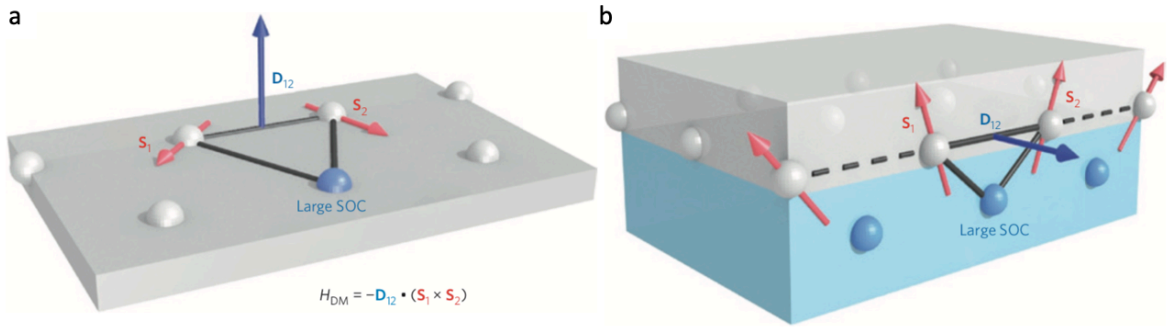

Figure 2-11: *Sketch of a) bulk and b) interfacial DMI manifesting in non-centrosymmetric crystals and the interface between heavy metal and ferromagnet systems, respectively. [44]*

DMI can arise in both non-centrosymmetric bulk materials (eg. MnW [47], MnSi [48], FeGe [49]) as well due to the broken inversion symmetry at interfaces between a ferromagnet and a heavy metal (Pt,Ta,W) with large spin orbit coupling as shown in Fig. 2-11 (a,b). In centrosymmertic materials D_{ij} tensor becomes zero so there is no DMI. Emori et al [43] and Ryu et al [50] separately discovered homochiral Néel domain walls at room temperature manifesting from interfacial DMI of Pt/Co(Fe)/oxide films. For this thesis we will focus on BiYIG thin films that form Bloch walls allowing ultrafast domain wall motion by application of in-plane fields. We will also discuss how to introduce DMI in BiYIG by addition of rare-earths like Tm.

References

[1] Zvezdin, A. K., & Kotov, V. A. (1997). *Modern magnetooptics and magnetooptical materials*. CRC Press.

[2] Dötsch, H., Bahlmann, N., Zhuromskyy, O., Hammer, M., Wilkens, L., Gerhardt, R., Hertel, P. and Popkov, A.F., 2005. Applications of magneto-optical waveguides in integrated optics. *JOSA B*, *22*(1), pp.240-253.

[3] Dionne, G.F., 2009. Magnetic oxides (Vol. 14, p. 15). New York: Springer.\

[4] Wittekoek, S., Popma, T.J., Robertson, J.M. and Bongers, P.F., 1975. Magneto-optic spectra and the dielectric tensor elements of bismuth-substituted iron garnets at photon energies between 2.2-5.2 eV. Physical review B, 12(7), p.2777.

[5] Hu, J., Zhang, Y., Du, Q., Wang, C., Fakhrul, T., Zhang, Y., Liu, S., Deng, L., Goncalves, C., Blanco, C. and Richardson, K., 2020, February. Filling in the missing link: monolithic optical isolators on silicon with high performance, broadband operation, and polarization diversity. In *Photonic and Phononic Properties of Engineered Nanostructures X* (Vol. 11289, p. 112891L). International Society for Optics and Photonics.

[6] Du, Q., Fakhrul, T., Zhang, Y., Hu, J. and Ross, C.A., 2018. Monolithic magneto-optical oxide thin films for on-chip optical isolation. *MRS Bulletin*, *43*(6), pp.413-418.

[7] Fakhrul, T., Tazlaru, S., Beran, L., Zhang, Y., Veis, M. and Ross, C.A., 2019. Magneto-optical Bi: YIG films with high figure of merit for nonreciprocal photonics. *Advanced Optical Materials*, *7*(13), p.1900056.

[8] Zhang, Y., Du, Q., Wang, C., Fakhrul, T., Liu, S., Deng, L., Huang, D., Pintus, P., Bowers, J., Ross, C.A. and Hu, J., 2019. Monolithic integration of broadband optical isolators for polarization-diverse silicon photonics. *Optica*, *6*(4), pp.473-478.

[9] Fakhrul, T., Tazlaru, S., Khurana, B., Beran, L., Bauer, J., Vančík, M., Marchese, A., Tsotsos, E., Kučera, M., Zhang, Y. and Veis, M., 2021. High Figure of Merit Magneto-Optical Ce-and Bi-Substituted Terbium Iron Garnet Films Integrated on Si. *Advanced Optical Materials*, p.2100512.

[10] Du, Q., Wang, C., Zhang, Y., Zhang, Y., Fakhrul, T., Zhang, W., Gonçalves, C., Blanco, C., Richardson, K., Deng, L. and Ross, C.A., 2018. Monolithic on-chip magneto-optical isolator with 3 dB insertion loss and 40 dB isolation ratio. *ACS photonics*, *5*(12), pp.5010-5016.

[11] Huang, D., Pintus, P. and Bowers, J.E., 2018. Towards heterogeneous integration of optical isolators and circulators with lasers on silicon. *Optical Materials Express*, *8*(9), pp.2471-2483.

[12] Bi, L., Hu, J., Jiang, P., Kim, D.H., Dionne, G.F., Kimerling, L.C. and Ross, C.A., 2011. On-chip optical isolation in monolithically integrated non-reciprocal optical resonators. *Nature Photonics*, *5*(12), pp.758-762.

[13] Bi, L., Hu, J., Jiang, P., Kim, H.S., Kim, D.H., Onbasli, M.C., Dionne, G.F. and Ross, C.A., 2013. Magneto-optical thin films for on-chip monolithic integration of non-reciprocal photonic devices. *Materials*, *6*(11), pp.5094-5117.

[14] Yokoi, H., Mizumoto, T. and Shoji, Y., 2003. Optical nonreciprocal devices with a silicon guiding layer fabricated by wafer bonding. *Applied optics*, *42*(33), pp.6605-6612.

[15] Srinivasan, K. and Stadler, B.J., 2018. Magneto-optical materials and designs for integrated TE-and TM-mode planar waveguide isolators: a review. *Optical Materials Express*, *8*(11), pp.3307-3318.

[16] Sun, X.Y., Du, Q., Goto, T., Onbasli, M.C., Kim, D.H., Aimon, N.M., Hu, J. and Ross, C.A., 2015. Single-step deposition of cerium-substituted yttrium iron garnet for monolithic on-chip optical isolation. *Acs Photonics*, *2*(7), pp.856-863.

[17] Goto, T., Onbaşlı, M.C. and Ross, C.A., 2012. Magneto-optical properties of cerium substituted yttrium iron garnet films with reduced thermal budget for monolithic photonic integrated circuits. *Optics express*, *20*(27), pp.28507-28517.

[18] Onbasli, M.C., Beran, L., Zahradník, M., Kučera, M., Antoš, R., Mistrík, J., Dionne, G.F., Veis, M. and Ross, C.A., 2016. Optical and magneto-optical behavior of cerium yttrium iron garnet thin films at wavelengths of 200–1770 nm. *Scientific reports*, *6*(1), pp.1-10.

[19] Mizumoto, T., Shoji, Y. and Takei, R., 2012. Direct wafer bonding and its application to waveguide optical isolators. *Materials*, *5*(5), pp.985-1004.

[20] Stadler, B.J. and Mizumoto, T., 2013. Integrated magneto-optical materials and isolators: a review. *IEEE Photonics Journal*, *6*(1), pp.1-15.

[21] Ahmed, A.S., Lee, A.J., Bagués, N., McCullian, B.A., Thabt, A.M., Perrine, A., Wu, P.K., Rowland, J.R., Randeria, M., Hammel, P.C. and McComb, D.W., 2019. Spin-Hall topological Hall effect in highly tunable Pt/ferrimagnetic-insulator bilayers. *Nano letters*, *19*(8), pp.5683-5688.

[22] Quindeau, A., Avci, C.O., Liu, W., Sun, C., Mann, M., Tang, A.S., Onbasli, M.C., Bono, D., Voyles, P.M., Xu, Y. and Robinson, J., 2017. Tm3Fe5O12/Pt heterostructures with perpendicular magnetic anisotropy for spintronic applications. *Advanced Electronic Materials*, *3*(1), p.1600376.

[23] Avci, C.O., Rosenberg, E., Caretta, L., Büttner, F., Mann, M., Marcus, C., Bono, D., Ross, C.A. and Beach, G.S., 2019. Interface-driven chiral magnetism and current-driven domain walls in insulating magnetic garnets. *Nature nanotechnology*, *14*(6), pp.561-566.

[24] Yang, S.H., Ryu, K.S. and Parkin, S., 2015. Domain-wall velocities of up to 750 m s− 1 driven by exchange-coupling torque in synthetic antiferromagnets. *Nature nanotechnology*, *10*(3), pp.221-226.

[25] Caretta, L., Mann, M., Büttner, F., Ueda, K., Pfau, B., Günther, C.M., Hessing, P., Churikova, A., Klose, C., Schneider, M. and Engel, D., 2018. Fast current-driven domain walls and small skyrmions in a compensated ferrimagnet. *Nature nanotechnology*, *13*(12), pp.1154-1160.

[26] Soumah, L., Beaulieu, N., Qassym, L., Carrétéro, C., Jacquet, E., Lebourgeois, R., Youssef, J.B., Bortolotti, P., Cros, V. and Anane, A., 2018. Ultra-low damping insulating magnetic thin films get perpendicular. *Nature communications*, *9*(1), pp.1-6.

[27] Caretta, L., Oh, S.H., Fakhrul, T., Lee, D.K., Lee, B.H., Kim, S.K., Ross, C.A., Lee, K.J. and Beach, G.S., 2020. Relativistic kinematics of a magnetic soliton. *Science*, *370*(6523), pp.1438-1442.

[28] Allen, G.A., 1994. *The magneto-optic spectra of bismuth-substituted iron garnets* (Doctoral dissertation, Massachusetts institute of technology).

[29] Zaman, T.R., Guo, X. and Ram, R.J., 2008. Semiconductor waveguide isolators. *Journal of Lightwave Technology*, *26*(2), pp.291-301.

[30] Budker, D., Gawlik, W., Kimball, D.F., Rochester, S.M., Yashchuk, V.V. and Weis, A., 2002. Resonant nonlinear magneto-optical effects in atoms. *Reviews of modern physics*, *74*(4), p.1153.

[31] Ghosh, S., 2013. *Optical isolators in silicon based photonic integrated circuits* (Doctoral dissertation, Ghent University).

[32] Zhang, Y., Du, Q., Wang, C., Yan, W., Deng, L., Hu, J., Ross, C.A. and Bi, L., 2019. Dysprosium substituted Ce: YIG thin films with perpendicular magnetic anisotropy for silicon integrated optical isolator applications. *APL Materials*, *7*(8), p.081119.

[33] Kasap, S. and Capper, P. eds., 2017. *Springer handbook of electronic and photonic materials*. Springer.

[34] Slonczewski, J.C., 1996. Current-driven excitation of magnetic multilayers. *Journal of Magnetism and Magnetic Materials*, *159*(1-2), pp.L1-L7.

[35] Berger, L., 1996. Emission of spin waves by a magnetic multilayer traversed by a current. *Physical Review B*, *54*(13), p.9353.

[36] Katine, J.A., Albert, F.J., Buhrman, R.A., Myers, E.B. and Ralph, D.C., 2000. Current-driven magnetization reversal and spin-wave excitations in Co/Cu/Co pillars. *Physical review letters*, *84*(14), p.3149.

[37] Kiselev, S.I., Sankey, J.C., Krivorotov, I.N., Emley, N.C., Schoelkopf, R.J., Buhrman, R.A. and Ralph, D.C., 2003. Microwave oscillations of a nanomagnet driven by a spin-polarized current. *nature*, *425*(6956), pp.380-383.

[38] Gambardella, P. and Miron, I.M., 2011. Current-induced spin–orbit torques. *Philosophical Transactions of the Royal Society A: Mathematical, Physical and Engineering Sciences*, *369*(1948), pp.3175-3197.

[39] Liu, L., Pai, C.F., Li, Y., Tseng, H.W., Ralph, D.C. and Buhrman, R.A., 2012. Spin-torque switching with the giant spin Hall effect of tantalum. *Science*, *336*(6081), pp.555-558.

[40] Caretta, L., Rosenberg, E., Büttner, F., Fakhrul, T., Gargiani, P., Valvidares, M., Chen, Z., Reddy, P., Muller, D.A., Ross, C.A. and Beach, G.S., 2020. Interfacial Dzyaloshinskii-Moriya interaction arising from rare-earth orbital magnetism in insulating magnetic oxides. *Nature communications*, *11*(1), pp.1-9.

[41] Khvalkovskiy, A.V., Cros, V., Apalkov, D., Nikitin, V., Krounbi, M., Zvezdin, K.A., Anane, A., Grollier, J. and Fert, A., 2013. Matching domain-wall configuration and spin-orbit torques for efficient domain-wall motion. *Physical Review B*, *87*(2), p.020402.

[42] Haazen, P.P.J., Murè, E., Franken, J.H., Lavrijsen, R., Swagten, H.J.M. and Koopmans, B., 2013. Domain wall depinning governed by the spin Hall effect. *Nature materials*, *12*(4), pp.299-303.

[43] Emori, S., Bauer, U., Ahn, S.M., Martinez, E. and Beach, G.S., 2013. Current-driven dynamics of chiral ferromagnetic domain walls. *Nature materials*, *12*(7), pp.611-616.

[44] Fert, A., Cros, V. and Sampaio, J., 2013. Skyrmions on the track. *Nature nanotechnology*, *8*(3), pp.152-156.

[45] Emori, S., 2013. *Magnetic domain walls driven by interfacial phenomena* (Doctoral dissertation, Massachusetts Institute of Technology).

[46] Caretta, L.M., 2019. *Chiral spin textures and dynamics in multi-sublattice magnetic materials* (Doctoral dissertation, Massachusetts Institute of Technology).

[47] Bode, M., Heide, M., Von Bergmann, K., Ferriani, P., Heinze, S., Bihlmayer, G., Kubetzka, A., Pietzsch, O., Blügel, S. and Wiesendanger, R., 2007. Chiral magnetic order at surfaces driven by inversion asymmetry. *Nature*, *447*(7141), pp.190-193.

[48] Mühlbauer, S., Binz, B., Jonietz, F., Pfleiderer, C., Rosch, A., Neubauer, A., Georgii, R. and Böni, P., 2009. Skyrmion lattice in a chiral magnet. *Science*, *323*(5916), pp.915-919.

[49] Yu, X.Z., Kanazawa, N., Onose, Y., Kimoto, K., Zhang, W.Z., Ishiwata, S., Matsui, Y. and Tokura, Y., 2011. Near room-temperature formation of a skyrmion crystal in thin-films of the helimagnet FeGe. *Nature materials*, *10*(2), pp.106-109.

[50] Ryu, K.S., Thomas, L., Yang, S.H. and Parkin, S., 2013. Chiral spin torque at magnetic domain walls. *Nature nanotechnology*, *8*(7), pp.527-533.

3. Experimental Methods

This chapter covers the experimental methods used throughout the thesis. The garnet thin films were grown by pulsed laser deposition and the Pt overlayers and Au contacts were sputtered in Prof. Luqiao Liu and Prof. Geoffrey Beach's labs respectively. Thickness of the films were measured using X-ray reflectometry (XRR) or profilometry. The structural characterization of the film X-ray diffraction (XRD) was used, and the surface topology and roughness were studied by Atomic force microscopy (AFM). Room temperature and temperature dependent magnetic properties of the films were studied by vibrating sample magnetometry (VSM) and superconducting quantum interference device (SQUID). TEM images of the film cross section for both polycrystalline and epitaxial BiYIG films were also collected to investigate the microstructure. The TEM samples were prepared using focused ion beam (FIB) milling with a 5-20nm of Pt coating on the insulating samples. The TEM of the polycrystalline BiYIG films were performed at MIT MRL using JEOL 2010F field-emission TEM, whereas the epitaxial BiYIG films were sent to Cornell university for TEM analysis in Prof. David Muller's group. TEM experiments were performed on an aberration-corrected electron microscope (Thermo Fisher Scientific, Titan Themis) with a probe-forming aperture semi-angle of 21.4 mrad at 300 keV. Hall crosses for spin magnetoresistance (SMR) measurements were fabricated by maskless photolithography and lift-off methods.

Compositional analysis was done by wavelength dispersive spectroscopy (WDS) using a JEOL-JXA-8200 Superprobe. The cation ratios in the thin films were calculated using GMR electron probe thin film microanalysis program[1] which takes into account the substrate contributions to the WDS spectrum and the effect of the substrate-film interface. High resolution X-ray photoelectron spectroscopy was used to study the valence states of the Ce and Bi substituted TbIG films.

3.1 Thin Film growth

3.1.1 Pulsed Laser Deposition (PLD)

PLD is a physical vapor deposition method that allows non-equilibrium and versatile growth of complex stoichiometries. It combines characteristics of both evaporation and sputtering and has several advantages that are not present with other common thin film deposition techniques. It has been extensively used for the growth of oxides since the discovery that it could be used to grow high-quality superconducting $YBa_2Cu_3O_7$ [2] films. A schematic plot of the PLD system used in this thesis is shown in Fig. 3-1. Thin film deposition is achieved by focusing laser pulses on a target of desired stoichiometry and generating a plume containing the atomic species of the target material that deposits on the substrate. The key components of the PLD chamber as shown in Fig. 1 include the chamber, laser (a Coherent COMPexPro 205 KrF with λ = 248 nm excimer laser), optics, turbomolecular pump, mechanical pump, target and substrates. Typical pulse durations are in the nanosecond range and as most materials are absorptive in these wavelengths the laser energy is readily absorbed to generate plumes. The laser pulses are guided by and focused by high quality quartz optical components that allow energy densities in the range of 2-3J/cm^2 on the target. The target spot hit by the laser pulse heats up rapidly and vaporizes, and the vapor absorbs more energy from the laser pulse to break down into a dense plasma. This plasma absorbs any remaining energy from the laser pulse and expands to create a plume perpendicular from the target surface resulting in deposition on the substrates placed above directly above the target. A high base pressure in the range of 10^{-6} Torr ensures high film purity. The chamber is typically either under vacuum or oxygen atmosphere at high temperatures or room temperature. Substrates are rotated during deposition to ensure uniformity and low roughness for film surfaces and the targets are rotated and rastered during laser ablation and deposition in order to ensure uniform ablation of the targets.

Some of the advantages of PLD for thin film growth include:

1) Allows close-to-stoichiometric transfer from the target to the film and the formation non-equilibrium phases in complex material systems.
2) Ability to grow multilayered heterostructures. Separate targets can be used in the same deposition by rotating the carousel holding the targets to allow for growth of multilayered epitaxial and polycrystalline films.

3) Allows for Combinatorial PLD growth. PLD can grow composite or combinatorial composition gradients of complex oxides from multiple oxide targets by offsetting the target and substrate positions to deposit films that vary linearly in composition between two compounds.
4) PLD systems are modular allowing decoupling of the growth chamber and the laser. This allows the use of different lasers with different wavelengths, powers, pulse width which enables PLD growth of different classes of materials.

A limitation of PLD is the nonuniformity in the films composition or thickness due to the forward-directed plume nature. However, this non-uniformity is usually eliminated by rotation the substrate holder or raster scanning the laser across the target surface.

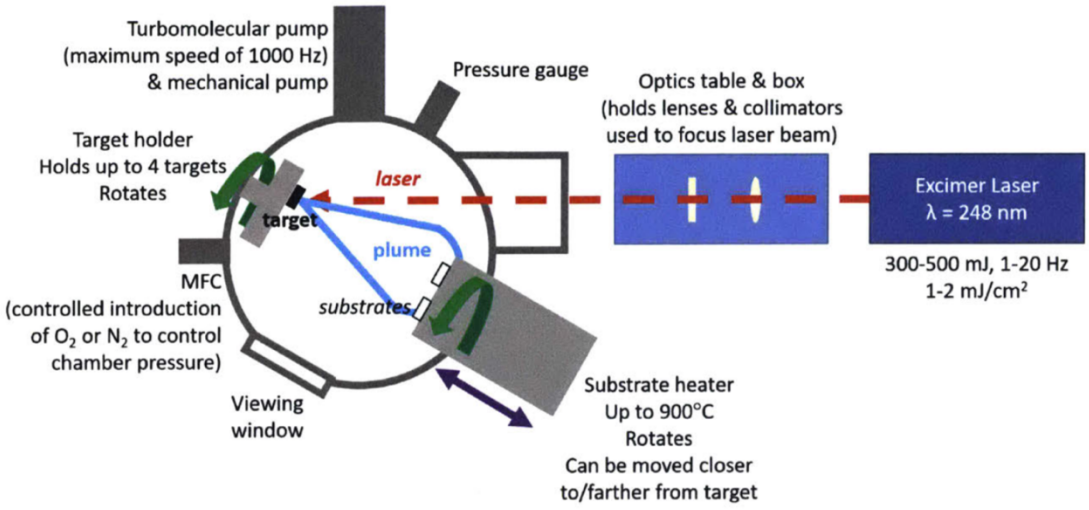

Figure 3-1: *Plot of the PLD setup used for film growth* [3]

3.1.2 Garnet target fabrication

Single-phase targets of TbIG ($Tb_3Fe_5O_{12}$), CeTbIG ($Ce_1Tb_2Fe_5O_{12}$, $Ce_2Tb_1Fe_5O_{12}$) and BiTbIG ($Bi_{0.3}Tb_{2.7}Fe_5O_{12}$) were made by using conventional mixed oxide sintering method. The furnaces in Prof. Harry Tuller labs were used for this purpose. The desired stoichiometry of targets were obtained by mixing the correct amounts of oxide powders (99.999% pure Tb_2O_3, CeO_2, Bi_2O_3, and Fe_2O_3) based on the reaction equation of the calcination and sintering processes. After mixing and grinding with a mortar and pestle, the powders were ball milled with alumina grinding media and ethanol for 24 hrs. The dried mixture is then calcinated for

12 hours in a tube furnace at 1400°C. The process of mixing, grinding and ball milling is repeated on the calcined powders after which the powder is cold isostatically pressed into 1 inch diameter cylindrical discs at 40,000 psi for 2 min. Finally, the cold pressed disc is sintered for 18 hours in a tube furnace at 1400°C.

3.2 Lithography and Lift-off for Spintronic Device Fabrication

After deposition, the single crystal BiYIG and BiYIG-TmIG heterostructures were patterned to make hall crosses and domain wall track devices. Maskless lithography was done using the Heidelberg DirectWrite-MLA-150-OptAF. The MLA-150 is a direct-write laser system that can expose UV sensitive photoresist on wafers, with the choice of a 375nm or 405 nm diode laser without the need of any mask fabrication allowing faster prototyping cycles. The flow chart of the device fabrication is shown in Fig. 3-2. After film growth and Pt deposition the sample is spin coated with photoresist AZ3312 at 4500rpm and pre-baked at 102°C for 60s. The pattern is then exposed using the MLA with the 375nm diode laser and a dose of 100mJ/cm^2. After exposing, the sample is post baked at 112°C for 60s and then developed in AZ300 for 75s. The patterned film is the ion milled with Ar plasma leaving behind only regions protected by the resist.

Lift-off is used for contact deposition where Au (150nm)/Ta (5nm) contacts are deposited after resist coating. To facilitate high yield metal lift-off, a bilayer photoresist stack of PMGI and AZ3312 is used as shown in Fig. 3-2. PMGI is spin coated on the sample at 4500rpm and the film is baked at 220°C for 300s followed by AZ3312 spin coating at 4500rpm and pre-baking at 102°C for 60s. The pattern is then exposed using MLA with the 375nm diode laser and a dose of 160mJ/cm^2. After resist development, contacts are deposited and the film is immersed in NMP overnight. Finally, the samples are splashed with IPA for metal lift-off. The PMGI resist ensures smooth lift-off of the Au/Ta without need for sonication.

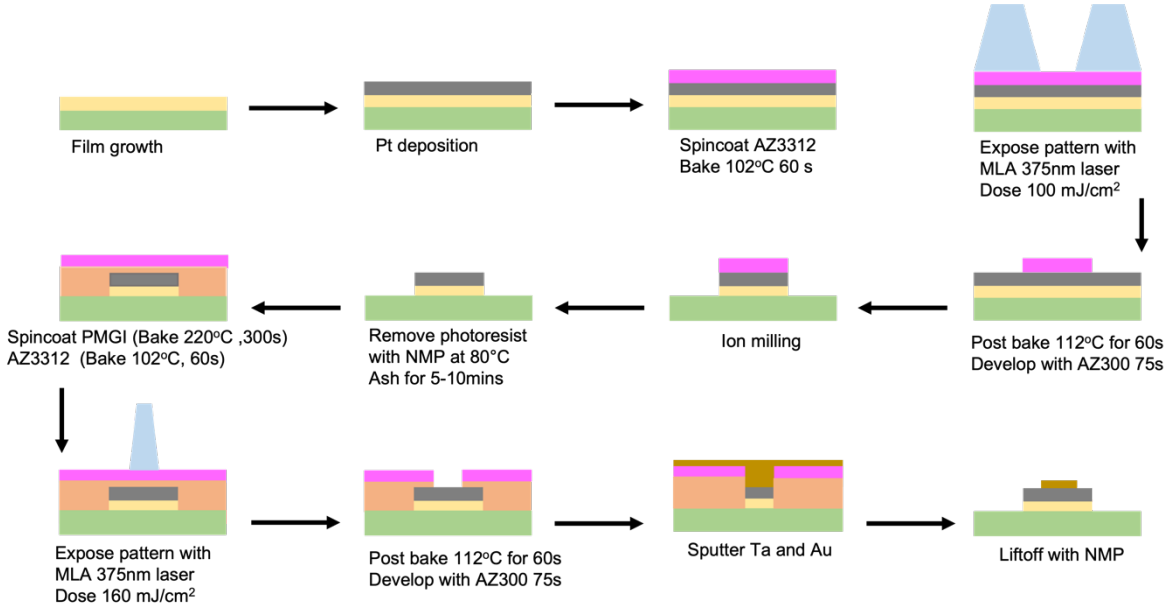

Figure 3-2: *Schematic plot of the device fabrication by lithography and lift-off.*

3.3 Thin film characterization

3.3.1 X-ray diffraction (XRD)

XRD was used to determine for phase identification, lattice mismatch, measurement of out-of-plane lattice parameters and thickness measurements (XRR). The XRD methods used in this thesis were 1DXRD (ω - 2θ) and X-ray reflectometry (XRR) . The tools of choice for the purpose of this thesis were the PANalytical X'Pert PRO MPD diffractometer for polycrystalline films and the HRXRD (Bruker D8 Discover diffractometer) for epitaxial film analysis.

For phase identification, ω - 2θ coupled scans were collected by x-ray detectors as shown in Fig. 3.2. The incident angle, ω, is defined between the X-ray source and sample and the diffracted angle, 2θ, is defined between the incident beam and detector angle. The coupled scan is a plot of scattered X-ray intensity vs 2Theta, but ω also changes linked to 2θ.

The same equipment that is optimized for HRXRD was used for XRR analysis to extract film thickness for the films. XRR is an x-ray measurement of glancing, but varying, incident angle and a matching detector angle that collects the X-rays reflected from the sample surface. Interference fringes (Laue fringes) in the reflected signal are used to find the film thickness. An XRR model based on the electron densities of the layers is constructed using Bruker Leptos software to fit the XRR measurement results. The model parameters including the thicknesses,

surface roughnesses and density of layers are varied to fit the experimental pattern. This measurement technique allows extracting film thicknesses and surface roughness's with in 0.1 nm.

Reciprocal space mapping (RSM) technique is used to get information about in-plane, out-of-plane lattice parameters and also strain state and defects in the epitaxially grown BiYIG films. RSM scans are performed by doing several ($2\theta - \omega$) scans for different tilt ($\Delta\omega$) values. A single coupled asymmetric scan yields enough data to extract in-plane and out-of-plane lattice parameters of both films and substrates. RSM is presented in terms of reciprocal space parameters that is proportional to inverse of lattice constants.

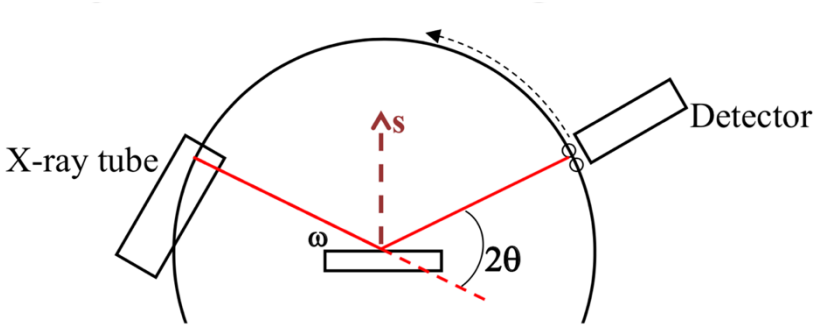

Figure 3-3: *Coupled ω - 2θ scan configuration.*[4]

3.3.2 Vibrating sample magnetometry (VSM)

The VSM is the most common method to measure magnetization of a sample as a function of an applied field. The VSM setup used in this thesis is shown in Fig. 3-4. The working principle of the VSM relies on Faraday's Law of electromagnetic induction, which states that the electromotive force generated in a pickup coil is proportional to the rate of change of the magnetic flux. The sample is attached to a diamagnetic sample holder (Pyrex glass) and placed between the pickup coils of the VSM where it is vibrated along the z direction with a constant frequency. The oscillating magnetic sample and the change to magnetization under the applied field will alter the magnetic flux through the pickup coils and induce a voltage which is converted into a magnetic signal (in emu). By ramping the field and measuring the

magnetization the sample's hysteresis loop can be measured. Calibration is done with a Ni standard as reference before each measurement to ensure the magnetic moment for a given voltage output is consistent with prior measurements.

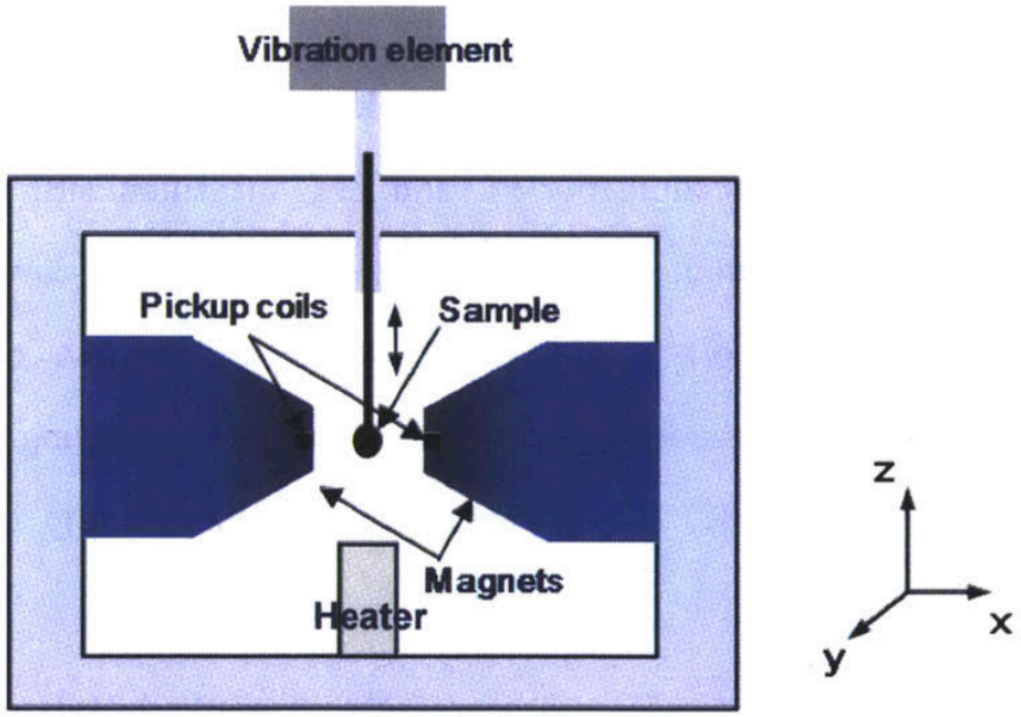

Figure 3-4: *VSM set-up.* [4]

3.3.3 Superconducting quantum interference device (SQUID)

A SQUID is a superconducting device that can measure an extremely small magnetic field, voltage or current. It is a very sensitive magnetometer in which a superconducting loop is used with one or more Josephson junctions. A squid magnetometer has a much higher sensitivity of 10^{-7} emu compared to that of VSM (10^{-5} emu). When a sample is moved up and down through the sensing coil a current proportional to the magnetic flux is induced in the ring. The schematic of a SQUID loop is shown in Fig. 3-5. Measurements may be obtained in the temperature range 1.8 to 400 K. SQUID was used to measure magnetization as a function of temperature to study the compensation temperature of TbIG, CeTbIG and BiTbIG films.

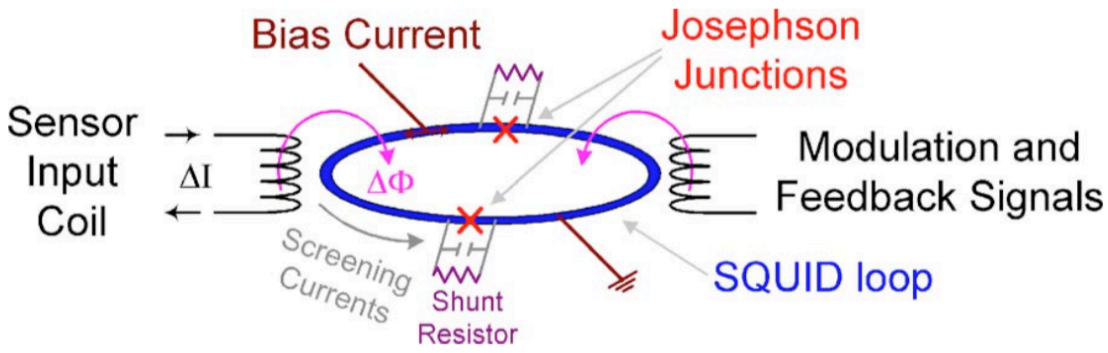

Figure 3-5: *SQUID loop.*[5]

3.3.4 Faraday Rotation

The Faraday rotation of the garnet thin films were characterized on a custom-built apparatus at 1550nm wavelength with the laser light and magnetic field directions perpendicular to the film plane. Fig. 3-6 shows a schematic of the Faraday rotation set-up used in this work. The sample is placed between the pole pieces of an electromagnet. An infrared laser light with wavelength of 1550nm is linearly polarized by a polarizer and modulated at 1000 Hz by a Faraday cell modulator controlled with a lock-in amplifier. The linearly polarized light then passes through a hole bored into the first electromagnetic coil and then through the sample. After exiting the sample the light passes through the second electromagnetic coil through an analyzer set at 1° off from extinction. The transmitted light signal is detected by a Ge detector, filtered by a band pass filter and shown on the lock-in amplifier and oscilloscope. By scanning the magnetic field with the LabView interface control, the Faraday rotation hysteresis of the sample is collected. The Faraday rotation value is determined by calibrating the signal intensity on the lock-in amplifier. Calibration is done by rotating the first polarizer between the laser and the modulator to 1° and then reading out the lock-in amplifier voltage for the sample due to 1° rotation. This value is then entered into the LabView interface. The rotation angle is assumed to be linearly proportional to the signal intensity for thin films with small rotation angles,

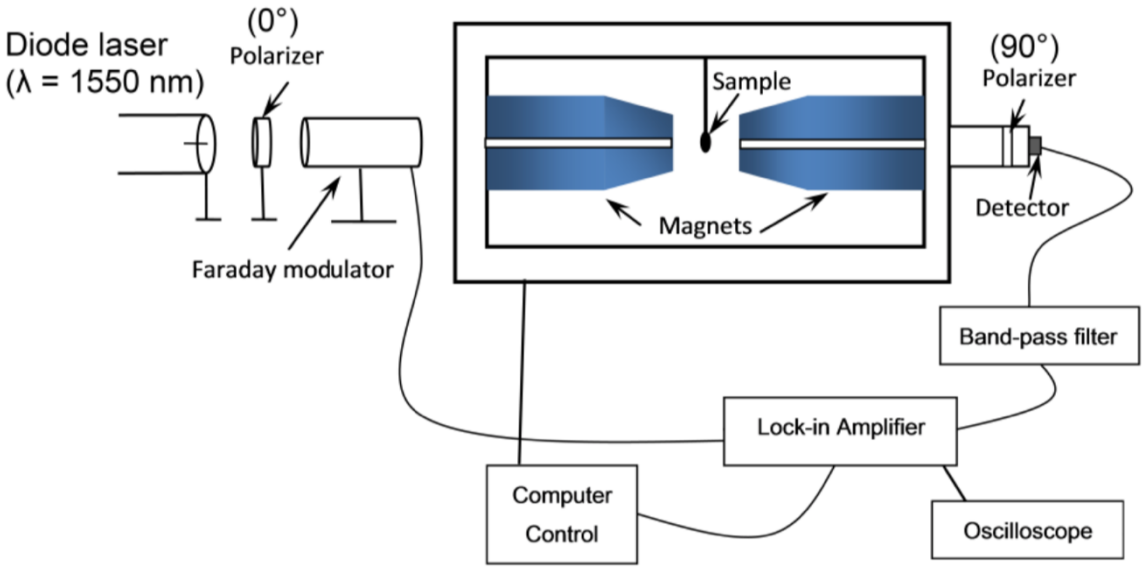

Figure 3-6: *Faraday rotation measurement set-up.*[6]

3.3.5 Ellipsometry

The refractive index n and extinction coefficient $\boldsymbol{k}$ of polycrystalline iron garnet thin film systems were characterized using a spectroscopic ellipsometer (J.A. Woollam RC2) for three light incident angles ranging from 55 ˚ to 65 ˚. A plot of the experimental set-up is shown in Fig. 3-7. The incident light is linear with both p- and s- components. The reflected light has undergoes amplitude and phase changes for both p- and s- polarized light, and ellipsometry measures the change in polarization as light reflects or transmits from a material surface. The polarization change of the reflected light (ρ) is represented as a change in the ratio of amplitude , Ψ, and phase difference, Δ, between p- and s- polarized light:

$$\rho = \tan(\Psi)\, e^{-i\Delta} = \frac{r_p}{r_s}$$

Here, r_p and r_s are the ratios of the amplitude of reflected wave to the incident wave for p- and s- polarizations respectively. The parameters Ψ, Δ are measured by changing the polarizer and

analyzer angles and recorded as a function of wavelength. The optical constants are obtained by fitting the spectrum with the Cody-Lorentz model. The spectral dependence of complex refractive index (N = n+ik) of each garnet layer was parametrized by the sum of 4 Cody-Lorentz oscillators and their parameters were fitted together with the layer thickness and surface roughness. The mean squared error (MSE) parameter used to describe the fitting accuracy by comparing the fitted Ψ and Δ to measured results was found to be MSE < 1 for all the films reported in this thesis.

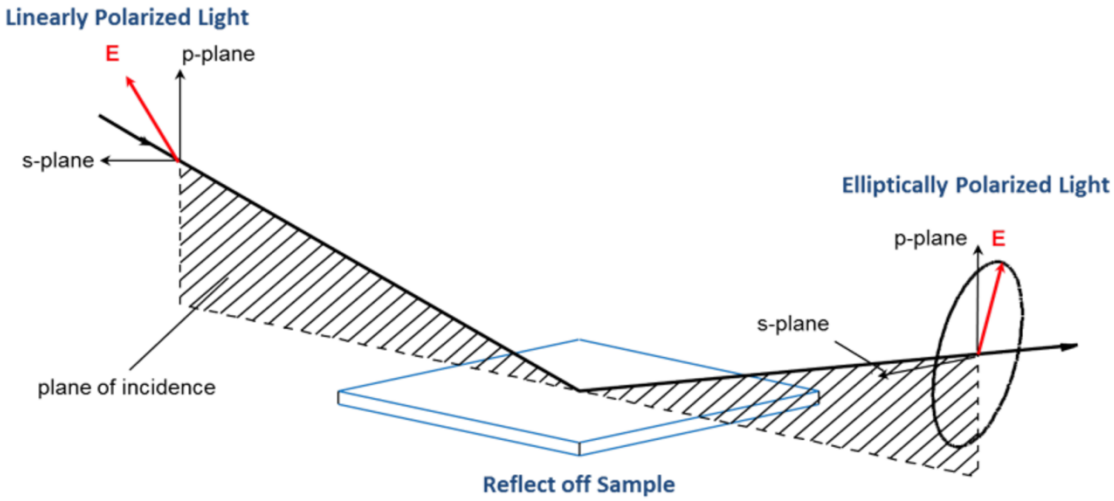

Figure 3-7: *A schematic plot of the ellipsometry measurement set-up.* [7]

3.3.6 Ferromagnetic Resonance (FMR) characterization

Magnetization dynamics is modeled using the Landau-Lifshitz-Gilbert equations (LLGE). LLGE describes the time rate of change of the normalized magnetisation ($\boldsymbol{m} = \frac{M}{M_s}$) given by:

$$\frac{\delta \boldsymbol{m}}{\delta t} = -|\gamma| \boldsymbol{m} \times \boldsymbol{H}_{eff} + \alpha \boldsymbol{m} \times \frac{\delta \boldsymbol{m}}{\delta t}$$

Here, γ is the gyromagnetic ratio , α is the Gilbert damping parameter and $\boldsymbol{H}_{eff}$ is the "effective magnetic field" that exerts a torque on the magnetic moment and causes it to precess about it. The first term on the right-hand side of the LLGE is the precessional term. The second term is the damping term that aligns the magnetization towards $\boldsymbol{H}_{eff}$ as shown in Fig. 3.8. The damping parameter alpha is a measure of how fast the precession decays and aligns to $\boldsymbol{H}_{eff}$.

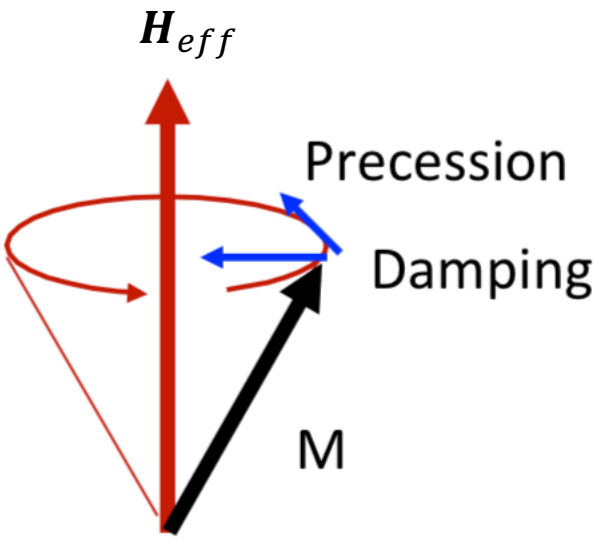

Figure 3.8: *Magnetization dynamics of a moment with an applied magnetic field.*

To extract the damping of the BiYIG and BiYIG-TmIG thin films their dynamic magnetic properties were studied with broadband perpendicular FMR spectroscopy based on the vector network analyzer (VNA) technique [8-10]. The samples were placed face-down on a 50 Ω coplanar waveguide. A static out-of-plane magnetic field up to $\mu_0 H$ = 2.2 T was swept to saturate the film in the out-of-plane direction. A variable microwave field was applied in-plane

while the microwave transmission over a frequency from 10-40 GHz was measured. The complex transmission parameter S_{21} was measured at a fixed frequency while the external magnetic field was swept [8] . The resonance field for the films were fitted to the Kittel equation for perpendicular geometry to extract the effective magnetization M_{eff} and the Landé g-factor g [11] for a chosen film. Here:

$$H_{res} = \frac{2\pi f}{|\gamma|\mu_0} + M_{eff}$$

where, H_{res} is the resonance field, f is the excitation frequency, and γ is the gyromagnetic ratio $(g\mu_B)/\hbar$ where μ_B is the Bohr magneton and ħ is the reduced Planck's constant. The anisotropy of the films , K_u, is extracted from M_{eff} from the equation [12,13]

$$M_{eff} = M_s - \frac{2K_u}{\mu_0 M_s}$$

The damping α was extracted by fitting the linewidth to the following expression:

$$\Delta H = \frac{4\pi\alpha f}{|\gamma|\mu_0} + \Delta H_0$$

where ΔH is the experimentally observed linewidth determined from fitting the S_{21} data with the complex susceptibility and ΔH_0 is the inhomogeneous broadening of the linewidth.

3.2.6 Brillouin light scattering (BLS)

DMI in a film manifest itself as the nonreciprocal propagation for spin waves i.e. for a given wavelength two counterpropagating spin waves have different frequencies when the magnetization is in plane and the wavevector is perpendicular to the magnetization. This asymmetric dispersion can be measured directly by Brillouin light scattering (BLS). In BLS measurements, a laser is focused onto a sample, and the photons are inelastically backscattered by the spin waves. Momentum conservation means that magnons with momentum $|k| = \frac{4\pi}{\lambda}\sin\theta$(where λ is the wavelength of the laser and θ is the light incident angle with the film normal) propagating towards the incoming laser beam are annihilated (anti-Stokes process),

and magnons propagating in the opposite direction are created (Stokes process) as shown in Fig. 3-9. The reflected light shows a shift in frequency, altering the dispersion relation. In a symmetric material containing no DMI, clockwise spin waves propagating in the +x direction and counterclockwise spin waves propagating in the -x direction occur in equal amounts. Nembach *et al.* [14] *reports for* an in-plane magnetized film with spin waves propagating perpendicular to the magnetization direction, the DMI alters the spin wave frequency according to:

$$f = f_o + \Delta f_{DMI}$$

where f_o is the spin-wave frequency in the absence of the DMI and

$$\Delta f_{DMI} = \frac{2\gamma}{\pi M s} Dk \text{ [15]}$$

where γ is the gyromagnetic constant, Ms is the saturation magnetization and D is the DMI constant.

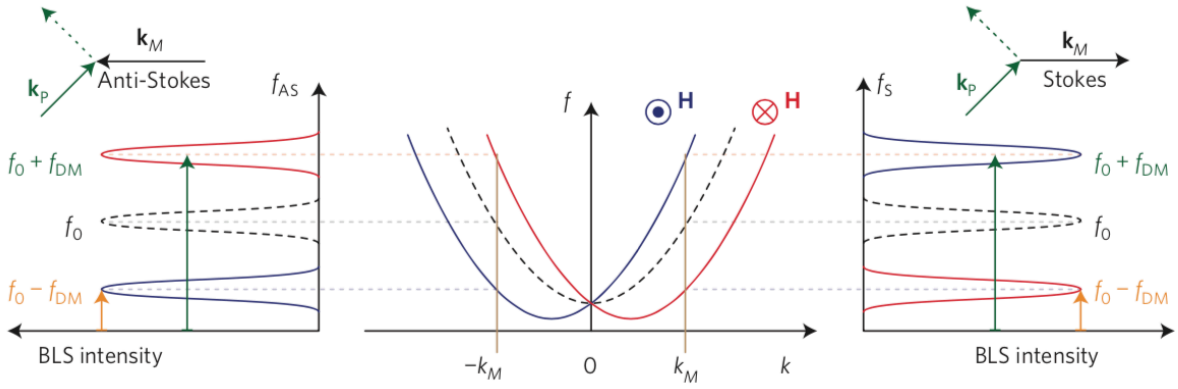

Figure 3.9: *The central image shows a spin wave dispersion in the absence (dashed) and presence (solid) of DMI. The left and right sketch show BLS spectra for anti-stokes and stokes processes.* [14]

The BLS measurements were performed using a Sandercock-style (3+3) tandem Fabry-Pérot interferometer [16] and 532 nm continuous-wave laser. The Damon-Eshbach geometry was employed [17], with an external field applied in the in-plane direction of the sample and

perpendicular to the spin wave propagation direction. Thermally excited spin waves were detected at room temperature hrough a frequency-shift of the backscattered light, collected and analyzed through the interferometer.

3.2.7 Spin Magnetoresistance measurement

Hall crosses of dimensions 50 µm × 40 µm were fabricated using mask less lithography as described in section 2.2. A home made four-point probe was used to perform spintronics measurement. A DC sensing current of 1 mA was used for Hall resistance measurement with an out-of-plane field sweep from -150 Oe to 150 Oe.

3.2.8 Magneto-optical Kerr effect microscopy

Polar MOKE microscopy was acquired in a custom-built Kerr microscope with independent out-of-plane and in-plane magnetic field controls. The in-plane magnetic field was controlled via a water-cooled, Fe-cored electromagnet with a magnetic field feedback loop while the out-of-plane magnetic field was controlled via an air-core electromagnet. The sample stage had high-precision angular adjustment for eliminating out-of-plane contributions from the in-plane magnet. Differential wide-field MOKE microscopy was performed using a light-emitting diode white-light source focused with a 10x objective.

References

[1] R. A. Waldo, Microbeam Anal. 1988, 23, 310.

[2] Dijkkamp, D., Venkatesan, T., Wu, X.D., Shaheen, S.A., Jisrawi, N., Min-Lee, Y.H., McLean, W.L. and Croft, M., 1987. Preparation of Y-Ba-Cu oxide superconductor thin films using pulsed laser evaporation from high T c bulk material. *Applied Physics Letters*, *51*(8), pp.619-621.

[3] Tang, A.S., 2018. *Effect of nonstoichiometry on the magnetism and ferroelectricity of Fe- and Co-substituted strontium titanate thin films* (Doctoral dissertation, Massachusetts Institute of Technology).

[4] Bi, L., 2011. *Magneto-optical oxide thin films and integrated nonreciprocal photonic devices* (Doctoral dissertation, Massachusetts Institute of Technology).

[5] Fagaly, R.L., 2006. Superconducting quantum interference device instruments and applications. *Review of scientific instruments*, *77*(10), p.101101.

[6] Onbasli, M.C., 2015. Magneto-optical and multiferroic oxide thin films, integrated nonreciprocal photonic devices and multiferroic memory devices (Doctoral dissertation, Massachusetts Institute of Technology).

[7] https://www.jawoollam.com/resources/ellipsometry-tutorial/ellipsometry-measurements

[8] Nembach, H.T., Silva, T.J., Shaw, J.M., Schneider, M.L., Carey, M.J., Maat, S. and Childress, J.R., 2011. Perpendicular ferromagnetic resonance measurements of damping and Land e´ g− factor in sputtered (Co 2 Mn) 1− x Ge x thin films. *Physical Review B*, *84*(5), p.054424.

[9] Ding, Y., Klemmer, T.J. and Crawford, T.M., 2004. A coplanar waveguide permeameter for studying high-frequency properties of soft magnetic materials. *Journal of applied physics*, *96*(5), pp.2969-2972.

[10] Neudecker, I., Woltersdorf, G., Heinrich, B., Okuno, T., Gubbiotti, G. and Back, C.H., 2006. Comparison of frequency, field, and time domain ferromagnetic resonance methods. *Journal of Magnetism and Magnetic Materials*, *307*(1), pp.148-156.

[11] Nakamura, N., Ogi, H., Hirao, M., Fukuhara, T., Shiroki, K. and Imaizumi, N., 2008. Elastic constants of single-crystal rare-earth bismuth iron garnet films. *Japanese Journal of Applied Physics*, *47*(5S), p.3851.

[12] Wu, C.N., Tseng, C.C., Fanchiang, Y.T., Cheng, C.K., Lin, K.Y., Yeh, S.L., Yang, S.R., Wu, C.T., Liu, T., Wu, M. and Hong, M., 2018. High-quality thulium iron garnet films with tunable perpendicular magnetic anisotropy by off-axis sputtering–correlation between magnetic properties and film strain. *Scientific reports*, *8*(1), pp.1-8.

[13] R. O'Handley, *Modern Magnetic Materials: Principles and Applications*, 1st ed. (Wiley, New York, NY, 1999).

[14] Nembach, H.T., Shaw, J.M., Weiler, M., Jué, E. and Silva, T.J., 2015. Linear relation between Heisenberg exchange and interfacial Dzyaloshinskii–Moriya interaction in metal films. *Nature Physics*, *11*(10), pp.825-829.

[15] Ma, X., Yu, G., Tang, C., Li, X., He, C., Shi, J., Wang, K.L. and Li, X., 2018. Interfacial dzyaloshinskii-moriya interaction: Effect of 5 d band filling and correlation with spin mixing conductance. *Physical review letters*, *120*(15), p.157204.

[16] Damon, R.W. and Eshbach, J.R., 1961. Magnetostatic modes of a ferromagnet slab. *Journal of Physics and Chemistry of Solids*, *19*(3-4), pp.308-320.

[17] Hillebrands, B., 1999. Progress in multipass tandem Fabry–Perot interferometry: I. A fully automated, easy to use, self-aligning spectrometer with increased stability and flexibility. *Review of scientific instruments*, *70*(3), pp.1589-1598

4. Magneto-optical Bi:YIG films for integrated photonics

4.0 Introduction and Motivation

As discussed in chapter 2, the rapid development of optical fiber communication systems has prompted the growing demand for on-chip optical isolation in photonic integrated circuits (PICs) . [1-6] Discrete isolators rely on Faraday rotation, i.e. a non-reciprocal mode conversion, but in PICs the use of nonreciprocal phase shift (NRPS) in a resonator or interferometer device is preferable to avoid problems caused by the birefringence of optical waveguides. The active material in these isolator devices is commonly a magneto-optical (MO) iron garnet material, in particular yttrium iron garnet (YIG, $Y_3Fe_5O_{12}$) with substituents such as Ce or Bi to increase the MO performance.[5-15]

However, the integration of garnets on a Si (or other semiconductor) platform is challenging due to the incompatible lattice parameters and the thermal expansion mismatch between garnets and common semiconductor substrates.[6-16] Moreover, crystallization of the garnet phase usually requires a high thermal budget. Garnets formed on semiconductor substrates are polycrystalline and exhibit higher optical absorption than single crystal films. Furthermore, impurity phases such as $YFeO_3$, Fe_2O_3 and Bi_2O_3 can form during the crystallization process,[17] which contributes to optical loss. These factors result in inferior optical performance of polycrystalline MO garnet films compared to the bulk garnet material, and a lower figure of merit (FoM), defined as the ratio of the Faraday rotation to the absorption coefficient per length of the material.

Considerable work has been done on growth of garnet films on semiconductors to enable demonstrations of isolators and modulators.[6-16] The first monolithically integrated optical isolator [6] used 80 nm thick Ce:YIG which was grown by pulsed laser deposition (PLD) on a pre-annealed 20 nm thick YIG seed layer to induce crystallization of the Ce:YIG. A simplified PLD process was introduced by Sun et al.[11] where the YIG seed layer was placed on top of the MO garnet and both layers were crystallized simultaneously by rapid thermal annealing (RTA). This top-seedlayer process places the MO garnet in direct contact with the underlying Si waveguide, maximizing the coupling of light from the waveguide to the MO cladding, but

The work in this chapter was published in Advanced Optical Materials, 2019, 7(13), p.1900056.

has only been applied to Ce:YIG. Recently rare-earth garnets have been developed that crystallize on Si and quartz without a seed layer, including sputter-deposited terbium iron garnet (TIG) and Bi-doped TIG (Bi:TIG).[18,19]

Growth of MO materials on the sidewall of the waveguide can enable a wider range of device designs, including isolators for TE (transverse electric) polarization. Integrated semiconductor lasers emit TE-polarized light, and TE mode isolation using NRPS requires placement of the MO material on the sidewall of the waveguide to break left-right symmetry.[18,20,21] However, the NRPS-based integrated optical isolators that have been experimentally demonstrated are made with the MO material on the top or bottom surface of the waveguide, which isolates only the TM (transverse magnetic) polarization.[6-8,11-14] It is therefore essential to establish deposition conditions that yield well-crystallized MO garnet on the sidewalls of waveguides to facilitate TE-mode isolation without requiring additional mode converters.

Ce:YIG is the most commonly used MO material for integrated optical isolators designed to operate at 1550 nm. However, Ce:YIG has an absorption peak from a Ce transition near 1.3 eV with a notable tail extending into the IR, leading to a decreasing FoM as the wavelength is reduced below 1550 nm.[13,22] Bi:YIG lacks this absorption peak, making it favorable for isolators in the lowest dispersion 1300 nm wavelength range,[6,7,13] and bulk Bi:YIG is the material of choice in discrete isolators. Single-crystal Bi:YIG has been extensively characterized.[23-35] Epitaxial Bi:YIG films on $Gd_3Ga_5O_{12}$ (GGG) (111) substrates exhibited a Faraday rotation angle Θ_f proportional to the Bi content.[24] Complete substitution of bismuth in YIG can increase the Faraday rotation by as high as two orders of magnitude at 633 nm wavelength in comparison to YIG.[23, 32, 45] The Bi^{3+} ion has high spin orbit coupling that increases excited state splitting, raising the Faraday rotation.[34] Although polycrystalline Bi:YIG has been grown and characterized,[6, 7, 33, 36-40] its reported FoM is well below that of bulk Bi:YIG and there has been no systematic study of its FoM as a function of composition or deposition parameters.

In this chapter we report the growth and optical properties of epitaxial and polycrystalline thin films of Bi-substituted yttrium iron garnet ($Bi_xY_{3-x}Fe_5O_{12}$, Bi:YIG) synthesized using PLD on GGG and Si substrates. The optimum growth conditions for epitaxial films and the effect of growth temperatures and O_2 pressure on the film stoichiometry was studied. The key results are demonstrations of the highest reported FoM of polycrystalline Bi:YIG films; the top-down seedlayer process for Bi:YIG; and the sidewall growth of Bi:YIG. The microstructure and

The work in this chapter was published in Advanced Optical Materials, 2021, p.2100512.

stoichiometry of the films grown on the top surface and on the sidewalls of waveguide structures was compared to address the challenges of developing TE mode optical isolators.

4.1 Characterization of Bi:YIG/GGG

4.1.1 Structural Characterization

We first describe the PLD growth, structure and properties of single crystal Bi:YIG films grown on GGG. Bi:YIG films of thickness 30 to 100 nm grew epitaxially on the substrate according to XRD analysis. The Bi:YIG and YIG films were deposited on double-side polished silicon (100) and GGG(100) substrates using a 248nm wavelength KrF excimer laser (Coherent, COMPex Pro 205). The $Bi_xY_{3-x}Fe_5O_{12}$ (x = 0.8, 1.2, 1.5) and $Y_3Fe_5O_{12}$ targets were prepared by sintering of mixed oxide powders.[11] The chamber was pumped to 5 × 10^{-6} Torr base pressure prior to introducing oxygen and depositing the films. The laser repetition rate was 10 Hz, the laser fluence was ~2 J/cm^2, and the target-substrate distance was 6 cm. A range of different substrate temperatures (480-650^{o}C) and O_2 pressures (5-100mTorr) were used. The high crystalline quality of the epitaxial films is evident from the Laue fringes present in the HRXRD symmetric scans around the Bi:YIG and GGG (400) peaks as shown in Fig. 4-1a. The out-of-plane lattice parameters of $Bi_xY_{3-x}Fe_5O_{12}$ grown from targets with x = 0.8, 1.2 and 1.5 and at 20mTorr oxygen pressure and substrate temperature of 560^{o}C were 12.41 Å, 12.50 Å and 12.56 Å respectively in agreement with previous reports.[23,24,33]

4.1.2 Effect of Temperature and Oxygen Pressure on Stoichiometry

The effects of substrate temperature (T_s) and oxygen pressure (P_{O_2}) on film composition are shown in Fig. 4-1b and c. The cation content of the films was measured by wavelength dispersive spectroscopy and characterized by the Bi:Y ratio and by (Bi+Y)/Fe which is ideally 0.6. Films grown on Si during the same deposition run showed the same cation ratios found in films grown on GGG.

High T_s and/or low P_{O_2} lead to a lower bismuth content whereas low T_s and/or high P_{O_2} result in bismuth-rich films as shown in Fig. 4-1d. This bismuth deficiency at higher T_s is attributed to the volatility of bismuth, and similar behavior has been observed in $BiFeO_3$ films.[41,42] The pressure dependence is related to scattering of the ablated species by the oxygen in the chamber. Fe is lighter than Bi and is scattered more effectively, accounting for the Fe deficiency at higher P_{O_2}. Increasing oxygen pressure also lowered the ratio of Fe to Y. As a result, for constant

temperature the (Bi+Y):Fe ratio is much less than 0.6 at lower P_{O_2} but increases with P_{O_2} as shown in Fig. 4-1d.

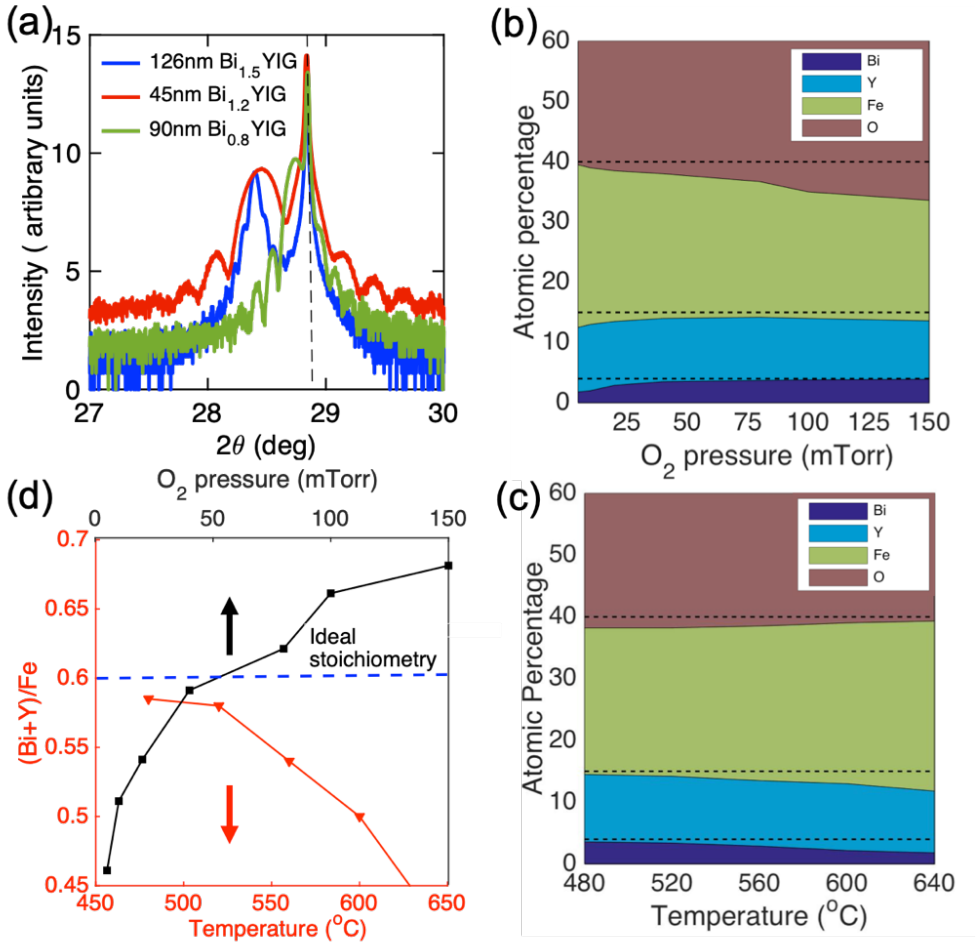

Figure 4-1: *(a) HRXRD ω −2Θ scans around the Bi:YIG (400) and GGG (400) peaks for films grown at 560 °C and 100mTorr pressure. Dashed line indicates the (400) peak of bulk GGG. (b) Effect of oxygen pressure on composition of films grown from a target composition of* $Bi_{0.8}Y_{2.2}Fe_5O_{12}$ *at 560 °C, repetition rate 10 Hz and laser fluence of 2 J/cm². (c) Effect of substrate temperature on composition of films grown from target composition of* $Bi_{0.8}Y_{2.2}Fe_5O_{12}$ *at 20 mTorr, repetition 10 Hz and laser fluence of 2 J/cm². (d) The corresponding (Bi+Y)/Fe ratios in (b) and (c) plotted as a function of temperature (red) and* O_2 *pressure (black).*

The (Bi+Y):Fe ratio was close to the stoichiometric ratio of 0.6 at growth temperatures of 520-600°C at P_{O_2} of 20 mTorr (Fig. 4-1d) and XRD analysis confirms formation of single phase garnet in this temperature range. While a single phase garnet without secondary phases was formed at all oxygen pressures between 10-100mTorr, the Bi-rich films at higher oxygen pressures have improved magneto-optical characteristics (Fig. 4-2d).

4.1.3 Magnetic and Magneto-optical Characterization

The single crystal films grown on GGG have a saturation magnetization of approximately 120 cmu cm^{-3} (Fig. 4-2a and 4-2b), similar to previous reports,[6,7] and Faraday rotation up to 3000° cm^{-1} at 1550 nm wavelength, Fig. 4-2c. The Faraday rotation increased linearly with the bismuth content as reported previously.[24] Hence, the Faraday rotation can be increased by using a target with higher Bi content or by depositing at a higher oxygen pressure to enhance Bi incorporation into the films. In Fig. 4-2f, the Faraday rotation versus wavelength for Bi:YIG/GGG is typical of bulk Bi:YIG with absorption in the visible-ultra violet region due to Fe transitions, and an absorption tail extending into the IR.[34,35, 44-46]

Table 4-1. Growth conditions and stoichiometry of garnet films on GGG and Si.

Sample	Substrate	Target	P_{O2} (mTorr)	Temperature (°C)	Film Thickness (nm)	Bi:Y:Fe
G1	GGG	$Bi_{1.2}Y_{1.8}Fe_5O_{12}$	150	520	104	1:1.6:3.6
G2			100		110	0.9: 2:4
G3			20		130	0.65:2.2:4.6
G4		$Bi_{1.5}Y_{1.5}Fe_5O_{12}$	100	560	126	1.4:1:4.2
G5		$Bi_{1.2}Y_{1.8}Fe_5O_{12}$	150	560	75	1.1:1.4:4
G6		$Bi_{0.8}Y_{2.2}Fe_5O_{12}$	100	560	90	0.7:1.9:4
S1	Si	$Bi_{0.8}Y_{2.2}Fe_5O_{12}$	100	560	YIG(37)/BiYIG(88)/Si	
S2		$Bi_{1.2}Y_{1.8}Fe_5O_{12}$	100	560	YIG(40)/BiYIG(80)/Si	
S3		$Bi_{1.5}Y_{1.5}Fe_5O_{12}$	100	640	YIG(50)/BiYIG(90)/Si	
S4		$Bi_{0.8}Y_{2.2}Fe_5O_{12}$	100	560	BiYIG(85)/YIG(20)/Si	
S5		$Bi_{1.2}Y_{1.8}Fe_5O_{12}$	100	560	BiYIG(90)/YIG(25)/Si	
S6		$Bi_{1.5}Y_{1.5}Fe_5O_{12}$	100	600	BiYIG(100)/YIG(40)/Si	

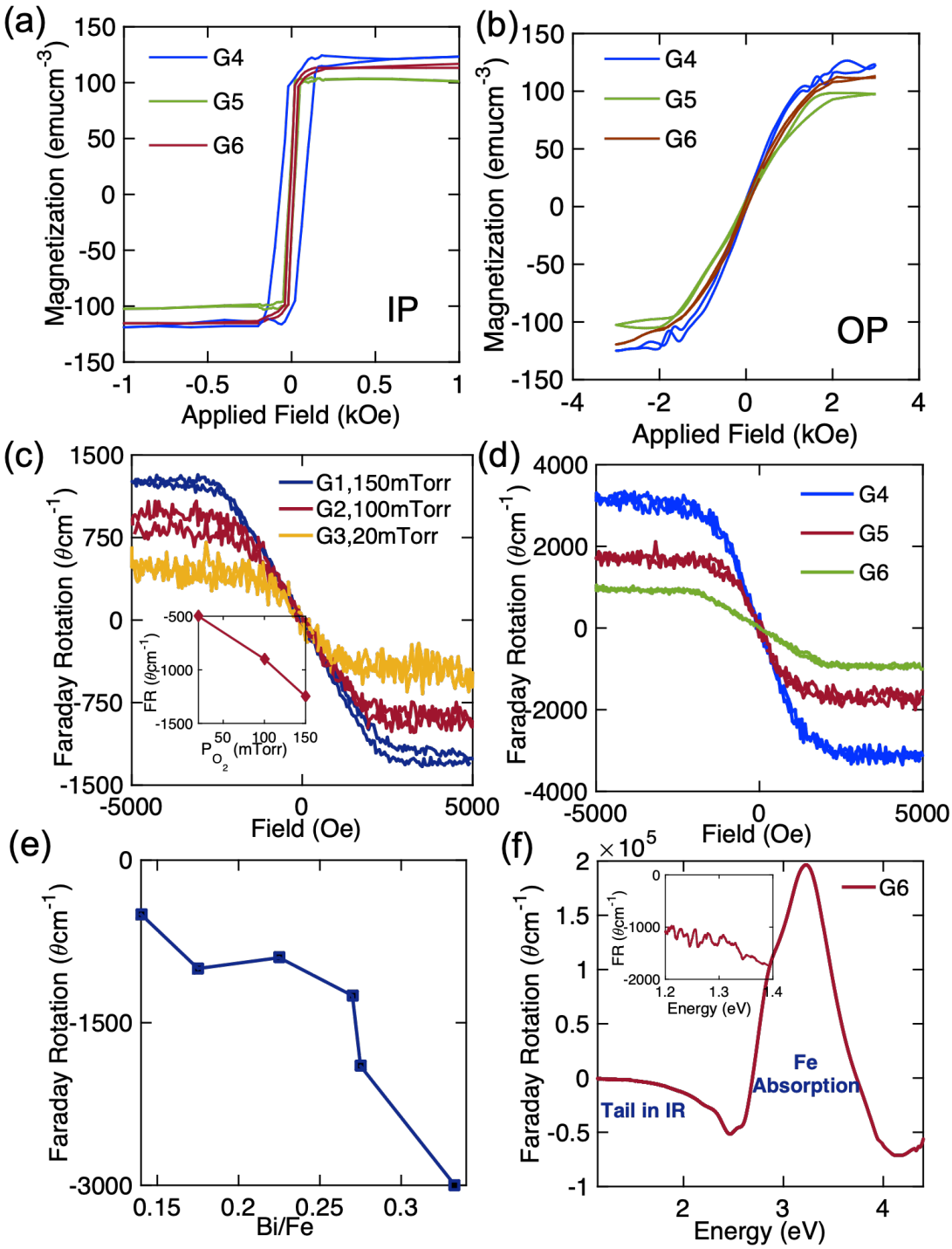

Figure 4-2: *(a) In-plane (IP) and (b) out-of-plane (OP) hysteresis loops for epitaxial films grown from targets of varying bismuth content. (c) Out-of plane Faraday rotation hysteresis loops at 1550 nm for films grown at 520°C, 1.9J/cm² at various oxygen pressures from a* $Bi_{1.2}Y_{1.8}Fe_5O_{12}$ *target. (d) Out-of plane Faraday rotation hysteresis loops at 1550 nm for epitaxial Bi:YIG films made from* $Bi_{0.8}Y_{2.2}Fe_5O_{12}$, $Bi_{1.2}Y_{1.8}Fe_5O_{12}$ and $Bi_{1.5}Y_{1.5}Fe_5O_{12}$ *targets.* (e) *Faraday rotation versus Bi/Fe ratio of epitaxial films. (f) Faraday rotation spectrum of an epitaxial film made from a* $Bi_{0.8}Y_{2.2}Fe_5O_{12}$ *target.*

4.2 Characterization of Bi:YIG/Si

4.2.1 Structural Characterization, Surface Morphology and Crystal Quality

We now discuss the properties of Bi:YIG films grown on Si substrates by PLD from the same three targets of composition $Bi_{0.8}Y_{2.2}Fe_5O_{12}$, $Bi_{1.2}Y_{1.8}Fe_5O_{12}$ and $Bi_{1.5}Y_{1.5}Fe_5O_{12}$. The films grown on Si underwent rapid thermal annealing (RTA, Modular Process Tech, RTP-600S) at 800 °C for 5 min. Annealing of single layer Bi:YIG films did not produce a garnet phase, but inclusion of a YIG seed layer led to crystallization into garnet as shown previously for Ce:YIG.[6,7] Bilayers consisting of Bi:YIG with a YIG seed layer below or above the Bi:YIG are referred to as bottom-up or top-down, respectively (Fig. 4-3a). Layer thicknesses are given in Table 4-1.

Fig. 4-3b shows the XRD pattern for bottom-up and top-down crystallized bilayers after RTA at 800 °C for 5 min. While the bottom-up crystallized films form no secondary phases the top-down crystallized films contain secondary phases in the form of Bi_2O_3 and Fe_2O_3. We suggest that in the top-down crystallization process the escape of volatile Bi during annealing is limited by the capping YIG seed layer and the excess Bi forms the secondary Bi_2O_3 phases. The introduction of an additional annealing step in the PLD chamber after the growth of the Bi:YIG layer but before the YIG was deposited allows part of the Bi to escape and prevents the formation of secondary phases as shown in Fig. 4-3b. The excess Bi in the top-down bilayers was alternatively avoided by co-depositing iron oxide from a separate target during growth. However, this process resulted in a slight excess of Fe_2O_3 in the film as shown in Figure 3b. XRD data for a broad range of angles ($2\theta = 20^o$ to 50^o) for the polycrystalline films further confirms the presence of secondary phases only in the top-down crystallized Bi:YIG films that were not PLD annealed or co-deposited with Fe_2O_3 as shown in Fig. 4-4. The SEM and AFM surface morphology of the bilayer films of YIG/Bi:YIG/Si and Bi:YIG/YIG/Si are shown in Fig. 4-3c and Fig. 4-3d. For the YIG/Bi:YIG/Si, the grain size at the top surface is on the order of 5 μm, whereas in Bi:YIG/YIG/Si the grain size is on the order of 2 μm.

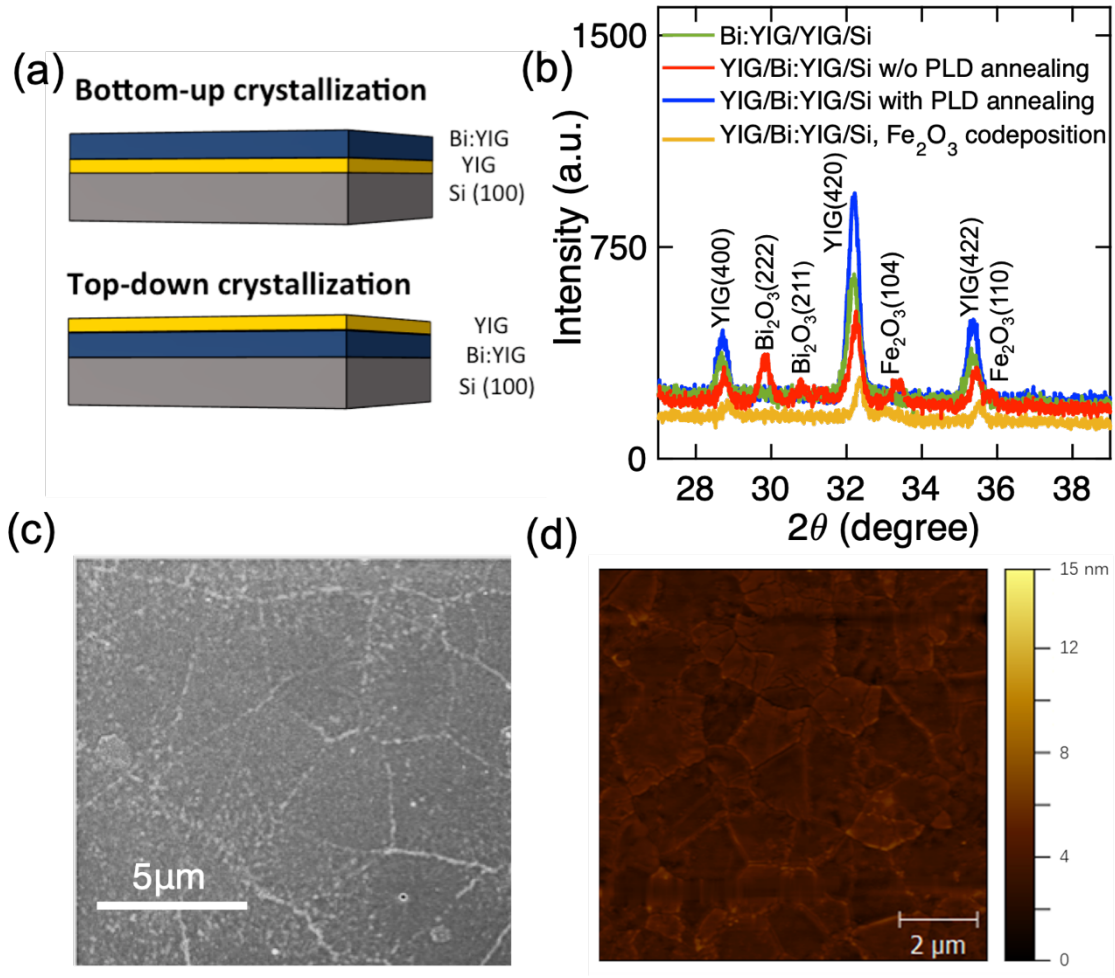

Figure 4-3: *(a) Schematic of bottom-up and top-down crystallized films. (b) XRD ω−2θ scans for polycrystalline Bi:YIG films on silicon after RTA. (c) SEM image of crystallized top surface of YIG/Bi:YIG/Si film after rapid thermal annealing. (d) AFM image of Bi:YIG/YIG/Si film after rapid thermal annealing, with color scale showing the height.*

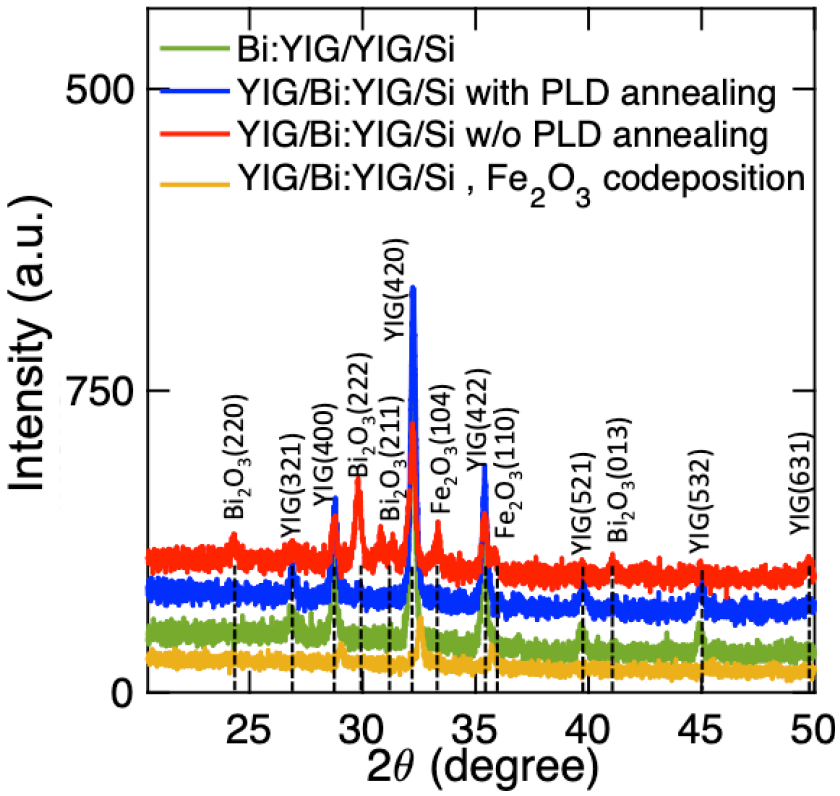

Figure 4-4: *XRD ω−2θ scans for polycrystalline Bi:YIG films on silicon after RTA for a broad range of 2θ angles from 20° to 50°.*

Fig. 4-5a shows the cross-sectional SEM image of top-down crystallized YIG (50nm)/Bi:YIG (150nm)/substrate grown on a waveguide of a TE mode optical test device. TE-mode optical isolation requires symmetry breaking that is transverse to the waveguide and therefore sidewall garnet growth is necessary.[47] The garnet covers both the top surface and the sidewalls, but the layer on the sidewall of the trench is thinner than the layer on the flat surface of the device. Moreover, the sidewall coverage of garnet on either side of the trench is significantly different because the trench was not placed directly above the plume during deposition. By rotating the substrate during deposition a much more uniform side wall coverage on both sides of the trench is obtained as shown in the cross-sectional TEM image of YIG (100nm)/Bi:YIG(100nm)/substrate in Fig. 4-5b. Fig. 4-5a also confirms that the Bi:YIG layer shows internal contrast, presumably from grain boundaries, and has a smaller grain size than

the YIG capping layer.

A bright-field TEM cross-sectional image of YIG/Bi:YIG film on amorphous SiO_2 is shown in Fig. 4-5c. The Au and Pt layers were added during sample preparation prior to cutting the sample using the FIB. A high-resolution (HR) TEM image of the interface between the YIG and the Bi:YIG layer is shown in Fig. 4-5d. Fig. 4-5e and Fig. 4-5f show selected area diffraction (SAD) pattern of the garnet grown on the flat surface of the device taken along the $[0\bar{1}\bar{1}]$ zone axis and of sidewall garnet along the $[\bar{1}11]$ zone using apertures indicated in Fig. 4-5b in orange and red respectively. The SAD patterns show diffraction spots consistent with the garnet structure, and their spacing yielded interplanar spacings of d_{321}= 3.34 Å, d_{422}= 2.55 Å, d_{400}= 3.10Å close to the lattice spacings from XRD. (d_{321}= 3.31 Å, d_{422}= 2.52 Å, d_{400}= 3.09Å).

Fig. 4-6 shows the elemental mapping of Fe, Y, O, Bi and Au in the top-down YIG/Bi:YIG/Si from the scanning transmission electron microscope sample together with a bright field TEM image. The distribution of Fe and Y is uniform throughout the YIG and Bi:YIG layers. However, the Fe distribution on the sidewall includes Fe-rich regions as shown in Fig. 4-7. The Bi map suggests interdiffusion of Bi into the YIG layer. The false signal in the Bi map at the top of the Bi:YIG film is due to an overlap of the Bi Mα peak with the Au Lα peak.

4.2.2 Magnetic and Magneto-optical Characterization

The polycrystalline films grown with both top and bottom seed layers on planar Si substrates had bulk-like magnetic moment (Fig. 4-8a and 4-8b) and Faraday rotation up to $2000^{o}cm^{-1}$ at 1550 nm was achieved for top-down crystallized films grown from the $Bi_{1.5}Y_{1.5}Fe_5O_{12}$ target (Fig. 4-8c). The high Faraday rotation of the films S3 and S6 is attributed to the increased Bi content from the $Bi_{1.5}Y_{1.5}Fe_5O_{12}$ target.[24,34,35,45] For all the polycrystalline films the Faraday rotation was averaged over the entire bilayer thickness, i.e. including the YIG contribution, and was comparable for both top-down and bottom-up films grown from the same target composition as shown in the inset in Fig. 4-8d.

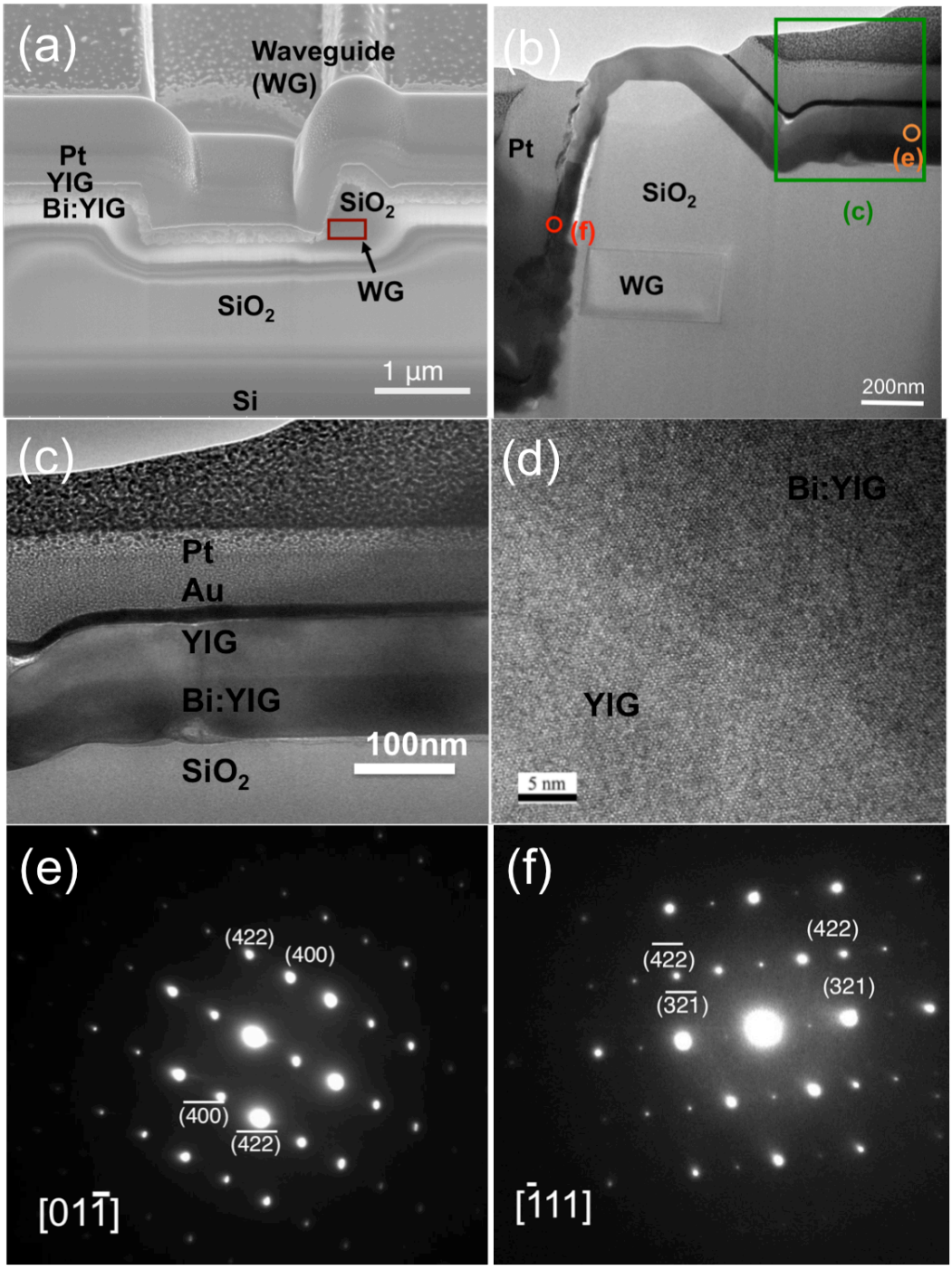

Figures 4-5: *(a) and (b) show the cross-sectional SEM and TEM images of top-down crystallized Bi:YIG film grown on a waveguide of an optical test device. In (a) the waveguide cross-section is highlighted in red. (c) Bright-field TEM cross-sectional images of bilayer film. (d) High resolution TEM images of the interface between the YIG and Bi:YIG layer. (e)*

Selected area diffraction (SAD) pattern taken along the $[0\bar{1}\bar{1}]$ *zone axis of the planar surface of the device with the aperture placed at the location indicated in orange in (b). (f) SAD pattern taken along* the $[\bar{1}11]$ *zone axis at the location indicated in red in (b).*

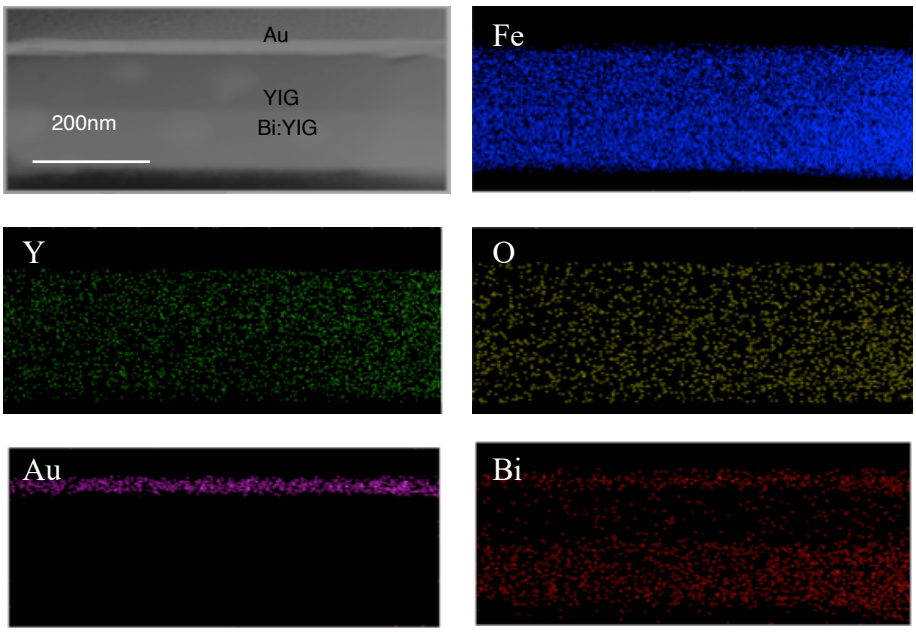

Figure 4-6: *Compositional analysis of YIG/Bi:YIG/Si film grown on planar surface of optical test device. Dark field TEM image and STEM-EDX element mappings of the top-down crystallized film showing the layer structure qualitatively.*

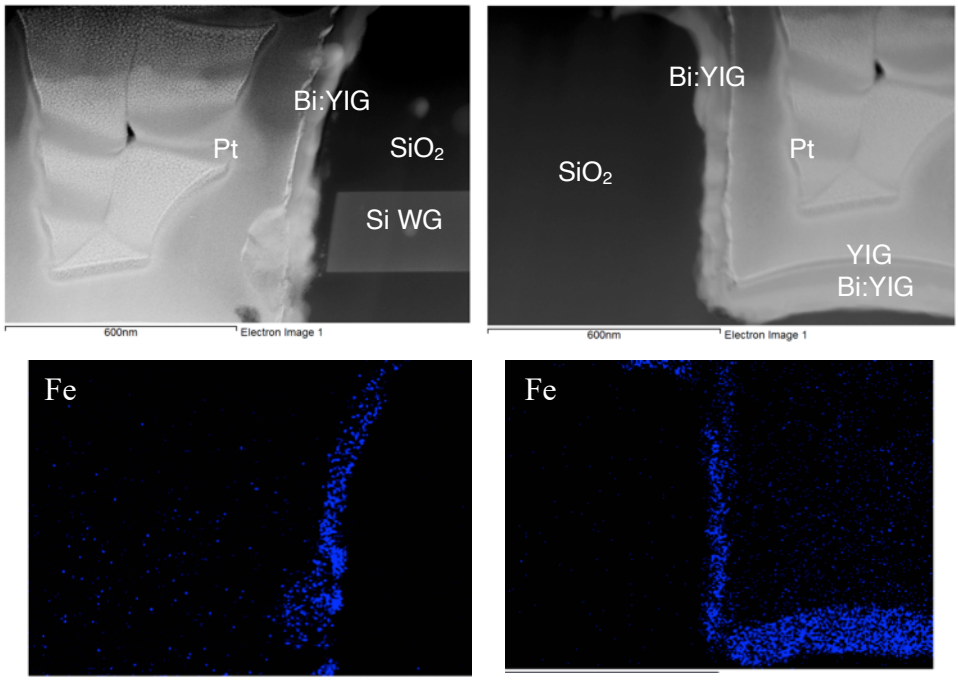

Figure 4-7: *Dark field TEM image and STEM-EDX element mapping of Fe of the YIG/Bi:YIG film grown side-wall of optical test device.*

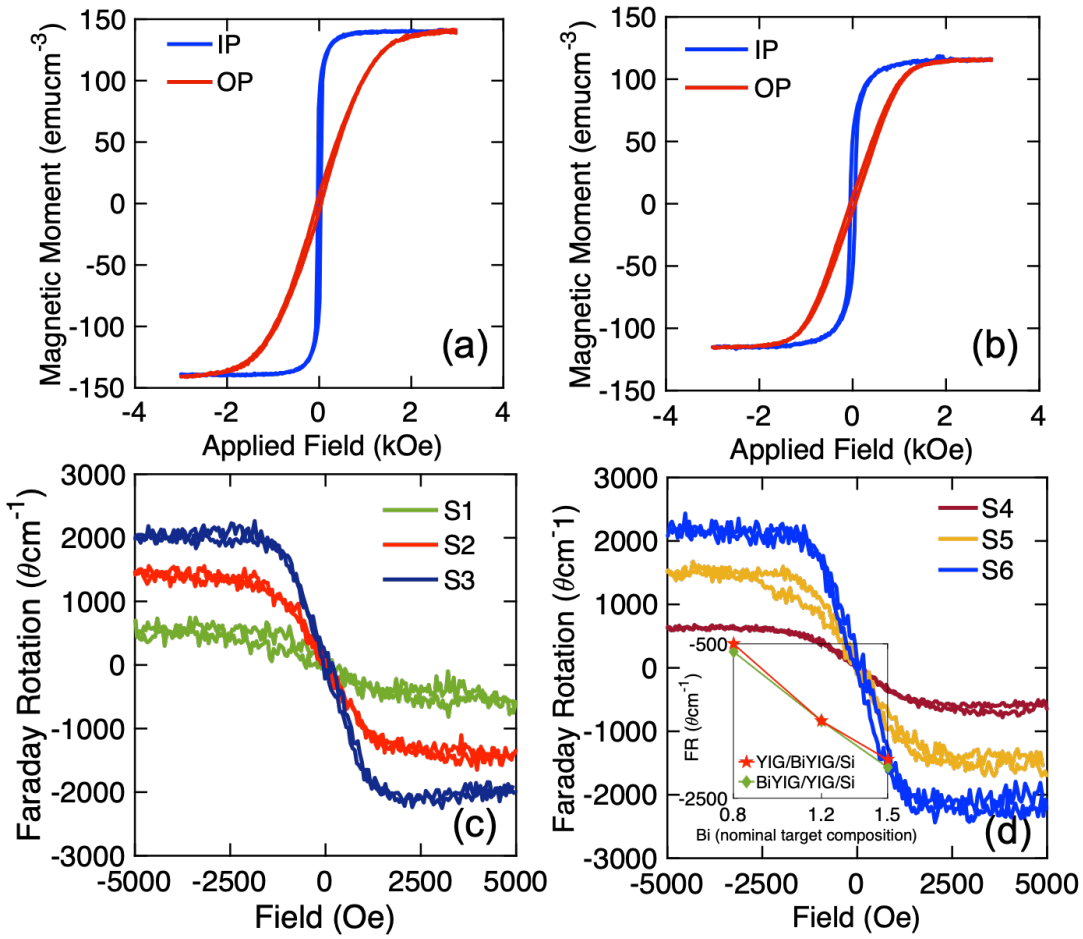

Figure 4-8: *In-plane (IP) and Out-of-plane (OP) hysteresis loops of films on Si after RTA (a) bottom-up crystallized film from $Bi_{1.2}Y_{1.8}Fe_5O_{12}$ target (b) top-down crystallized film from $Bi_{1.5}Y_{1.5}Fe_5O_{12}$ target. Out-of plane Faraday rotation hysteresis loops at 1550 nm wavelength of (c) top-down YIG/Bi:YIG and (d) bottom-up YIG/Bi:YIG films grown from target compositions of $Bi_{0.8}Y_{2.2}Fe_5O_{12}$, $Bi_{1.2}Y_{1.8}Fe_5O_{12}$ and $Bi_{1.5}Y_{1.5}Fe_5O_{12}$. Inset in (d) shows Faraday rotation versus nominal target composition for bottom-up and top-down films.*

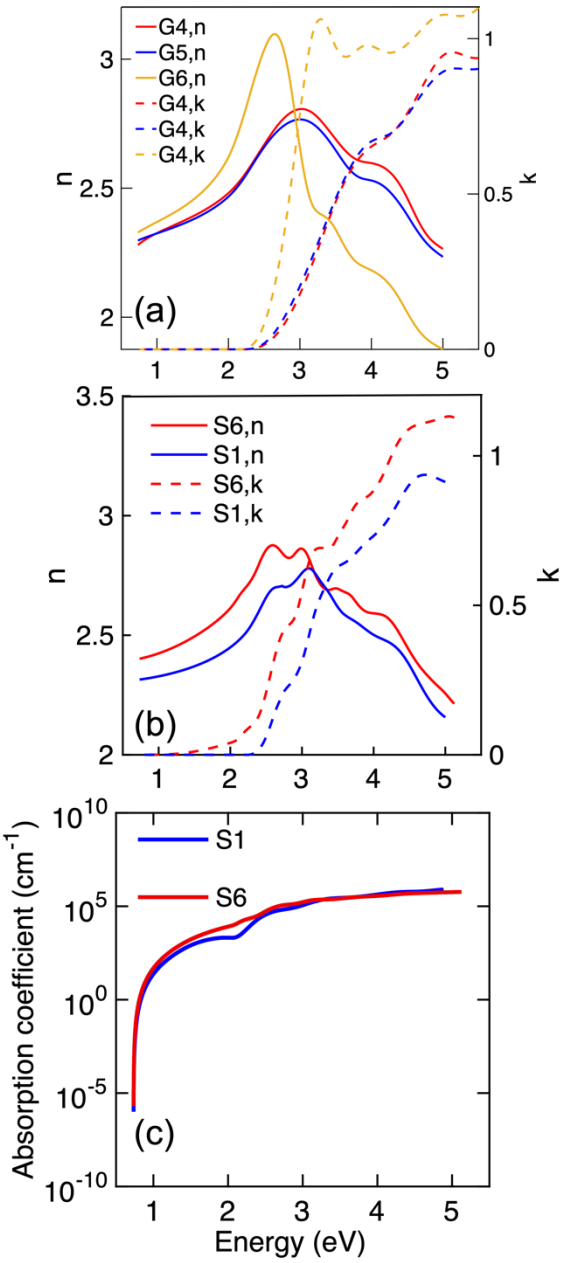

Figure 4-9: *Refractive index (n) and extinction coefficient (k) spectra of (a) Bi:YIG/GGG (b) Bi:YIG/YIG/Si and YIG/Bi:YIG/Si films characterized by spectroscopic ellipsometry. (c) Spectral dependence of absorption coefficient of Bi:YIG/YIG/Si and YIG/Bi:YIG/Si films.*

4.2.4 Optical Characterization

Experimental data measured by spectroscopic ellipsometer were fitted using a model structure of (a) thin Bi:YIG layer on GGG substrate, or (b) YIG/Bi:YIG layer on oxidized Si substrate. The optical parameters of GGG and YIG were obtained from separate measurements on bare GGG substrate and on a 90 nm thick YIG layer on GGG substrate. Kramers-Kronig consistency of the results was ensured by the dispersion model used.

Spectral dependences of the real, n, and imaginary, k, part of the complex refractive index are shown in Fig. 4-9a and 4-9b. The spectral behavior is typical for ferrimagnetic garnets.[13,34,43,45,46] Figure 6b clearly shows an increase in the absorption below the absorption edge with increasing Bi content, as was previously reported.[34] Using the results in Figure 6b we have calculated spectral dependence of the absorption coefficient of the samples grown on Si substrates. The resulting spectra are displayed in Fig. 4-9c.

The absorption coefficient falls dramatically in the IR region on moving away from the optical absorption edge. The films exhibit the highest values of FoM at 1550 nm reported for polycrystalline Bi:YIG films to date, as shown in Table 4-2. The lower bound of the FoM was 397 and 769° dB^{-1} at 1550 nm (E = 0.8 eV) for sample S1 and S6 from Table 1 respectively. These FoM values are more than an order of magnitude higher than previous reports for polycrystalline Ce:YIG films.[6,12]

Table 4-2. Comparison of MO Figure-of-merit values for polycrystalline garnets on non-garnet substrates, single crystalline garnets on garnet substrates and bulk garnets at λ = 1550 nm.

MO material and substrate	MO FoM [°dB^{-1}]	Growth Method	Optical Loss [dB.cm^{-1}]	Reference
$Y_{2.82}Ce_{0.18}Fe_5O_{12}$ (no substrate, bulk crystal)	1420	Traveling solvent floating zone	0.52	22
Single crystalline epitaxial Ce:YIG on GGG (111) substrate	943	PLD	6	13
Polycrystalline CeYIG on YIG on Si substrate	38	PLD	29	12
Ce:YIG on Si	21.8	PLD	58	6
YIG/$Bi_{0.8}$YIG/Si	397	PLD	1.26	This work
$Bi_{1.5}$YIG/YIG/Si	769	PLD	2.6	This work

4.3 Summary

In summary, polycrystalline YIG/Bi:YIG films were grown on Si in both bottom-up and top-down configuration using a single-step PLD method in which the YIG layer provides a template for Bi:YIG crystallization. Top-down YIG/Bi:YIG was demonstrated for the first time, crystallizing on both planar substrates and on sidewall features, and its Faraday rotation was as high as 2000^o cm^{-1} at 1500 nm. The top-down process allows the MO Bi:YIG layer to be placed in direct contact with an underlying waveguide which is expected to increase optical coupling into the Bi:YIG and improve the performance of integrated optical isolators. The FoM reported for both the top down and bottom-up crystallized films at 1550 nm are more than one order of magnitude higher than previous reported FoM values for polycrystalline MO garnets suggesting Bi:YIG as a material for non-reciprocal integrated photonics with enhanced performance.

References

[1] Thomson, D., Zilkie, A., Bowers, J.E., Komljenovic, T., Reed, G.T., Vivien, L., Marris-Morini, D., Cassan, E., Virot, L., Fédéli, J.M. and Hartmann, J.M., 2016. Roadmap on silicon photonics. *Journal of Optics*, *18*(7), p.073003.

[2] Almeida, V.R., Barrios, C.A., Panepucci, R.R. and Lipson, M., 2004. All-optical control of light on a silicon chip. *Nature*, *431*(7012), pp.1081-1084.

[3] Soref, R., 2005, March. Silicon photonics technology: past, present, and future. In Optoelectronic Integration on Silicon II (Vol. 5730, pp. 19-28). International Society for Optics and Photonics.

[4] Fan, L., Wang, J., Varghese, L.T., Shen, H., Niu, B., Xuan, Y., Weiner, A.M. and Qi, M., 2012. An all-silicon passive optical diode. *Science*, *335*(6067), pp.447-450.

[5] Huang, D., Pintus, P. and Bowers, J.E., 2018. Towards heterogeneous integration of optical isolators and circulators with lasers on silicon. *Optical Materials Express*, *8*(9), pp.2471-2483.

[6] Bi, L., Hu, J., Jiang, P., Kim, D.H., Dionne, G.F., Kimerling, L.C. and Ross, C.A., 2011. On-chip optical isolation in monolithically integrated non-reciprocal optical resonators. *Nature Photonics*, *5*(12), pp.758-762.

[7] Bi, L., Hu, J., Jiang, P., Kim, H.S., Kim, D.H., Onbasli, M.C., Dionne, G.F. and Ross, C.A., 2013. Magneto-optical thin films for on-chip monolithic integration of non-reciprocal photonic devices. *Materials*, *6*(11), pp.5094-5117.

[8] Du, Q., Fakhrul, T., Zhang, Y., Hu, J. and Ross, C.A., 2018. Monolithic magneto-optical oxide thin films for on-chip optical isolation. *MRS Bulletin*, *43*(6), pp.413-418.

[9] Yokoi, H., Mizumoto, T. and Shoji, Y., 2003. Optical nonreciprocal devices with a silicon guiding layer fabricated by wafer bonding. *Applied optics*, *42*(33), pp.6605-6612.

[10] Srinivasan, K. and Stadler, B.J., 2018. Magneto-optical materials and designs for integrated TE-and TM-mode planar waveguide isolators: a review. *Optical Materials Express*, *8*(11), pp.3307-3318.

[11] Sun, X.Y., Du, Q., Goto, T., Onbasli, M.C., Kim, D.H., Aimon, N.M., Hu, J. and Ross, C.A., 2015. Single-step deposition of cerium-substituted yttrium iron garnet for monolithic on-chip optical isolation. *Acs Photonics*, *2*(7), pp.856-863.

[12] Goto, T., Onbaşlı, M.C. and Ross, C.A., 2012. Magneto-optical properties of cerium substituted yttrium iron garnet films with reduced thermal budget for monolithic photonic integrated circuits. *Optics express*, *20*(27), pp.28507-28517.

[13] Onbasli, M.C., Beran, L., Zahradník, M., Kučera, M., Antoš, R., Mistrík, J., Dionne, G.F., Veis, M. and Ross, C.A., 2016. Optical and magneto-optical behavior of cerium yttrium iron garnet thin films at wavelengths of 200–1770 nm. *Scientific reports*, *6*(1), pp.1-10.

[14] Mizumoto, T., Shoji, Y. and Takei, R., 2012. Direct wafer bonding and its application to waveguide optical isolators. *Materials*, *5*(5), pp.985-1004.

[15] Stadler, B.J. and Mizumoto, T., 2013. Integrated magneto-optical materials and isolators: a review. *IEEE Photonics Journal*, *6*(1), pp.1-15.

[16] Du, Q., Wang, C., Zhang, Y., Zhang, Y., Fakhrul, T., Zhang, W., Gonçalves, C., Blanco, C., Richardson, K., Deng, L. and Ross, C.A., 2018. Monolithic on-chip magneto-optical isolator with 3 dB insertion loss and 40 dB isolation ratio. *ACS photonics*, *5*(12), pp.5010-5016.

[17] Kumar, N., Misra, D.S., Venkataramani, N., Prasad, S. and Krishnan, R., 2004. Magnetic properties of pulsed laser ablated YIG thin films on different substrates. *Journal of Magnetism and Magnetic Materials*, *272*, pp.E899-E900.

[18] P. Dulal, A. D. Block, T. E. Gage, H.A Haldren, S. Y. Sung, D. C. Hutchings, B. J. Stadler, *ACS Photonics* **2016**, *3*, 1818.

[19] Zhang, C., Dulal, P., Stadler, B.J. and Hutchings, D.C., 2017. Monolithically-integrated TE-mode 1D silicon-on-insulator isolators using seedlayer-free garnet. *Scientific reports*, *7*(1), pp.1-8.

[20] Shoji, Y. and Mizumoto, T., 2014. Magneto-optical non-reciprocal devices in silicon photonics. *Science and technology of advanced materials*.

[21] Pintus, P., Di Pasquale, F. and Bowers, J.E., 2011. Design of transverse electric ring isolators for ultra-low-loss Si 3 N 4 waveguides based on the finite element method. *Optics letters*, *36*(23), pp.4599-4601.

[22] S. Higuchi, S. Takekawa, S. K. Kitamura, *Jpn. J. Appl. Phys.* **1999**, *38*, 4122.

[23] Tepper, T. and Ross, C.A., 2003. Pulsed laser deposition and refractive index measurement of fully substituted bismuth iron garnet films. *Journal of Crystal Growth*, *255*(3-4), pp.324-331.

[24] Chern, M.Y. and Liaw, J.S., 1997. Study of BixY 3-xFe 5O12 Thin Films Grown by Pulsed Laser Deposition. *Japanese journal of applied physics*, *36*(3R), p.1049.

[25] Soumah, L., Beaulieu, N., Qassym, L., Carrétéro, C., Jacquet, E., Lebourgeois, R., Youssef, J.B., Bortolotti, P., Cros, V. and Anane, A., 2018. Ultra-low damping insulating magnetic thin films get perpendicular. *Nature communications*, *9*(1), pp.1-6.

[26] Hasanpour, A., Mozaffari, M., Amighian, J., Richert, H., Lorenz, A., Lindner, M., Görnert, P. and Heegn, H., 2007. Preparation and magneto-optical properties of BiY2Fe5O12 organic nanocomposite films. *Journal of magnetism and magnetic materials*, *317*(1-2), pp.41-45.

[27] Robertson, J.M., Wittekoek, S., Popma, T.J. and Bongers, P.F., 1973. Preparation and optical properties of single crystal thin films of bismuth substituted iron garnets for magneto-optic applications. *Applied physics*, *2*(5), pp.219-228.

[28] Leitenmeier, S., Körner, T., Griesbauer, J., Herbort, M., Heinrich, A. and Stritzker, B., 2008. Studies on the growth of epitaxial bismuth-substituted iron garnet on gadolinium gallium garnet single crystals by pulsed laser deposition. *Journal of Crystal Growth*, *310*(24), pp.5392-5401.

[29] Kahl, S. and Grishin, A.M., 2004. Enhanced Faraday rotation in all-garnet magneto-optical photonic crystal. *Applied Physics Letters*, *84*(9), pp.1438-1440.

[30] Siegel, G., Prestgard, M.C., Teng, S. and Tiwari, A., 2014. Robust longitudinal spin-Seebeck effect in Bi-YIG thin films. *Scientific reports*, *4*(1), pp.1-6.

[31] Lux, R., Heinrich, A., Leitenmeier, S., Körner, T., Herbort, M. and Stritzker, B., 2006. Pulsed-laser deposition and growth studies of Bi 3 Fe 5 O 12 thin films. *Journal of applied physics*, *100*(11), p.113511.

[32] Adachi, N., Denysenkov, V.P., Khartsev, S.I., Grishin, A.M. and Okuda, T., 2000. Epitaxial Bi 3 Fe 5 O 12 (001) films grown by pulsed laser deposition and reactive ion beam sputtering techniques. *Journal of Applied Physics*, *88*(5), pp.2734-2739.

[33] Veis, M., Lišková, E., Antoš, R., Višňovský, Š., Kumar, N., Misra, D.S., Venkataramani, N., Prasad, S. and Krishnan, R., 2011. Polar and longitudinal magneto-optical spectroscopy of bismuth substituted yttrium iron garnet films grown by pulsed laser deposition. *Thin Solid Films*, *519*(22), pp.8041-8046.

[34] Wittekoek, S., Popma, T.J., Robertson, J.M. and Bongers, P.F., 1975. Magneto-optic spectra and the dielectric tensor elements of bismuth-substituted iron garnets at photon energies between 2.2-5.2 eV. *Physical review B*, *12*(7), p.2777.

[35] Chern, M.Y., Lo, F.Y., Liu, D.R., Yang, K. and Liaw, J.S., 1999. Red shift of Faraday rotation in thin films of completely bismuth-substituted iron garnet Bi3Fe5O12. *Japanese Journal of Applied Physics*, *38*(12R), p.6687.

[36] Inoue, M., Fujikawa, R., Baryshev, A., Khanikaev, A., Lim, P.B., Uchida, H., Aktsipetrov, O., Fedyanin, A., Murzina, T. and Granovsky, A., 2006. Magnetophotonic crystals. *Journal of Physics D: Applied Physics*, *39*(8), p.R151.

[37] Körner, T., Heinrich, A., Weckerle, M., Roocks, P. and Stritzker, B., 2008. Integration of magneto-optical active bismuth iron garnet on nongarnet substrates. *Journal of Applied Physics*, *103*(7), p.07B337.

[38] Block, A.D., Dulal, P., Stadler, B.J. and Seaton, N.C., 2013. Growth parameters of fully crystallized YIG, Bi: YIG, and Ce: YIG films with high faraday rotations. *IEEE Photonics Journal*, *6*(1), pp.1-8.

[39] Geller, S., Williams, H.J., Espinosa, G.P., Sherwood, R.C. and Gilleo, M.A., 1963. Reduction of the preparation temperature of polycrystalline garnets by bismuth substitution. *Applied Physics Letters*, *3*(2), pp.21-22.

[40] Matsumoto, K., Yamaguchi, K., Fujii, T. and Ueno, A., 1991. Preparation of bismuth-substituted yttrium iron garnet powders by the citrate gel process. *Journal of applied physics*, *69*(8), pp.5918-5920.

[41] Bi, L., Taussig, A.R., Kim, H.S., Wang, L., Dionne, G.F., Bono, D., Persson, K., Ceder, G. and Ross, C.A., 2008. Structural, magnetic, and optical properties of BiFeO 3 and Bi 2 FeMnO 6 epitaxial thin films: an experimental and first-principles study. *Physical Review B*, *78*(10), p.104106.

[42] Béa, H., Bibes, M., Fusil, S., Bouzehouane, K., Jacquet, E., Rode, K., Bencok, P. and Barthélémy, A., 2006. Investigation on the origin of the magnetic moment of BiFeO 3 thin films by advanced x-ray characterizations. *Physical Review B*, *74*(2), p.020101.

[43] Scott, G.B. and Lacklison, D., 1976. Magnetooptic properties and applications of bismuth substituted iron garnets. *IEEE Transactions on Magnetics*, *12*(4), pp.292-311.

[44] H. L. Gall, M. Guillot, A. Marchand, Y. Nomi, M. Artinian, J. M. Desvignes, *J. Magn. Soc. Jpn.* **1987**, *11*, S1_235.

[45] Hansen, P. and Krumme, J.P., 1984. Magnetic and magneto-optical properties of garnet films. *Thin solid films*, *114*(1-2), pp.69-107.

[46] Dionne, G.F. and Allen, G.A., 1993. Spectral origins of giant Faraday rotation and ellipticity in Bi-substituted magnetic garnets. *Journal of applied physics*, *73*(10), pp.6127-6129.

[47] Pintus, P., Di Pasquale, F. and Bowers, J.E., 2013. Integrated TE and TM optical circulators on ultra-low-loss silicon nitride platform. *Optics express*, *21*(4), pp.5041-5052.

5. Rare-earth iron garnet thin films for integrated photonics

5.0 Introduction and Motivation

In the last chapter we reported our work on BiYIG/Si , for on-chip optical isolation, that had a record high MO materials figure-of-merit. While BiYIG studied in this work and also CeYIG as found in literature both have excellent MO figure of merit [1-18], crystallization of these garnets without secondary phases can only be accomplished by depositing a YIG seedlayer placed either above or below the active MO layer. When a seed layer is included, a top seed layer is preferable as it maximizes coupling of the MO garnet with an optical mode propagating through an underlying waveguide [12,13]. In the case of BiYIG, our study shows the bottom seed layer is easier to crystallize and has almost twice the figure of merit than a top seed layer crystallized BiYIG film. So, the challenge of crystallizing a high figure of merit MO material in direct contact with Si remains.

Although YIG crystallizes readily on non-garnet substrates, it has a low Faraday rotation (~ +100 °/cm at 1550 nm)[10] and FoM. Like YIG, rare earth garnets such as terbium iron garnet (TbIG) or dysprosium iron garnet [19,20] can crystallize directly on non-garnet substrates to form polycrystalline films. TbIG is a thermodynamically stable phase [21,22] which promotes garnet-phase crystallization without a seed layer. TbIG has a Faraday rotation in the 1100 – 1550 nm wavelength range of ~ +270 to +1000 °/cm. [23-25] Bi-substituted TbIG has been grown by liquid-phase epitaxy and flux methods[23-27] or sol-gel methods [28], and more recently thin films of Ce- and Bi-substituted TbIG (CeTbIG, BiTbIG) were grown on Si by sputtering.[29-34] Sputtered BiTbIG with Bi substitution of 14% of the Tb sites has a Faraday rotation of ~ -500 °/cm at 1550 nm,[29] the same sign as that of CeYIG, which at 1550 nm wavelength had a Faraday rotation of at least -3700 °/cm.[30] CeTbIG films with Ce substituting up to 25% of the Tb sites showed a Faraday rotation above -3200 ± 200 °/cm,[31,32] but a 44 nm thick magnetic dead layer formed between the waveguide and the CeTbIG, hindering the interaction of the

The work in this chapter was published in Advanced Optical Materials, 2021, p.2100512.

evanescent light with the MO garnet cladding.[32] However, the optical absorption and FoM of these Bi- and Ce-substituted TbIG materials has not yet been reported.

In this chapter we report the growth, magnetic and optical characteristics of polycrystalline thin films of TbIG, CeTbIG and BiTbIG synthesized using pulsed laser deposition (PLD) on Si substrates. The effect of the growth conditions on the stoichiometry of TbIG, CeTbIG and BiTbIG films is discussed. We show that by composition control of the Ce- and Bi-substituted TbIG, high Faraday rotation is achievable, up to 6200 °/cm at 1550 nm wavelength. The optical absorption of the TbIG garnet films can be reduced by addition of Bi^{3+} and Ce^{3+} and the possible mechanisms of optical absorption in these films are discussed. The figure of merit reached 720 °/dB, the highest reported for polycrystalline garnet films with the added benefit of improved device performance due to the absence of a seed layer. The temperature dependence of the magneto-optical and magnetic properties of these thin films are also characterized.

5.1 TbIG/Si, CeTbIG/Si and BiTbIG/Si thin films

5.1.1 Structural, Compositional and Surface Characterization

TbIG, CeTbIG and BiTbIG films were grown on Si substrates with native oxides by PLD from targets of composition $Tb_3Fe_5O_{12}$, $Ce_1Tb_2Fe_5O_{12}$ and $Bi_{0.3}Tb_{2.7}Fe_5O_{12}$ using a 248 nm wavelength 45 KrF excimer laser (Coherent, COMPex Pro 205). The targets were prepared by mixed oxide sintering [12] of 99.999% pure Tb_2O_3, CeO_2, Bi_2O_3, and Fe_2O_3 powders. The films were grown at a repetition rate of 10 Hz and laser fluence of 1.5 and 2.5 J cm^{-2}. The substrate heater setpoint temperature was 900°C which corresponds to a substrate temperature of approximately 750 °C, and an oxygen pressure of 10 mTorr. Afterwards the films were rapid thermally annealed (RTA) at 900 °C for 3 minutes in oxygen. Different compositions for the CeTbIG and BiTbIG films were achieved by codeposition with the TbIG target, by alternately ablating the targets using 25 laser shots on TbIG target and between 4-15 laser shots on the CeTbIG and BiTbIG targets. Iron garnets such as $Tb_3Fe_5O_{12}$ form cubic crystals with lattice parameter of ~1.2 nm and 8 formula units per unit cell, illustrated in Fig. 5-1a. Tb, Bi and Ce are expected to occupy 3 dodecahedral sites per formula unit whereas the Fe occupies 2 octahedral and 3 tetrahedral sites. We define a composition parameter R as the ratio of $\frac{Tb+Ce+Bi}{Fe}$

which characterizes how close the film is to the ideal cation stoichiometric ratio of R=0.6. Table 5-1 shows the cation ratios of films made in this study determined by wavelength dispersive x-ray spectroscopy (WDS).

Fig. 5-1b-d shows the x-ray diffraction (XRD) patterns and R ratios for several samples of TbIG, CeTbIG and BiTbIG after rapid thermal annealing (RTA) at 900 °C for 3 min. The nominally TbIG samples have an R ratio of 0.70, 0.57 and 0.54 (Fig. 5-1b), yet they each crystallize well on Si, showing the characteristic garnet (400), (420) and (422) powder peaks near 2θ = 30˚ with no detectable peaks from secondary phases. An iron deficiency similar to that of the TbIG with R=0.70 has also been reported for single crystal TbIG films with the excess Tb incorporated into the octahedral sites usually occupied by Fe [35]. The iron deficiency of the films in this study was reduced by using a lower laser fluence which is believed to result in less scattering of Fe atoms in the PLD plume compared to the rare earth.

In the case of CeTbIG, while all the compositions shown in Fig.5-1c form garnet phases, only the $Ce_{0.36}$TbIG film, which has a R ratio that is closest to 0.6, crystallizes with all three of the garnet peaks near 2θ = 30˚. Increasing Ce content led to the formation of broad garnet peaks or secondary phase formation. For BiTbIG, most of the films have very low bismuth content compared to the target. This is due to the volatility of bismuth, which is commonly depleted during high temperature deposition or annealing.[12] By using a lower substrate temperature of 700 ˚C and a higher oxygen pressure of 100 mTorr, the Bi content was greatly enriched, forming $Bi_{0.79}$TbIG with a R ratio of 0.66, but this composition did not crystallize as a single phase garnet according to the XRD data (Fig.5-1d).

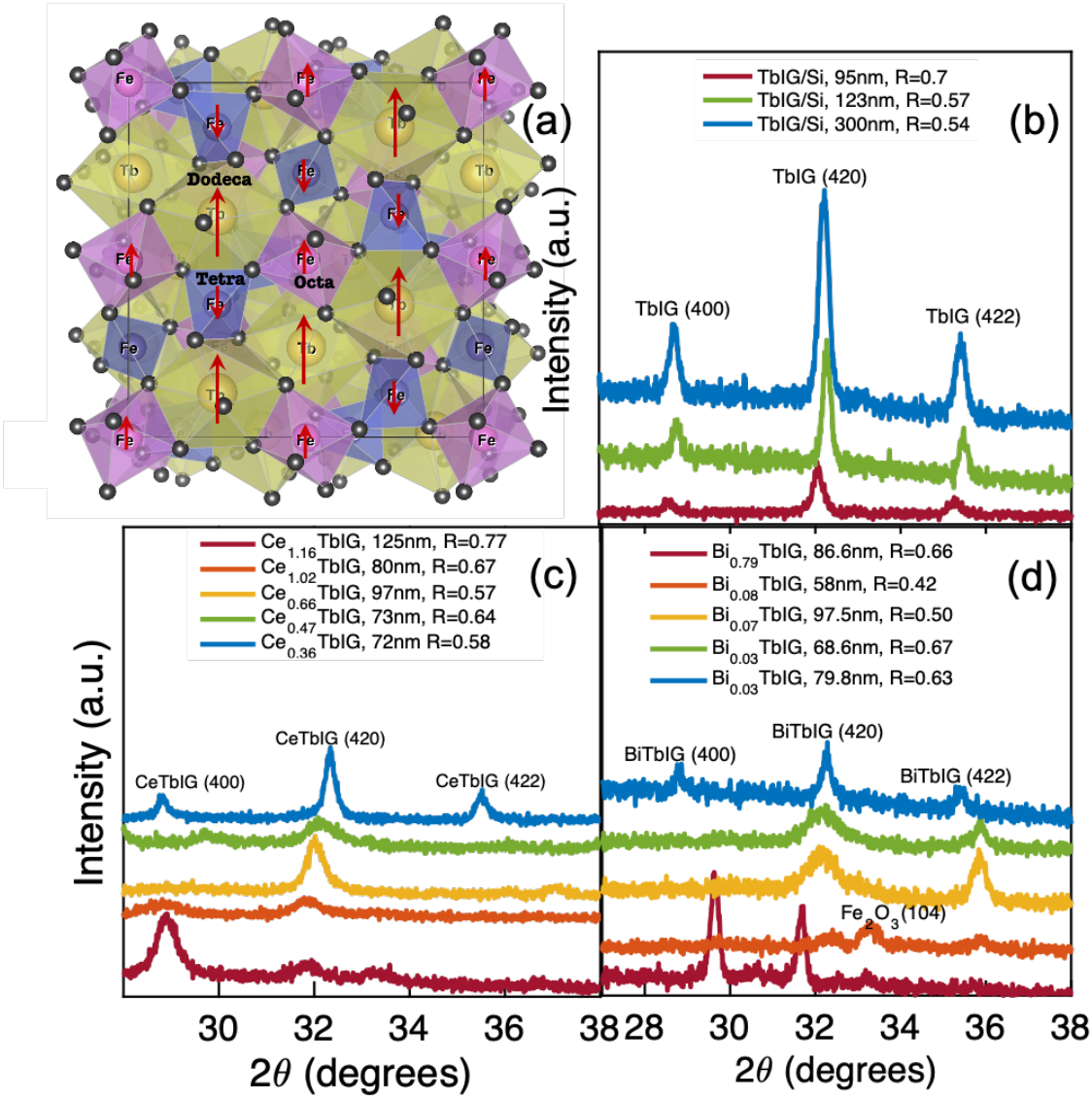

Figure 5-1: *(a) Cubic unit cell of TbIG showing octahedral (pink), tetrahedral (purple) and dodecahedral (yellow) sites. The cation sites are surrounded by O^{2-} (indicated by black spheres) at the vertices of the polyhedrons. Magnetization directions of the Tb^{3+} and Fe^{3+} cations are shown using red arrows. (b-d) XRD $\omega-2\theta$ scans for polycrystalline (a) TbIG , (b) CeTbIG and (c) BiTbIG films on silicon after RTA at 900°C for 3min.*

***Table 5-1**. Cation ratios for all films of the TbIG, CeTbIG and BiTbIG shown in Figure 5-1. The data are presented such that the sum of the cation concentrations is 8.*

Sample	Name	Ce or Bi	Tb	Fe	R	Thickness, nm
1	TbIG	0.00	3.3	4.7	0.702	95
2	TbIG	0.00	2.9	5.1	0.569	123
3	TbIG	0.00	2.8	5.2	0.538	300
2	$Ce_{0.36}Tb_{2.59}Fe_{5.05}O_{12}$	0.36	2.59	5.05	0.584	72
3	$Ce_{0.47}Tb_{2.65}Fe_{4.88}O_{12}$	0.47	2.65	4.88	0.639	73
4	$Ce_{0.66}Tb_{2.23}Fe_{5.11}O_{12}$	0.66	2.23	5.11	0.564	97
5	$Ce_{1.02}Tb_{2.18}Fe_{4.80}O_{12}$	1.02	2.18	4.8	0.667	80
6	$Ce_{0.9}Tb_{2.32}Fe_{4.52}O_{12}$	1.16	2.32	4.52	0.770	125
7	$Bi_{0.03}Tb_{3.06}Fe_{4.9}O_{12}$	0.03	3.06	4.90	0.630	79.8
8	$Bi_{0.79}Tb_{2.4}Fe_{4.81}O_{12}$	0.79	2.40	4.81	0.657	86.6
9	$Bi_{0.03}Tb_{3.19}Fe_{4.78}O_{12}$	0.03	3.19	4.78	0.673	68.6
10	$Bi_{0.07}Tb_{2.6}Fe_{5.33}O_{12}$	0.07	2.60	5.33	0.500	97.5
11	$Bi_{0.06}Tb_{1.7}Fe_{4.2}O_{12}$	0.08	2.28	5.64	0.418	58

Based on the structural and compositional analysis we selected three exemplary films for further magnetic and magneto-optical characterization. The films, of composition TbIG (123 nm thick, measured composition Tb:Fe = 2.9:5.1, R=0.57), $Ce_{0.36}$TbIG (72 nm, Ce:Tb:Fe = 0.36:2.59:5.05, R = 0.58) and $Bi_{0.03}$TbIG (79.8 nm, Bi:Tb:Fe = 0.03:3.06:4.9, R = 0.63), consist of polycrystalline single-phase garnet. AFM images of these three films in Fig. 5-2(a-c) show that the TbIG has a grain size of the order of 100 – 150 nm, the CeTbIG exhibits a range of grain sizes from 20 - 100 nm, and the $Bi_{0.03}$TbIG had a grain size of 10-30 nm with the grains forming larger clusters. Even though the final Bi content in the film is small, we expect that the film contained a much greater fraction of Bi prior to RTA which was lost on annealing, and this affected the microstructural development compared to that of TbIG. The AFM bimodal technique, called DualAC, was also employed for high quality images of the lateral microstructure of the thin films as shown in Fig. 5-3. The photothermal excitation technique,

called blueDrive, was utilized to tune both the primary and second order resonance peaks. In particular, the signal from the minute amplitude of oscillation of the second mode for an Olympus AC160TSA-R3 cantilever is used to present the AFM images in Fig. 5-3.

5.1.2 Magnetic Characterization

Magnetic hysteresis of the films was measured with the magnetic field applied both in-plane and out-of-plane (perpendicular to the films) using a vibrating sample magnetometer (VSM), and temperature-dependent in-plane magnetic hysteresis measurements were carried out using a SQUID magnetometer. The VSM hysteresis loops at room temperature are given in Fig. 5-2d-f. The TbIG (R=0.57), $Ce_{0.36}$TbIG and $Bi_{0.03}$TbIG films have room temperature saturation magnetization (M_s) of 43, 26 and 38 kA m^{-1} respectively. The total anisotropy of the films includes the sum of magnetocrystalline, magnetoelastic (K_{me}) and shape (K_{sh}) anisotropy contributions. The magnetocrystalline anisotropy can be neglected due to the polycrystallinity of the films, and the net uniaxial anisotropy becomes

$$K_u = E_{OP} - E_{IP} = K_{mc} + K_{me} + K_{sh} + K_{growth} = -\frac{K_1}{2} + \frac{9}{4}\lambda_{111}c_{44}\left(\frac{\pi}{2} - \beta\right) - \frac{\mu_o}{2}M_s^2 \quad (1)$$

where λ is the magnetostriction coefficient for the polycrystal, E is the Young's modulus, ν is the Poisson's ratio and ε_x and ε_z are the in-plane and out-of-plane strain. Iron garnet is close to being elastically isotropic, with an elastic anisotropy factor $2c_{44}/(c_{11} + c_{12}) = 0.947$ calculated for YIG [36] where c_{11}, c_{12}, and c_{44} are the three independent cubic elastic constants. The elastic properties of polycrystalline garnet are then given by $E = \frac{(c_{11}+2c_{12})(c_{11}-c_{12})}{(c_{11}+c_{12})}$ and $\upsilon = \frac{c_{12}}{c_{11}+c_{12}}$. The room temperature magnetostriction coefficients of single crystal TbIG are $\lambda_{100} = -3.3 \times 10^{-6}$ and $\lambda_{111} = +12 \times 10^{-6}$ [37]. The approximation for the magnetostriction λ of a polycrystal proposed by Akulov[38] is

$$\lambda = \frac{2}{5}\lambda_{100} + \frac{3}{5}\lambda_{111} \quad (2)$$

which yields $\lambda = +5.88 \times 10^{-6}$ for TbIG. An approximation of Callen and Goldberg[39,40] which assumes a non-uniform mechanical stress within the polycrystalline aggregate gives a similar result of $\lambda = +5.73 \times 10^{-6}$ based on the elastic constants of TbIG.[38]

The strain state in the garnet films on Si is dominated by thermal expansion mismatch. The in-plane strain is $\varepsilon_x = \varepsilon_y = \varepsilon_o = \Delta\alpha\Delta T$ where $\Delta\alpha = \alpha_{film} - \alpha_{substrate}$ is the mismatch between the thermal expansion coefficient (α) of the film and substrate and ΔT is the temperature change. We assume for TbIG that α has little variation within the temperature range, which is a reasonable approximation for iron garnets.[41] The TbIG film on Si will experience an in-plane tensile strain after cooling down from 900 °C. For an isotropic film under biaxial stress, the out-of-plane strain is $\varepsilon_z = -\frac{2\nu}{1-\nu}\varepsilon_o$.

Both magnetoelastic and shape anisotropy favor an in-plane easy axis, though the magnetoelastic contribution for TbIG (R=0.57) is more than 2 times greater than the shape anisotropy. The total anisotropy for the films, K_u, is calculated from the predicted thermal mismatch, magnetostriction and magnetization and is shown in Table 5-2. The values of K_u have the same sign and indicate an in-plane easy magnetization direction for all the films. The calculated anisotropy for TbIG (R=0.57) agrees well with the anisotropy determined experimentally from the difference in area between the in-plane and out-of-plane anhysteretic loops (i.e. the measured loops with hysteresis subtracted) [40], suggesting that thermal mismatch provides a reasonable estimation of the strain state and the bulk magnetostriction values are appropriate.

In contrast, the measured anisotropy of the $Bi_{0.03}$TbIG is 5 times higher than that of the TbIG, exceeding the value predicted from the magnetostriction and thermal mismatch strain. This suggests that the strain or the magnetostriction are higher than those of TbIG, or there may be another source of anisotropy. The magnetostriction is likely similar to that of TbIG due to the small Bi content, but Bi loss on annealing and the subsequent volume reduction could account for an increase in the in-plane tensile strain, and the Bi may also affect strain relaxation mechanisms.[42]

The magnetostriction of Ce-substituted garnets is not well characterized, but magnetostriction coefficients of $\lambda_{100} = +120 \times 10^{-6}$ and $\lambda_{111} = +50 \times 10^{-6}$ [43-45] have been extrapolated for the theoretical garnet $Ce_3Fe_5O_{12}$ based on data from YIG with small substitutions of Ce. Ce provides a positive contribution to the magnetostriction of YIG, and extrapolating from data reported by Wijn[43] we estimate $\lambda = +35\ 10^{-6}$ for polycrystalline $Ce_{0.36}$TbIG. This is 6 times larger than the magnetostriction of polycrystalline TbIG, and could account for the larger anisotropy of $Ce_{0.36}$TbIG compared to TbIG even if the actual value of magnetostriction is not as large as the extrapolated value.[13,45]

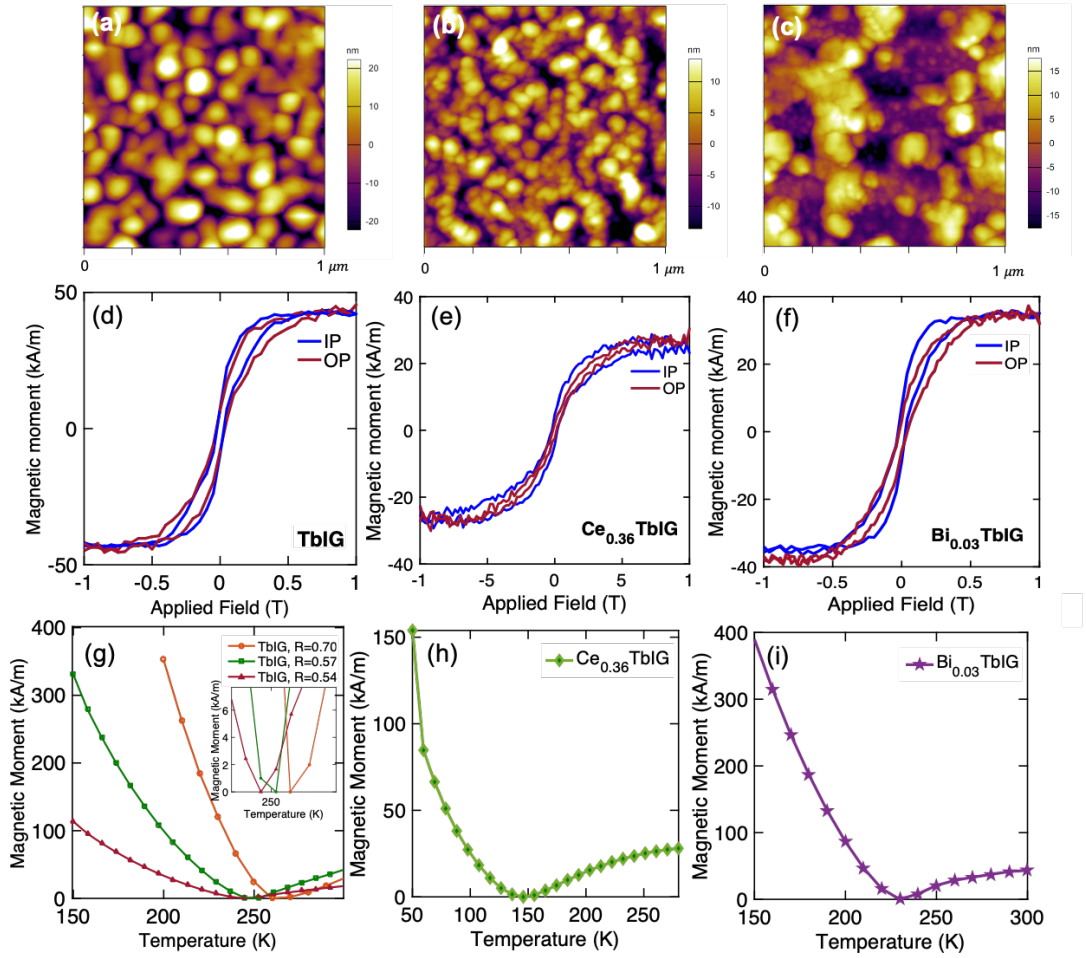

Figure 5-2: *AFM height images post-RTA for (a) TbIG/Si (R=0.57), (b) $Ce_{0.36}$TbIG/Si (c) $Bi_{0.03}$TbIG/Si. In-plane (IP) and out-of-plane (OP) VSM room temperature hysteresis loops of (d) TbIG (R=0.57), (e) $Ce_{0.36}$TbIG and (f) $Bi_{0.03}$TbIG films on Si after RTA. Temperature*

dependent magnetization measured in a SQUID magnetometer for (g) TbIG (R=0.54, 0.57 & 0.7) , (h) $Ce_{0.36}$TbIG and (i) $Bi_{0.03}$TbIG.

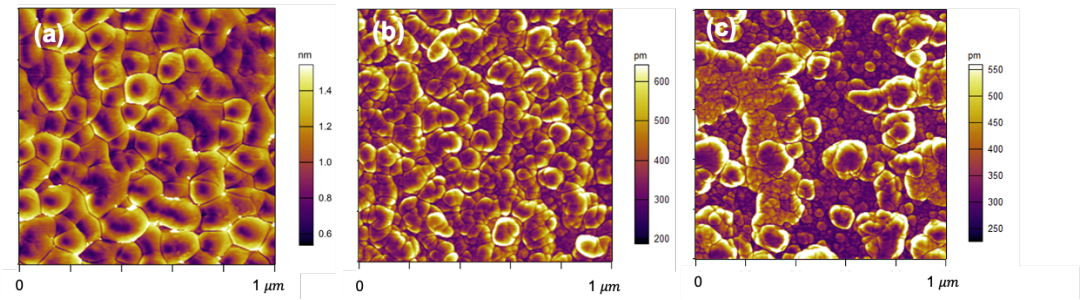

Figure 5-3: *Bimodal (height and phase superposed) AFM images post-RTA for (a) TbIG/Si (R=0.57) , (b) $Ce_{0.36}$TbIG/Si (c) $Bi_{0.03}$TbIG/Si.*

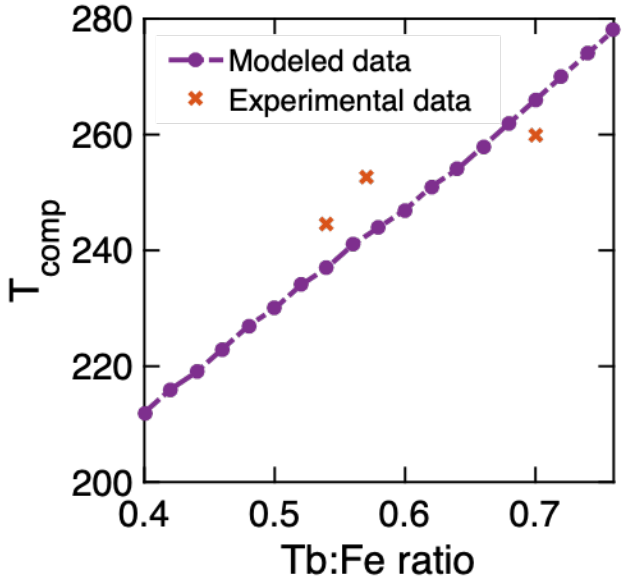

Figure 5-4: *Modeled compensation temperature (T_{comp}) versus Tb:Fe ratio.*

Table 5-2. Magnetic, optical and magnetooptical properties of garnet films on Si

Sample	Calculated λ from Refs. 38, 42 (10^{-6})	Calculated K_{me} kJ/m³	Calculated K_{sh} kJ/m³	Calculated $K_u = K_{me} + K_{sh}$ kJ/m³	Measured Anisotropy from anhysteretic loops kJ/m³	Model T_{comp} (K)	Measured T_{comp} (K)	Faraday Rotation 1550 nm °cm⁻¹	Optical Loss 1550 nm dB.cm⁻¹	MO FoM 1550 nm °dB⁻¹
TbIG (95 nm) /Si, R=0.70	5.73	-2.8	-0.57	-3.37	-2.99	266	259.9 ± 2.5	3500 ± 300	19.9	175
TbIG (123 nm) /Si, R=0.57			-1.16	-3.96	-3.42	243	252.6 ± 2.5	5400 ± 600	17.4	310
TbIG (300 nm) /Si, R=0.54			-0.20	-3.00	-0.97	237	244.6 ± 2.4	1800 ± 240	-	-
$Bi_{0.03}$TbIG (80 nm) /Si	5.73	-2.8	-0.91	-3.71	-15.01	236	229.9 ±2.2	6200 ± 300	8.6	720
$Ce_{0.36}$TbIG (72 nm) /Si	35.4	-17.5	-0.42	-17.92	-9.09	193	145.8±1.4	4500 ± 100	8.3	540

We now describe the trends in magnetic compensation temperature with composition. In iron garnets the strongest superexchange interactions occur between the octahedral Fe^{3+} and tetrahedral Fe^{3+} sites leading to ferrimagnetic ordering. The moment of the rare earth (here Tb^{3+}) in the dodecahedral sites is coupled antiparallel to the tetrahedral Fe^{3+} as shown in Fig. 5-1a. The dodecahedral Tb moments are canted at low temperatures around the [111] directions.[46,47] The different temperature-dependences of the Tb^{3+} and Fe^{3+} moments and the canting lead to a compensation temperature T_{comp} where the net Tb moment plus the octahedral

Fe moment balances the tetrahedral Fe moment and the total moment is zero, i.e. at T_{comp} three dodecahedral Tb contribute the same net magnetic moment as one tetrahedral Fe^{3+}.

The polycrystalline TbIG (R=0.57) has a T_{comp} of 252.6 K [$\pm$2.5K] which is near the bulk T_{comp} of 248.6 K. [35] The iron deficient TbIG (R=0.70) has a T_{comp} of 260 K [$\pm$2.6K], while the iron rich TbIG (R=0.54) has T_{comp} of 244.6 K [$\pm$2.4K] as shown in Fig. 5-2g, which also demonstrates that an increase in Tb:Fe ratio raises the magnetization below T_{comp}. The increase in compensation temperature with Tb enrichment is like observations of Rosenberg et al. [35] and can be attributed to excess Tb occupying octahedral sites. Tb can also be tetravalent, and in Tb-rich TbIG the Tb^{4+} is more likely to occupy the smaller octahedral sites. When the Tb is on the octahedral sites it is expected to exhibit stronger exchange coupling to the Fe^{3+} and less canting than dodecahedral Tb. This raises the magnetic moment of the octahedral sublattice relative to that of the tetrahedral sublattice which increases T_{comp} and the low temperature net magnetization.

To compare with experimental data, a modified version of Dionne's molecular field coefficient model for garnets was employed. [48,49] The model was modified to account for off-stoichiometry in the films by assuming that excess rare-earth occupies the octahedral sites, whereas excess iron occupies the dodecahedral sites. The molecular field coefficients are assumed to be independent of the site occupancy. Comparison with experimentally measured compensation temperatures for the TbIG shows close agreement, with the trend of higher R values leading to higher compensation temperatures as shown in Fig. 5-4.

Replacing Tb^{3+} ($4f^8$) with Bi^{3+} ($5d^{10}6s^2$) or Ce^{3+} ($4f^1$) is expected to reduce the magnetization of the dodecahedral sublattice and lower T_{comp}, with Bi having a larger effect than Ce. To estimate T_{comp} for $Ce_{0.36}$TbIG and $Bi_{0.03}$TbIG we assume that the contribution to the magnetic moment from the octahedral and tetrahedral Fe^{3+} is the same as that of YIG. [46,50-52] The Tb^{3+} sublattice magnetization can then be obtained by subtracting the magnetization of YIG [46] from that of TbIG,

$$[M_{Tb^{3+}}]_T = [M_{TbIG}]_T - [M_{YIG}]_T \ .$$

The resulting temperature-dependent sublattice magnetization of Tb^{3+}, $[M_{Tb^{3+}}]_T$, is then scaled to account for Bi^{3+} or Ce^{3+} substitution and added back to the temperature-dependent magnetization of YIG, $[M_{YIG}]_T$, to obtain the thermomagnetic curves for $Bi_{0.03}$TbIG and $Ce_{0.36}$TbIG. The predicted values of T_{comp} are shown in Table 5-2. The measured T_{comp} for $Bi_{0.03}$TbIG is lower than that of bulk TbIG by 19 K (Fig. 5-2i), whereas the model predicted a decrease by 13 K. As a comparison, sol-gel $Bi_xTb_{3-x}IG$ showed a decrease in T_{comp} by 80 K for x=0.5. [28] In the case of $Ce_{0.36}$TbIG, the measured reduction in T_{comp} by 103 K (Fig. 5-2h) is much larger than predicted by the model (56 K). A significant Ce^{4+} content appears unlikely, since it would be associated with Fe^{2+} and a higher optical absorption,[53] and there was no detectable CeO_2 found from XRD. The results show that both the Bi and Ce lower T_{comp} further than would be expected from a model based on simple dilution of the rare earth moment, which may indicate that the Ce or Bi affects the cation site occupancy in the films or the canting which is present at and below T_{comp}.[47]

5.1.3 Magneto-optical characterization

The temperature and spectral dependences of magneto-optical effects were obtained using a high precision magneto-optical spectrometer with a rotating analyzer, which enabled Faraday effect measurements to an accuracy of ~1 mdeg. Saturation Faraday rotation at 1550 nm at room temperature for the TbIG (R = 0.57), $Ce_{0.36}$TbIG and $Bi_{0.03}$TbIG films was 5400 ± 600 °/cm, 4500± 100 °/cm and 6200± 300°/cm respectively as shown in Fig. 5-5a. The greater Faraday rotation of TbIG in comparison to YIG at energies around 1eV is due to strong optical transitions at higher energies induced by Tb^{3+}.[54] Tb^{3+} is reported to increase the splitting of oscillator strength for left and right circularly polarized light above 4e V in iron garnets due to exchange interactions between Tb^{3+} and tetrahedral Fe^{3+}[54]. The Faraday rotation of TbIG is thus proportional to the magnetic moment of the ions involved in this charge transfer process.[52,54] Bi^{3+} and Ce^{3+} both have a negative contribution to the Faraday rotation of YIG [55-57] and in $Ce_{0.36}$TbIG the positive Faraday rotation is lower in comparison to TbIG as

expected. However, in $Bi_{0.03}$TbIG the Bi content is small and the Faraday rotation of TbIG and BiTbIG agree within the error range.

The polar Kerr rotation spectrum of the TbIG film shown in Fig. 5-5b resembles prior results[54] for single crystal TbIG. In TbIG, optical transitions located between 3-4 eV originate from Fe^{3+} crystal-field transitions.[54] The amplitude of the Kerr effect is lower than the results of single crystals in Ref. [54]. Fig. 5-5c shows longitudinal Kerr spectra of $Ce_{0.36}$TbIG at temperatures above and below T_{comp}. Below T_{comp} the octahedral Fe^{3+} and dodecahedral Tb^{3+} plus Ce^{3+} moments are oriented parallel to the field while the tetrahedral Fe^{3+} moments are antiparallel [58]. The Kerr rotation of the two datasets at 120 and 320 K have opposite signs as the orientation of the sublattices reverses at $T_{comp.}$ This change in sign is because the Kerr rotation like Faraday rotation is sensitive to the magnetic sublattices rather than the net magnetization [58,59]. $Ce_{0.36}$TbIG has a polar Kerr spectrum similar to that of single crystal CeYIG. [17] Fig. 5-5d displays the temperature-dependent polar Kerr rotation of $Bi_{0.03}$TbIG at 2.5 eV. The change in sign indicates T_{comp} in the range of ~220 K, similar to the value of ~230 K found using SQUID magnetometry.

5.1.4 Optical Characterization

A spectroscopic ellipsometer (J.A. Woollam RC2) was employed to acquire the spectra of the ellipsometric parameters PSI and DELTA. A set of three measurements at different angles of incidence were performed to enlarge the experimental dataset for subsequent fitting. For the fitting a model structure of a TbIG, $Ce_{0.36}$TbIG or $Bi_{0.03}$TbIG layer on an oxidized Si substrate was considered. The spectral dependence of complex refractive index (N = n+ik) of each garnet layer was parametrized by the sum of 4 Cody-Lorentz oscillators and their parameters were fitted together with the layer thickness and surface roughness. The resulting spectra of refraction index and extinction coefficient, n and k, for the three TbIG, CeTbIG and BiTbIG samples are shown in Fig. 5-6a and 5-6b and the spectrally dependent absorption coefficient is shown in Fig. 5-6c. The spectral behavior of n and k in Fig. 5-6 a,b is typical for ferrimagnetic garnets [12,56,57,60,61] with the absorption edge around 2eV.

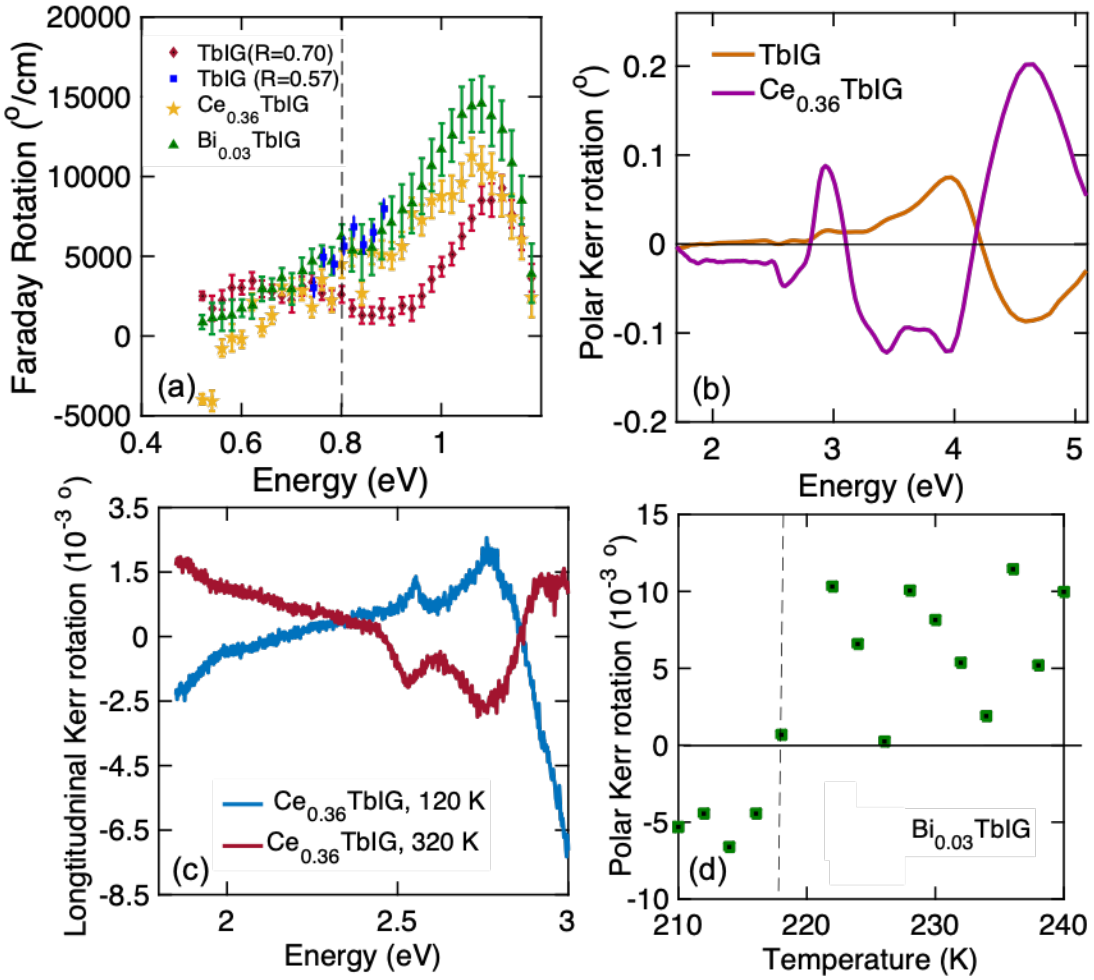

Figure 5-6: *(a) Room temperature Faraday rotation spectra of TbIG, $Ce_{0.36}$TbIG and $Bi_{0.03}$TbIG films (b) Room temperature polar Kerr rotation spectra of TbIG and $Ce_{0.36}$TbIG films. (c) Temperature-dependent longitudinal Kerr rotation of $Ce_{0.36}$TbIG. (d) Polar Kerr rotation versus temperature of $Bi_{0.03}$TbIG at energy 2.5eV, showing a sign change at T_{comp} in the range of ~220 K.*

We were unable to estimate the absorption of the 300 nm TbIG (R=0.54eV) film under 2eV from ellipsometric measurements, since this particular thickness leads to high interference in the low energy region and large depolarization. From Fig. 5-6b one can see a slight red shift of the onset of absorption for Bi and Ce samples. The shift towards lower energies induced by increasing the amount of Bi in YIG is well reported. [56,62]

The CeTbIG and BiTbIG had lower absorption than the TbIG at 1550 nm as shown in Table 2. The absorption of TbIG at 1550 nm can be attributed to the tail extending from a Faraday rotation and optical absorption line at λ=1850 nm from inner 4f electronic transitions in the Tb^{3+} ion. [23,27,63] While rare earths predominately occur in the trivalent state, Tb^{3+} only has one electron above the half-filled 4f shell and therefore is known to readily oxidize to Tb^{4+}, especially in cubic materials. [35,64-66] Tb^{4+} has been reported to be a quenching site of fluorescence for its strong and broad absorption in the visible region.[62] High resolution XPS data from the TbIG, CeTbIG and BiTbIG films shows potentially the presence of Tb^{4+} in all three films, Fig. 5-6e which is in accordance with results from single crystal TbIG films [35]. The higher intensity of the Tb^{4+} peak can be qualitatively interpretated as a larger proportion of Tb^{4+} than Tb^{3+} in these films. [35,67] Moreover, the intensity of Tb^{4+} relative to Tb^{3+} peaks was stronger in the TbIG film compared to $Ce_{0.36}$TbIG and $Bi_{0.03}$TbIG films pointing towards potentially a higher fraction of Tb^{4+} in TbIG compared to the other two films. The XPS spectra of Fe 2p in TbIG reveal a shift to a lower binding energy compared to the $Ce_{0.36}$TbIG and $Bi_{0.03}$TbIG films. A shift to lower binding energy of the Fe $2p_{3/2}$ peak in Fe_3O_4 has been associated with a reduction of Fe^{3+} to Fe^{2+} [68] due to the lower binding energies associated with Fe^{2+} compounds than Fe^{3+} compounds [68,69]. This higher amount of Fe^{2+} in the TbIG films correlates with the higher amount of Tb^{4+} and has been reported in other rare earth iron garnets as a result of the presence of tetravalent ion impurities. [63,70-72] The presence of Fe^{2+} in iron garnets results in enhanced absorption due to the relaxation of Fe^{3+} - Fe^{2+} where an electron promoted by a photon in Fe^{2+} transfers to a nearby Fe^{3+} ion. This relaxation process is associated with a large change in dipole moment and strong absorption, and at high concentrations of tetravalent ions the absorption is reported to be proportional to the number of tetravalent ions (here Tb^{4+}) because they increase the number of Fe^{2+} ions. [63,70]

In addition to Fe^{3+}-Fe^{2+} relaxation, the simultaneous presence of Tb^{4+} and Tb^{3+} can also affect the optical properties of the garnet films. [64] The electron donor behavior of Tb^{3+} allows electronic transitions from 4f → 4f and 4f→5d between 1.2 and 6eV while the electron acceptor behavior of Tb^{4+} allows charge transfer from ligand orbitals to rare earth or Fe^{3+} ions. [64] These potential absorption pathways including that fact that TbIG has an absorption peak near IR result in TbIG having higher absorption than YIG or BiYIG. [12] However, we find moderate

additions of Ce^{3+} and very small additions of Bi^{3+} are able to reduce this absorption to less than half as shown in Table 5-2 and also depicted in Fig. 5-6c. The Bi^{3+} and Ce^{3+} ions are associated with lower amounts of Tb^{4+} and Fe^{2+} as indicated by XPS, lowering the absorption coefficient significantly. Nonetheless, the TbIG (R=0.57) has a good MO FoM of 310 $°dB^{-1}$ compared to the FoM of 38 $°dB^{-1}$ for polycrystalline CeYIG. [12] As a result of having both a lower absorption than TbIG albeit a slightly smaller Faraday rotation due to the negative contribution of Ce^{3+}, the $Ce_{0.36}$TbIG film has a FoM almost 2 times higher than that of TbIG. $Bi_{0.03}$TbIG triumphs with a FoM of 720$°dB^{-1}$as shown in Fig. 5-6c. The small amount of Bi^{3+} does not negatively impact the Faraday rotation but it reduces the optical absorption significantly. So far, the highest FoM of 769$°dB^{-1}$ was reported [12] for polycrystalline BiYIG with a 40 nm bottom YIG seed layer, and the $Bi_{0.03}$TbIG in this work has the advantage of having a similarly high FoM while allowing for simpler fabrication and better device performance by eliminating the seed layer.

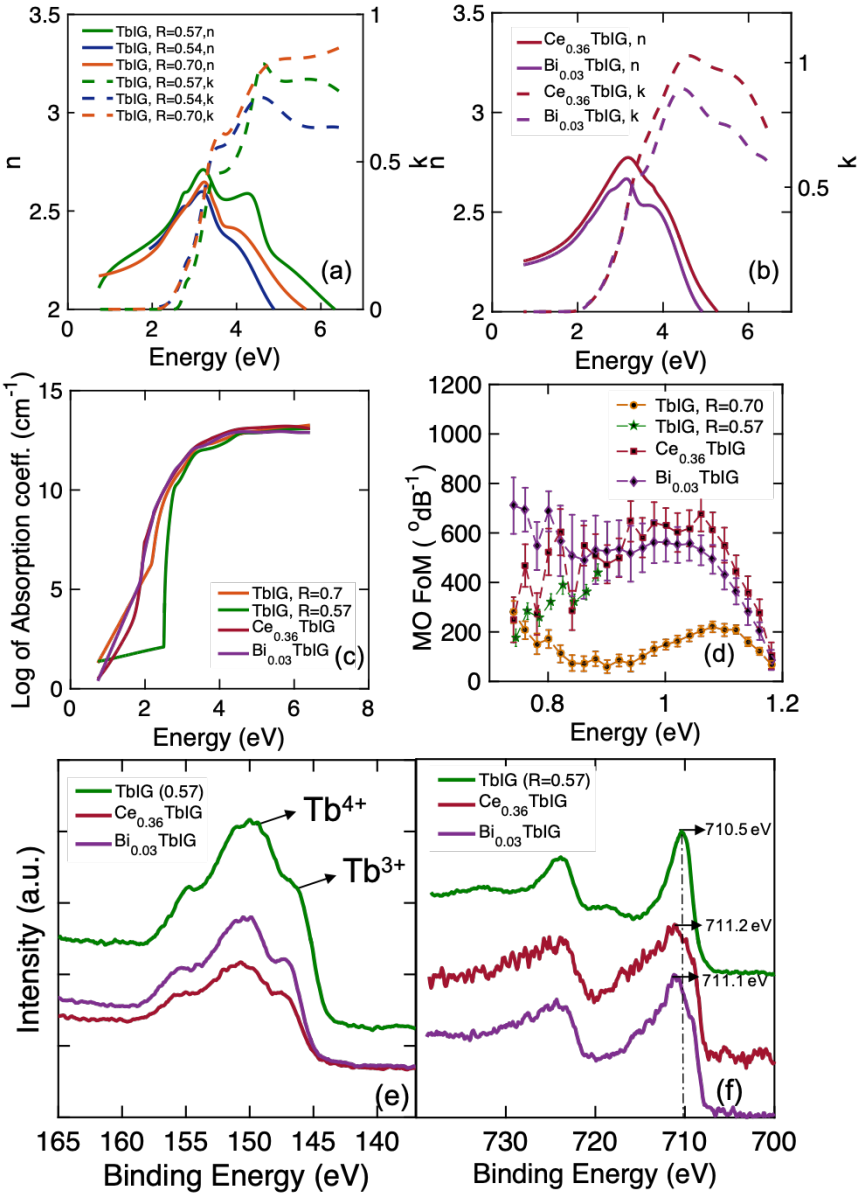

Figure 5-6: *Refractive index (n) and extinction coefficient (k) spectra of (a) TbIG (R=0.54, 0.57, 0.7), (b) $Ce_{0.36}$TbIG and $Bi_{0.03}$TbIG films. (c) Spectral dependence of absorption coefficient of TbIG, $Ce_{0.36}$TbIG and $Bi_{0.03}$TbIG films. (d) MO figure of merit (FoM) versus energy for TbIG (R=0.57,0.7) , $Ce_{0.36}$TbIG and $Bi_{0.03}$TbIG films. High resolution XPS spectra of (e) Tb 4d and (f) Fe 2p of the TbIG (R=0.57) , $Ce_{0.36}$TbIG and $Bi_{0.03}$TbIG films.*

5.2 Concluding remarks and summary

TbIG, CeTbIG and BiTbIG films were grown directly on Si via PLD without a seed layer. The films exhibit the highest reported Faraday rotation for polycrystalline films at 1550 nm wavelength, up to 6200 °/cm for $Bi_{0.03}$TbIG films and a similar value for TbIG. Despite its high Faraday rotation, the TbIG films exhibited an higher optical absorption than that of CeTbIG and BiTbIG, that may be attributed to both the greater concentration of Tb^{4+} and potential Fe^{2+} that can facilitate absorption through Fe^{3+}-Fe^{2+} relaxation and charge transfer from ligand orbitals, and the 4f electronic transitions of Tb^{3+}. Addition of Ce and Bi lowered the absorption significantly by potentially reducing the effect of absorption pathways and 4f electronic transitions.

Although we followed the process of attributing the peaks in XPS to Tb^{4+} and Tb^{3+}, as was done in several works [35,67,73], it has been pointed out that the XPS spectra of Tb^{3+} compounds such as Tb_2O_3, as well as atomic Tb^{3+} calculations, also show the same two 4d peaks thus implying that Tb^{3+} is responsible for both [74-77]. Therefore, it is difficult to quantify the amount of any potential Tb^{4+}, from the XPS by deconvolving the two peaks and comparing their intensity. That said, having a possibly smaller amount of Tb^{4+} does not affect the conclusion of this work as we do not expect more than half of the Tb ions to exist in Tb^{4+} state as suggested by the intensities of the peaks from XPS. This work emphasizes the critical importance of controlling the Tb^{3+}/Tb^{4+} ratio, analogous to the improvement in MO performance obtained by controlling Ce^{4+} in CeYIG via growth conditions [78]. The high FoM and the single layer growth process make Ce and especially Bi-substituted TbIG attractive materials for integrated nonreciprocal photonic devices or for other applications requiring magnetooptical materials such as magnetophotonic crystals or other nonreciprocal magnetooptical metamaterials. [79,80]

References

[1] Dötsch, H., Bahlmann, N., Zhuromskyy, O., Hammer, M., Wilkens, L., Gerhardt, R., Hertel, P. and Popkov, A.F., 2005. Applications of magneto-optical waveguides in integrated optics. *JOSA B*, *22*(1), pp.240-253.

[2] Mizumoto, T., Shoji, Y. and Takei, R., 2012. Direct wafer bonding and its application to waveguide optical isolators. *Materials*, *5*(5), pp.985-1004.

[3] Mizumoto, T., Baets, R. and Bowers, J.E., 2018. Optical nonreciprocal devices for silicon photonics using wafer-bonded magneto-optical garnet materials. *MRS Bulletin*, *43*(6), pp.419-424.

[4] Stadler, B.J. and Mizumoto, T., 2013. Integrated magneto-optical materials and isolators: a review. *IEEE Photonics Journal*, *6*(1), pp.1-15.

[5] Du, Q., Fakhrul, T., Zhang, Y., Hu, J. and Ross, C.A., 2018. Monolithic magneto-optical oxide thin films for on-chip optical isolation. *MRS Bulletin*, *43*(6), pp.413-418.

[6] Shoji, Y. and Mizumoto, T., 2014. Magneto-optical non-reciprocal devices in silicon photonics. *Science and technology of advanced materials*.

[7] Huang, D., Pintus, P. and Bowers, J.E., 2018. Towards heterogeneous integration of optical isolators and circulators with lasers on silicon. *Optical Materials Express*, *8*(9), pp.2471-2483.

[8] Zhang, Y., Du, Q., Wang, C., Fakhrul, T., Liu, S., Deng, L., Huang, D., Pintus, P., Bowers, J., Ross, C.A. and Hu, J., 2019. Monolithic integration of broadband optical isolators for polarization-diverse silicon photonics. *Optica*, *6*(4), pp.473-478.

[9] Hansen, P., Witter, K. and Tolksdorf, W., 1983. Magnetic and magneto-optic properties of lead-and bismuth-substituted yttrium iron garnet films. *Physical Review B*, *27*(11), p.6608.

[10] Bi, L., Hu, J., Jiang, P., Kim, D.H., Dionne, G.F., Kimerling, L.C. and Ross, C.A., 2011. On-chip optical isolation in monolithically integrated non-reciprocal optical resonators. *Nature Photonics*, *5*(12), pp.758-762.

[11] Du, Q., Wang, C., Zhang, Y., Zhang, Y., Fakhrul, T., Zhang, W., Gonçalves, C., Blanco, C., Richardson, K., Deng, L. and Ross, C.A., 2018. Monolithic on-chip magneto-optical isolator with 3 dB insertion loss and 40 dB isolation ratio. *ACS photonics*, *5*(12), pp.5010-5016.

[12] Fakhrul, T., Tazlaru, S., Beran, L., Zhang, Y., Veis, M. and Ross, C.A., 2019. Magneto-optical Bi: YIG films with high figure of merit for nonreciprocal photonics. *Advanced Optical Materials*, *7*(13), p.1900056.

[13] Sun, X.Y., Du, Q., Goto, T., Onbasli, M.C., Kim, D.H., Aimon, N.M., Hu, J. and Ross, C.A., 2015. Single-step deposition of cerium-substituted yttrium iron garnet for monolithic on-chip optical isolation. *Acs Photonics*, *2*(7), pp.856-863.

[14] Bi, L., Hu, J., Jiang, P., Kim, H.S., Kim, D.H., Onbasli, M.C., Dionne, G.F. and Ross, C.A., 2013. Magneto-optical thin films for on-chip monolithic integration of non-reciprocal photonic devices. *Materials*, *6*(11), pp.5094-5117.

[15] Hu, J., Zhang, Y., Du, Q., Wang, C., Fakhrul, T., Zhang, Y., Liu, S., Deng, L., Goncalves, C., Blanco, C. and Richardson, K., 2020, February. Filling in the missing link: monolithic optical isolators on silicon with high performance, broadband operation, and polarization diversity. In *Photonic and Phononic Properties of Engineered Nanostructures X* (Vol. 11289, p. 112891L). International Society for Optics and Photonics.

[16] Goto, T., Onbaşlı, M.C. and Ross, C.A., 2012. Magneto-optical properties of cerium substituted yttrium iron garnet films with reduced thermal budget for monolithic photonic integrated circuits. *Optics express*, *20*(27), pp.28507-28517.

[17] Onbasli, M.C., Beran, L., Zahradník, M., Kučera, M., Antoš, R., Mistrík, J., Dionne, G.F., Veis, M. and Ross, C.A., 2016. Optical and magneto-optical behavior of cerium yttrium iron garnet thin films at wavelengths of 200–1770 nm. *Scientific reports*, *6*(1), pp.1-10.

[18] Yoshimoto, T., Goto, T., Isogai, R., Nakamura, Y., Takagi, H., Ross, C.A. and Inoue, M., 2016. Magnetophotonic crystal with cerium substituted yttrium iron garnet and enhanced Faraday rotation angle. *Optics express*, *24*(8), pp.8746-8753.

[19] Bauer, J.J., Rosenberg, E.R., Kundu, S., Mkhoyan, K.A., Quarterman, P., Grutter, A.J., Kirby, B.J., Borchers, J.A. and Ross, C.A., 2020. Dysprosium iron garnet thin films with perpendicular magnetic anisotropy on silicon. *Advanced Electronic Materials*, *6*(1), p.1900820.

[20] Zhang, Y., Du, Q., Wang, C., Yan, W., Deng, L., Hu, J., Ross, C.A. and Bi, L., 2019. Dysprosium substituted Ce: YIG thin films with perpendicular magnetic anisotropy for silicon integrated optical isolator applications. *APL Materials*, *7*(8), p.081119.

[21] Nielsen, J.W. and Dearborn, E.F., 1958. The growth of single crystals of magnetic garnets. *Journal of Physics and Chemistry of Solids*, *5*(3), pp.202-207.

[22] Wang, R., Yang, C., Fan, M., Wu, M., Wang, C., Yu, X., Zhu, J., Zhang, J., Li, G., Huang, Q. and Chen, D., 2013. Phase relationship of the TbO1. 81–Mn3O4–Fe2O3 system synthesized at 1200° C. *Journal of alloys and compounds*, *554*, pp.385-394.

[23] Tamaki, T., Kaneda, H. and Kawamura, N., 1991. Magneto-optical properties of (TbBi) 3Fe5O12 and its application to a 1.5 μm wideband optical isolator. *Journal of applied physics*, *70*(8), pp.4581-4583.

[24] Umezawa, H., Yokoyama, Y. and Koshizuka, N., 1988. Temperature dependence of Faraday rotation in Bi-substituted terbium iron garnet films. *Journal of Applied Physics*, *63*(8), pp.3113-3115.

[25] Honda, Y., Ishikawa, T. and Hibiya, T., 1987. Temperature dependence of Faraday rotation for Bi-substituted Tb iron garnet films. *Journal of the Magnetics Society of Japan*, *11*(S_1_ISMO), pp.S1_361-364.

[26] Guillot, M., Le Gall, H., Desvignes, J.M. and Artinian, M., 1994. Faraday rotation of bismuth substituted terbium iron garnets. *IEEE Transactions on Magnetics*, *30*(6), pp.4419-4421.

[27] Fratello, V.J., Licht, S.J. and Brandle, C.D., 1996. Innovative improvements in bismuth-doped rare-earth iron garnet Faraday rotators. *IEEE Transactions on Magnetics*, *32*(5), pp.4102-4107.

[28] Park, I.J., Kang, K.U. and Kim, C.S., 2006. Temperature-dependent magnetic properties of bismuth substituted terbium–iron garnets. *IEEE transactions on magnetics*, *42*(10), pp.2882-2884.

[29] Dulal, P., Block, A.D., Gage, T.E., Haldren, H.A., Sung, S.Y., Hutchings, D.C. and Stadler, B.J., 2016. Optimized magneto-optical isolator designs inspired by seedlayer-free terbium iron garnets with opposite chirality. *ACS Photonics*, *3*(10), pp.1818-1825.

[30] Block, A.D., Dulal, P., Stadler, B.J. and Seaton, N.C., 2013. Growth parameters of fully crystallized YIG, Bi: YIG, and Ce: YIG films with high faraday rotations. *IEEE Photonics Journal*, *6*(1), pp.1-8.

[31] Srinivasan, K., Zhang, C., Dulal, P., Radu, C., Gage, T.E., Hutchings, D.C. and Stadler, B.J., 2019. High-gyrotropy seedlayer-free Ce: TbIG for monolithic laser-matched SOI optical isolators. *ACS Photonics*, *6*(10), pp.2455-2461.

[32] Srinivasan, K., Radu, C., Bilardello, D., Solheid, P. and Stadler, B.J., 2020. Interfacial and bulk magnetic properties of stoichiometric cerium doped terbium iron garnet polycrystalline thin films. *Advanced Functional Materials*, *30*(15), p.2000409.

[33] Dulal, P., Gage, T.E., Block, A.D., Cofell, E., Hutchings, D.C. and Stadler, B.J., 2016, October. Sputter-deposited seedlayer-free cerium-doped terbium iron garnets for SOI waveguide isolators. In *2016 IEEE Photonics Conference (IPC)* (pp. 773-774). IEEE.

[34] Srinivasan, K., Gage, T.E. and Stadler, B.J., 2018, May. Seed-layer free cerium-doped terbium iron garnet on non-garnet substrates for photonic isolators. In *CLEO: Science and Innovations* (pp. SW4I-5). Optical Society of America.

[35] Rosenberg, E.R., Beran, L., Avci, C.O., Zeledon, C., Song, B., Gonzalez-Fuentes, C., Mendil, J., Gambardella, P., Veis, M., Garcia, C. and Beach, G.S., 2018. Magnetism and spin transport in rare-earth-rich epitaxial terbium and europium iron garnet films. *Physical Review Materials*, *2*(9), p.094405.

[36] Clark, A. E., and R. E. Strakna. "Elastic constants of single-crystal YIG." *Journal of Applied Physics* 32, no. 6 (1961): 1172-1173.

[37] Iida, S., 1967. Magnetostriction constants of rare earth iron garnets. *Journal of the Physical Society of Japan*, *22*(5), pp.1201-1209.

[38] Akulov, N.S., 1930. Über die Anwendungen des Gesetzes ferromagnetischer Anisotropie zur Berechnung der Eigenschaften polykristallinischen Eisens. *Zeitschrift für Physik*, *66*(7-8), pp.533-542.

[39] Callen, H.B. and Goldberg, N., 1965. Magnetostriction of polycrystalline aggregates. *Journal of Applied Physics*, *36*(3), pp.976-977.

[40] Bauer, J.J., Rosenberg, E.R. and Ross, C.A., 2019. Perpendicular magnetic anisotropy and spin mixing conductance in polycrystalline europium iron garnet thin films. *Applied Physics Letters*, *114*(5), p.052403.

[41] Geller, S., Espinosa, G.P. and Crandall, P.B., 1969. Thermal expansion of yttrium and gadolinium iron, gallium and aluminum garnets. *Journal of Applied Crystallography*, *2*(2), pp.86-88.

[42] Lim, S.H., Murakami, M., Sarney, W.L., Ren, S.Q., Varatharajan, A., Nagarajan, V., Fujino, S., Wuttig, M., Takeuchi, I. and Salamanca-Riba, L.G., 2007. The effects of multiphase formation on strain relaxation and magnetization in multiferroic BiFeO3 thin films. *Advanced Functional Materials*, *17*(14), pp.2594-2599.

[43] H. P. J. Wijn, 1991. *Garnets (*Vol. 27e) Springer-Verlag, Berlin, Heidelberg

[44] Comstock, R.L. and Raymond, J.J., 1967. Magnetostriction of ytterbium and cerium in YIG. *Journal of Applied Physics*, *38*(9), pp.3737-3739.

[45] Lage, E., Beran, L., Quindeau, A.U., Ohnoutek, L., Kucera, M., Antos, R., Sani, S.R., Dionne, G.F., Veis, M. and Ross, C.A., 2017. Temperature-dependent Faraday rotation and magnetization reorientation in cerium-substituted yttrium iron garnet thin films. *APL Materials*, *5*(3), p.036104.

[46] Dionne, G.F., 2009. *Magnetic oxides* (Vol. 14, p. 15). New York: Springer.

[47] Hong, Y.J., Kum, J.S., Shim, I.B. and Kim, C.S., 2004. Spin rotation at compensation point studies of Tb/sub 3/Fe/sub 5/O/sub 12/by Mo/spl uml/ssbauer spectroscopy. *IEEE transactions on magnetics*, *40*(4), pp.2808-2810.

[48] Dionne, G.F., 1970. Molecular field coefficients of substituted yttrium iron garnets. *Journal of Applied Physics*, *41*(12), pp.4874-4881.

[49] Dionne, G.F., 1976. Molecular-field coefficients of rare-earth iron garnets. *Journal of Applied Physics*, *47*(9), pp.4220-4221.

[50] M. Guillot, H. L. Gall, *J. Phys*. (Paris) **1977**, *38*, 871.

[51] Zhang, G.Y., Xu, X.W. and Chong, T.C., 2004. Faraday rotation spectra of bismuth-substituted rare-earth iron garnet crystals in optical communication band. *Journal of applied physics*, *95*(10), pp.5267-5270.

[52] Crossley, W.A., Cooper, R.W., Page, J.L. and Van Stapele, R.P., 1969. Faraday rotation in rare-earth iron garnets. *Physical Review*, *181*(2), p.896.

[53] Liang, X., Xie, J., Deng, L. and Bi, L., 2015. First principles calculation on the magnetic, optical properties and oxygen vacancy effect of CexY3− xFe5O12. *Applied Physics Letters*, *106*(5), p.052401.

[54] Thuy, N.P., Višňovský, Š., Prosser, V., Krishnan, R. and Vien, T.K., 1981. Magnetooptical polar Kerr effect and reflectivity of terbium iron garnet between 2 and 6 eV. *Journal of Applied Physics*, *52*(3), pp.2292-2294.

[55] *Wittekoek, S., Popma, T.J., Robertson, J.M. and Bongers, P.F., 1975. Magneto-optic spectra and the dielectric tensor elements of bismuth-substituted iron garnets at photon energies between 2.2-5.2 eV. Physical review B, 12(7), p.2777*.

[56] Kucera, M., Bok, J. and Nitsch, K., 1989. Faraday rotation and MCD in Ce doped yig. *Solid state communications*, *69*(11), pp.1117-1121.

[57] Hansen, P. and Krumme, J.P., 1984. Magnetic and magneto-optical properties of garnet films. *Thin solid films*, *114*(1-2), pp.69-107.

[58] Zvezdin, A. K., & Kotov, V. A. (1997). *Modern magnetooptics and magnetooptical materials*. CRC Press.

[59] Ganzhorn, K., Barker, J., Schlitz, R., Piot, B.A., Ollefs, K., Guillou, F., Wilhelm, F., Rogalev, A., Opel, M., Althammer, M. and Geprägs, S., 2016. Spin Hall magnetoresistance in a canted ferrimagnet. *Physical Review B*, *94*(9), p.094401.

[60] Dionne, G.F. and Allen, G.A., 1993. Spectral origins of giant Faraday rotation and ellipticity in Bi-substituted magnetic garnets. *Journal of applied physics*, *73*(10), pp.6127-6129.

[61] Scott, G.B. and Lacklison, D., 1976. Magnetooptic properties and applications of bismuth substituted iron garnets. *IEEE Transactions on Magnetics*, *12*(4), pp.292-311.

[62] Jesenska, E., Yoshida, T., Shinozaki, K., Ishibashi, T., Beran, L., Zahradnik, M., Antos, R., Kučera, M. and Veis, M., 2016. Optical and magneto-optical properties of Bi substituted yttrium iron garnets prepared by metal organic decomposition. *Optical Materials Express*, *6*(6), pp.1986-1997.

[63] Wood, D. L., and J. P. Remeika. "Effect of impurities on the optical properties of yttrium iron garnet." *Journal of Applied Physics* 38, no. 3 (1967): 1038-1045.

[64] Verma, R.K., Kumar, K. and Rai, S.B., 2010. Inter-conversion of Tb3+ and Tb4+ states and its fluorescence properties in MO–Al2O3: Tb (M= Mg, Ca, Sr, Ba) phosphor materials. *Solid state sciences*, *12*(7), pp.1146-1151.

[65] Lu, D.Y., 2015. Self-adjustable site occupations between Ba-site Tb3+ and Ti-site Tb4+ ions in terbium-doped barium titanate ceramics. *Solid State Ionics*, *276*, pp.98-106.

[66] Ebendorff-Heidepriem, H. and Ehrt, D., 1999. Electron spin resonance spectra of Eu2+ and Tb4+ ions in glasses. *Journal of Physics: condensed matter*, *11*(39), p.7627.

[67] Gnanasekar, K.I., Selvam, P., Keer, H.V., Pinto, R., Purandare, S.C., Tamhane, A.S., Gupta, L.C. and Vijayaraghavan, R., 1994. Superconductivity and valence state of Tb in Lu1− x Tb x Ba2Cu3O7− δ (0≤ x≤ 0.7). *Applied physics letters*, *65*(10), pp.1296-1298.

[68] Mills, P. and Sullivan, J.L., 1983. A study of the core level electrons in iron and its three oxides by means of X-ray photoelectron spectroscopy. *Journal of Physics D: Applied Physics*, *16*(5), p.723.

[69] G.C. Allen, M.T. Curtis, A.J. Hooper, P.M. Tucker, J. Chem. Soc., Dalton Trans. **1974**,14, 1525.

[70] Wood, D.L. and Remeika, J.P., 1966. Optical Transparency of Rare-Earth Iron Garnets. *Journal of Applied Physics*, *37*(3), pp.1232-1233.

[71] Lefever, R.A. and Chase, A.B., 1960. Substitutional incorporation of divalent iron in yttrium iron garnet. *The Journal of Chemical Physics*, *32*(5), pp.1575-1576.

[72] Wickersheim, K.A. and Lefever, R.A., 1962. Absorption spectra of ferric iron-containing oxides. *The Journal of Chemical Physics*, *36*(3), pp.844-850.

[73] Khurana, B., Bauer, J.J., Zhang, P., Safi, T., Chou, C.T., Hou, J.T., Fakhrul, T., Fan, Y., Liu, L. and Ross, C.A., 2021. Magnetism and spin transport in platinum/scandium-substituted terbium iron garnet heterostructures. *Physical Review Materials*, *5*(8), p.084408.

[74] Kotani, A. and Ogasawara, H., 1992. Theory of core-level spectroscopy of rare-earth oxides. *Journal of electron spectroscopy and related phenomena*, *60*(4), pp.257-299. (most cited)

[75]Goedkoop, J.B., Thole, B.T., Van der Laan, G., Sawatzky, G.A., De Groot, F.M.F. and Fuggle, J.C., 1988. Calculations of magnetic x-ray dichroism in the 3d absorption spectra of rare-earth compounds. *Physical Review B*, *37*(4), p.2086.

[76] Ogasawara, H., Kotani, A. and Thole, B.T., 1994. Lifetime effect on the multiplet structure of 4d x-ray-photoemission spectra in heavy rare-earth elements. *Physical Review B*, *50*(17), p.12332.

[77] Biagi, R., Fernandez-Rodriguez, J., Gonidec, M., Mirone, A., Corradini, V., Moro, F., De Renzi, V., Del Pennino, U., Cezar, J.C., Amabilino, D.B. and Veciana, J., 2010. X-ray absorption and magnetic circular dichroism investigation of bis (phthalocyaninato) terbium single-molecule magnets deposited on graphite. *Physical Review B*, *82*(22), p.224406.

[78] Zhang, Y., Wang, C.T., Liang, X., Peng, B., Lu, H.P., Zhou, P.H., Zhang, L., Xie, J.X., Deng, L.J., Zahradnik, M. and Beran, L., 2017. Enhanced magneto-optical effect in Y1. 5Ce1. 5Fe5O12 thin films deposited on silicon by pulsed laser deposition. *Journal of Alloys and Compounds*, *703*, pp.591-599.

[79] Ignatyeva, D.O., Karki, D., Voronov, A.A., Kozhaev, M.A., Krichevsky, D.M., Chernov, A.I., Levy, M. and Belotelov, V.I., Nature Communications, **2020**. 11(1), pp.1-8.

[80] Davoyan, A.R., Mahmoud, A.M. and Engheta, N., 2013. Optical isolation with epsilon-near-zero metamaterials. *Optics Express*, *21*(3), pp.3279-3286.

6. Ultra-low damping BiYIG films facilitating exceptionally high domain wall motion

6.0 Introduction and Motivation

Magnetic materials with perpendicular magnetic anisotropy (PMA) and low Gilbert damping (α) hold great promise towards faster and smaller magnetic bits in information storage technology. Tremendous progress has been made to find PMA materials with higher speeds and lower energy consumption for use in a wide range of spintronic devices from spin-transfer-torque (STT) memory, spin-orbit-torque (SOT) devices, magnetic-tunnel junction sensors, racetrack memory and even spin-wave logic [1-4] . However, the magnetic films used in such applications require not only PMA, that ensures higher density, scalability and thermal stability, but also a very low Gilbert damping constant [5]. Higher damping translates to larger critical currents required for magnetization reversal by STT and also lower domain wall velocities in racetrack memory where domain wall velocity is usually inversely proportional to α [5-7]. As a result, the search to find and study materials with a combination of both PMA and lower damping becomes one of significant technological importance.

Conventional PMA metallic ferromagnets pose a problem because of their stray fields limit bit size while their considerably high damping losses limit read/write speeds and energy efficiency [8,9]. Magnetic insulators like ferrimagnetic rare earth iron garnets with PMA have recently attracted a great deal of attention for spintronic devices for their low power and high-frequency magnetization dynamics [10-12]. However, a major drawback for most rare earth iron garnets is their large Gilbert damping relative to non-RE garnets [13,14]. On the other hand, magnetic insulators like Yttrium iron garnet (YIG) became the center of intense research because it has the lowest magnetic damping among all known magnetic materials [15,16]. Unfortunately, YIG thin films generally do not show PMA due to YIG's weak magneto crystalline and magnetoelastic anisotropy that fails to dominate the in-plane shape anisotropy. Yet, there have been a few reports on PMA YIG by techniques including using $Sm_3Ga_5O_{12}$ buffer layers on garnet substrates that allow PMA up to 20nm thickness [17]. No information on the damping of these buffer layer grown YIG films have been provided. More recently, Ding et. al. have

reported growth of PMA YIG films up to 9nm thick on substituted gallium gadolinium garnet substrates [18]. However, the films have high Ferromagnetic resonance (FMR) linewidth larger than 32 mT. A recent report shows that Bismuth substituted yttrium iron garnet (BiYIG) combines the advantages of PMA in conventional rare earth iron garnets while also demonstrating low damping shown in YIG [19]. The first demonstration of PMA BiYIG was reported by Soumah et. al. [19] where BiYIG was grown on substituted gadolinium galium garnet (SGGG). However, the reported damping of 3×10^{-4} was measured at a 27° angle from the out-of-plane polar angle in the narrow frequency range of 8-17 GHz. The out-of-plane FMR linewidth was reported to be quite high at 18mT. Further reports of PMA BiYIG grown on SGGG show out of-plane damping of of 7.03×10^{-4} [20] in the narrow frequency range of 6-13 GHz. These reports warrant further study of PMA BiYIG as the current literature only reports linewidth measurement in both a narrow and low frequency range where nonlinearities in linewidth have been reported in both metallic systems [21] and insulating oxides like YIG [22] owing to slow-relaxing impurity mechanism.

In this work we will report the growth, FMR, magnetic and spintronic properties of ultra-low damping PMA BiYIG that has allowed us to demonstrate record current-driven domain wall velocities of up to 4.5 km/s [23]. The BiYIG films are grown epitaxially on a range of (111) oriented garnet substrates with varying lattice parameters that result in high quality single crystal PMA films due to magnetoelastic and growth induced anisotropy. The equilibrium domains and reversal characteristics of the films are investigated by MOKE imaging. FMR characterization reveals damping as low as 1.3×10^{-4} with a linewidth as small as 3.4 mT. Finally, a lower bound for the spin mixing conductance is reported which is in par with previous reports for PMA rare earth iron garnets having the highest reported spin mixing conductance.

6.1 Structural and Magnetic characterization

BiYIG films ranging from 7-70 nm in thickness were grown by pulsed laser deposition (PLD) on (111) oriented substituted gadolinium gallium garnets of composition $Gd_{2.6}Ca_{0.4}Ga_{4.1}Mg_{0.25}Zr_{0.65}O_{12}$ (SGGG), $Gd_3Sc_2Ga_3O_{12}$ (GSGG) and (111) $Nd_3Ga_5O_{12}$ (NGG). The target used for the thin film growth had a composition of $Bi_{0.8}Y_{2.2}Fe_5O_{12}$. The chamber was pumped to 5×10^{-6} Torr base pressure prior to introducing oxygen and depositing the films. The laser repetition rate was 10 Hz, the laser fluence was ~2 J/cm^2, and the target-substrate distance was 6 cm. The substrate temperature was 560^{o}C and the O_2 pressure was 150mTorr. After growth the samples were cooled down under 230 Torr of O_2.

The lattice parameters of the SGGG, NGG and GSGG were 12.480 Å, 12.505Å and 12.554 Å respectively. Since Bi has a larger ionic radius than Y, it causes a YIG expansion of 0.083 Å per Bismuth atom substituted in a formula unit [24], resulting in a lattice parameter of 12.45 Å for $Bi_{0.8}Y_{2.2}Fe_5O_{12}$. From the Laue fringes in the HRXRD $2\theta - \omega$ scans in Fig. 6-1 (a, b) it can be concluded that all the films are of high epitaxial quality growing under in-plane tensile strain. Lattice mismatch with the substrate causes distortion of the the unit cell of the BiYIG from cubic to rhombohedral (Fig. 6-1c) . Reciprocal space mapping (RSM) for the (642) reflection show that all of the BiYIG films upto 70nm on GSGG, NGG and SGGG were completely strained to the substrate. RSM for a 28.3 nm and 70nm BiYIG film on GSGG is shown in Fig. 6-1d, e. Atomic force microscopy (AFM) show the BiYIG films have a root mean square (RMS) surface roughness of less than 0.2 nm (Fig. 6-1f)

A rhombohedral-to-hexagonal transformation has been used to calculate the strain as detailed in our published work [26]. The high-quality and epitaxial nature of the growth is clear. The contrast in the STEM image indicates a Y-rich layer (~0.9 nm) near the GSGG interface and some Bi concentration fluctuations above this Y-rich layer as shown in Fig. 6-2 b,c. High-resolution HAADF STEM images of a 4nmPt/6.9nm/BiYIG/GSGG film is shown in Fig.6-2a,b.

The magnetic properties of the films were characterized by VSM measurements. The in-plane and out-of-plane hysteresis loops are shown in Fig. 6-3 a-d. The films grown on GSGG and NGG demonstrate PMA with square hysteresis loops whereas films grown on SGGG were found to have in-plane easy axis. The large paramagnetic background signal of the GSGG, NGG and SGGG substrates prevented background subtraction for the in-plane hysteresis loop of most of the BiYIG films. BiYIG films grown on NGG show the lowest coercivity of 1.59 kA/m and films on GSGG had higher coercivity of 7.98 kA/m. The saturation magnetization of BiYIG was between 120-150kA/m varying over a thickness of 20-70nm on all the substrates.

The magnetic anisotropy of the films is made of contributions from magnetocrystalline, shape, magnetoelastic and growth-induced anisotropy contributions. The net uniaxial anisotropy K_u of the films is determined by the difference between the magnetic energy for magnetization oriented in-plane and the magnetization oriented out-of-plane as shown below:

$$K_u = E_{IP} - E_{OP} = K_{mc} + K_{me} + K_{sh} + K_g = -\frac{K_1}{12} + \frac{9}{4}\lambda_{111}c_{44}\left(\frac{\pi}{2} - \beta\right) - \frac{\mu_o}{2}M_s^2 + K_g \quad (1)$$

Here, K_1 is the first order cubic magnetocrystalline anisotropy constant, λ_{111} is the magnetostriction coefficient for the (111) BiYIG films, c_{44} is the shear modulus, β is the corner angle of the rhombohedrally-distorted unit cell as shown in Fig. 6-1c and M_S is the saturation magnetization. Here, a positive K_u corresponds to an out-of-plane easy axis and vice versa. The magnetocrystalline anisotropy K_1 for BiYIG being negative, favors PMA for (111) films but in this case is very small (650Jm^{-3} [27]) and thus can be neglected. The magnetoelastic anisotropy K_{me} is proportional to $\lambda_{111}$and the shear strain that is proportional to $\frac{\pi}{2} - \beta \,.\lambda_{111}$ for BiYIG is negative [27] and therefore favors easy axis along the compressive strain thus driving PMA in BiYIG films grown on larger lattice parameter substrates. The shape anisotropy, K_{sh} ,favors an in-plane magnetization.

Like Soumah et al. [19], we find that only magnetoelastic anisotropy is insufficient to account for the PMA in these films as shown in Table 1. Partially substituted garnet films like BiYIG exhibit another form of anisotropy that is known as growth induced anisotropy K_g due to the

nonrandom distribution of the dodecahedral site by the Bi^{3+}atoms. This kind of growth induced anisotropy has been observed in the past in mixed rare earth and other mixed composition garnets [28-32]. Similarly, in BiYIG there is a preferential occupation of the of Bi^{3+} into inequivalent dodecahedral sites based on the cation size of Bi^{3+} and Y^{3+}. This broken symmetry leads to additional uniaxial magnetic anisotropy in the (111) films. The distribution of the Bi^{3+} ions within the available sites depends on the orientation of the substrate [28, 33] and on the growth parameters. The magnitude and the sign of K_g depends both on the substituted atoms and their proportion of substitution and for Bi^{3+} is positive and favors PMA [34].

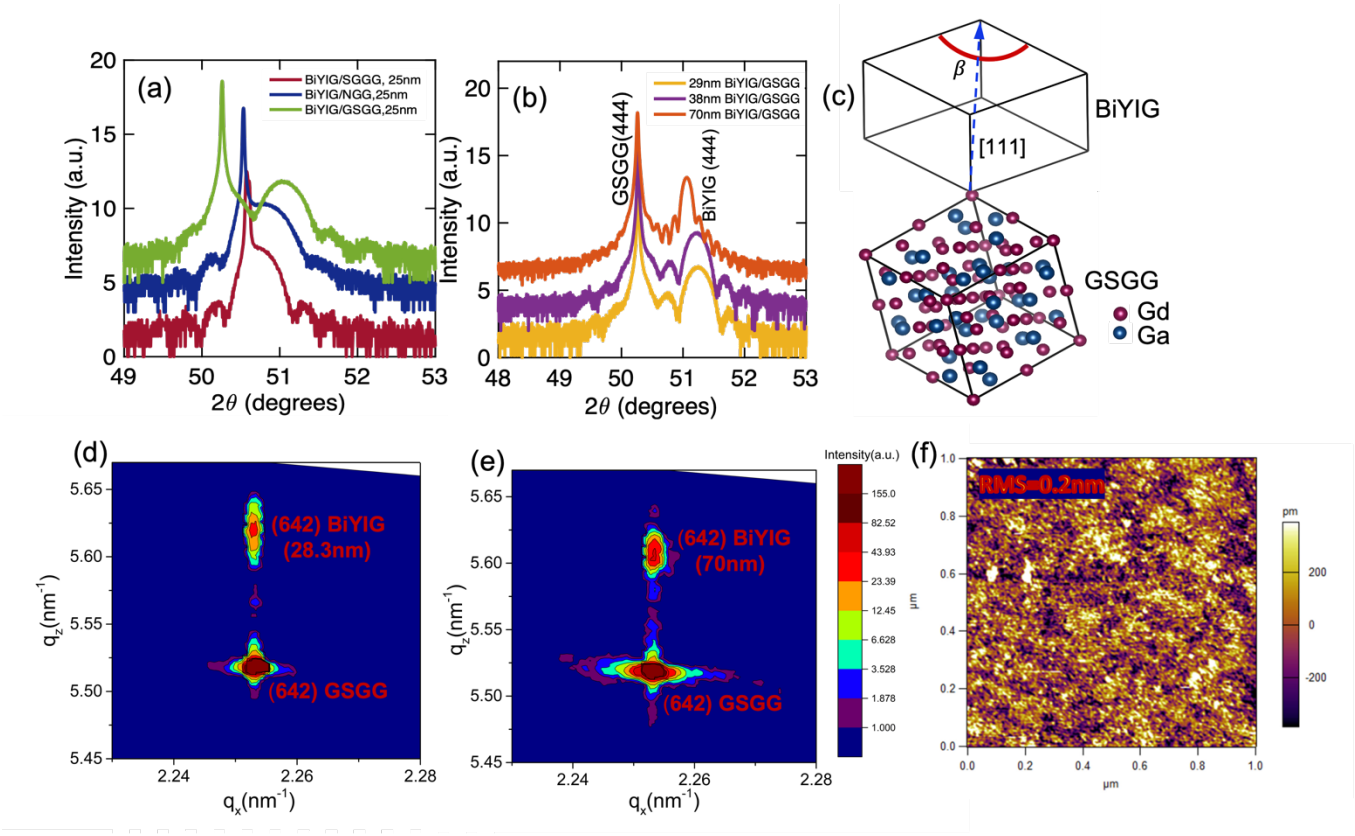

Figure 6-1: *(a,b) HRXRD ω −2Θ scans around the Bi:YIG (444) and, SGGG, GSGG and NGG (444) peaks for varying thicknesses of BiYIG. c) Schematic of a strained BiYIG cubic unit cell on GSGG with the corner angle β marked. HRXRD reciprocal space map of d) 28.3nm BiYIG/GSGG and e) 70nm BiYIG/GSGG. f) AFM scan on 7-nm-thick BiYIG film on GSGG.*

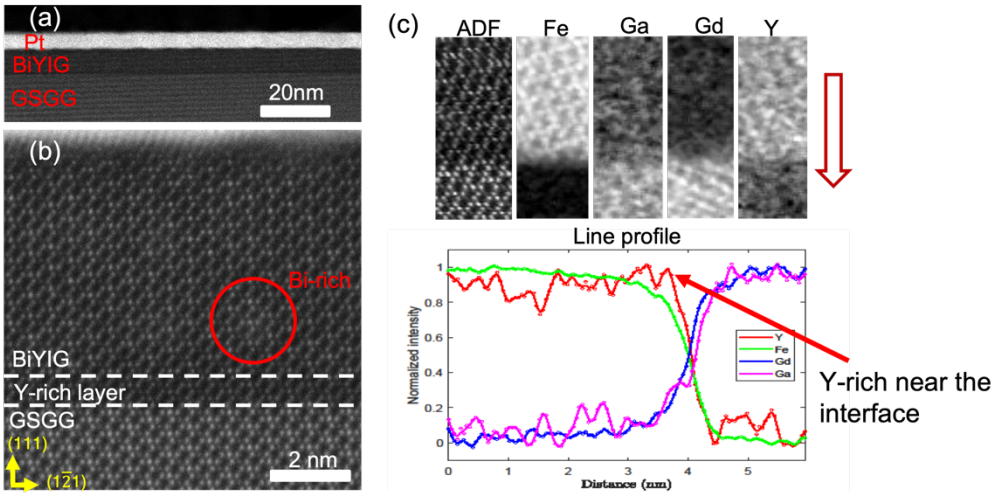

Figure 6-2: *(a-b) Scanning transmission electron microscopy of GSGG (111)/BiYIG (6.9 nm)/Pt(4 nm). c) Two-dimensional electron energy loss spectroscopy (EELS) maps across the interface for each elements, Fe, Ga, Gd and Y, as well as a simultaneously acquired annular dark-field (ADF) image.*

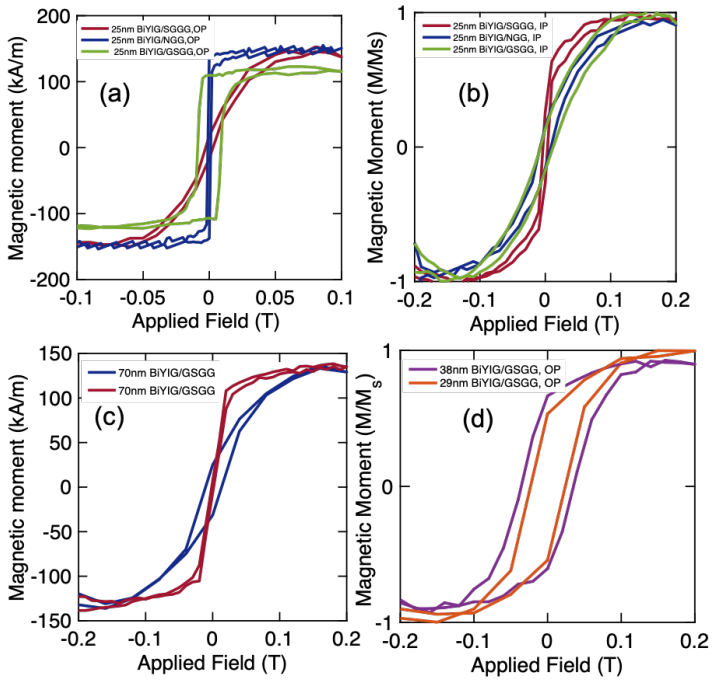

Figure 6-3: *(a) In-plane (IP) and (b) out-of-plane (OP) VSM hysteresis loops for 25nm BiYIG on SGGG, NGG and GSGG. (c) IP and OP VSM loops for 70nm BiYIG on GSGG. (d) OP VSM loops for 38 and 29nm BiYIG on GSGG.*

Table 1: Magnetic properties of BiYIG films on GSGG, NGG and SGGG substrates

Film thickness	Substrate	PMA	β (°)	K_u kJ/m^3	K_{shape} kJ/m^3	K_{me} kJ/m^3	$K_{shape}+K_{me}+K_{crystal}$ kJ/m^3	K_{growth} kJ/m^3	Domain shape	Avg. Equilibrium domain size µm
70nm	GSGG	Yes	90.58	17.9	-9.81	5.79	-3.97	21.87	stripe	--
25nm	SGGG	No	90.1	11.1	-14.1	1.74	-12.4	23.5	---	--
25nm	GSGG	Yes	90.58	30.18	-9.0	5.79	-36	33.44	Stripe	32 ± 8
28.3 nm	GSGG	Yes	90.7	49.2	-14.1	7.07	-4.93	54.13	triangular	67 ± 22
32.9nm	GSGG	Yes	90.7	44.8	-14.1	7.07	-4.48	49.3	triangular	84 ± 35
25nm	NGG	Yes	90.2	29.1	-13.4	2.22	-11.23	40.3	stripe	30 ± 9
26.5 nm	NGG	Yes	90.3	25.5	-11.1	3.03	-8.12	33.6	stripe	26 ± 8

6.2 MOKE Imaging

Magneto optical Kerr effect (MOKE) microscopy has been performed on BiYIG films with thicknesses 25 nm, 28 nm and 33 nm grown on GSGG substrates and 25 nm and 27 nm grown on NGG substrates. All the films were ac demagnetized using VSM with an exponentially decaying alternating magnetic field with an initial value of 5000 Oe and a reduction ratio of 0.95. MOKE images for the resulting low energy equilibrium domain structures for these films are shown in Fig. 6-4. Up and down domains occupy roughly equal areas so that the overall magnetization is close to zero. Average domain size calculated for all films using images taken from multiple locations on each film have been displayed in Table I. The large standard deviations for domain sizes in all films are indicative of heterogeneities in properties of PLD grown films like the net uniaxial anisotropy and the net magnetization.

MOKE images for ac demagnetized films with thickness 25 nm grown on GSGG substrate and 25 nm and 27 nm grown on NGG substrates show labyrinthine domain structure as shown in Fig. 6-4 a, d and e. However, some of the ac demagnetized BiYIG films with thicknesses 28 nm and 33 nm grown on GSGG substrates show triangular domains due to preferential formation of domain walls along certain crystallographic directions. (Fig. 6-3 b and c). Crystallographically oriented domain walls in ultrathin iron films grown on tungsten have been attributed to strain relaxation in a past studies [35]. Triangular domains have been reported in ultrathin CoFeB films on application of in-plane electric current and magnetic field [36]. While triangular domains have not been reported in bismuth iron garnets, there have been multiple reports of triangular threading and misfit dislocation defects in micron thick epitaxial bismuth iron garnet films grown by liquid phase epitaxy due to film-substrate lattice parameter misfit [37]. Machida et al. report triangular pits due to Pt inclusion potentially due to dislocation defects in micron thick $(YbTbBi)_3 Fe_5O_{12}$ films on SGGG [38]. Moreover, rare earth iron garnets (RIG) are known to have a larger thermal expansion (~8%) than rare earth gallium garnets (RGaG) and increasing Bi in iron garnets increases the thermal expansion even further causing distortion to the film due to stress exerted by the substrate [37]. Stress relieving dislocations can become energetically favorable when the dislocation formation energy is lower than the strain

energy required to maintain coherency and the formation of such dislocations would be a strong function of film thickness. Dislocation loops can nucleate at the surface of the growing film and expand downwards until they reach the interface. The kinetics of the formation and motion of the dislocation loops limit their generation. In garnets, the large Burgers vectors as a result of the large lattice parameter limits nucleation of dislocations at higher thicknesses [39]. Low thickness films increase the ease of nucleation of dislocations with increasing Bi substitutions. Van der Merwe [40] shows that the formation of misfit dislocations would be higher at a film-substrate with low bonding strength. It is reported in literature that the bonding of bismuth-iron garnets is lower than RIG because of the weaker Bi-O bonds compared to Y-O and R-O bonds which becomes more pronounced at higher temperatures. This qualitatively explains the ease of misfit dislocations in Bi containing iron garnets compared to other iron garnets.

The critical lattice mismatch causing the onset of triangular defects by misfit and threading dislocations has been reported to be 0.041 Å (at growth temperatures) in pure rare earth iron garnets which is even smaller in Bi-substituted garnets [37]. At room temperature our $Bi_{0.8}$YIG films have a lattice misfit of 0.104 Å with GSGG. The two films that nucleate triangular domains have higher β (higher lattice distortion) compared to similar thickness BiYIG films on GSGG that have equilibrium stripe domains as tabulated in Table 1. While RSM shows that triangular domain films are strained to the lattice as shown in Fig. 6-1d the films have ~60% higher anisotropy than other films of similar thickness as shown in Table 1. Thus, we speculate that these films may have localized strain relaxation with the formation of threading and partial dislocations. Thus, the domain walls in these films may form preferentially along dislocations due to favorable interaction with their strain fields which can lower domain wall energy. Resulting crystallographically oriented domain walls can cause domains to form in a particular shape like triangle.

MOKE microscopy has been used to study magnetization reversal for BiYIG films with thicknesses 28 nm and 70 nm grown on GSGG substrates and 25 nm grown on NGG substrate as shown in Fig. 5. MOKE images were continuously collected for all the films with application of an initial out-of-plane magnetic field of -600 Oe which was followed by an out-of-plane field sweep from 0 Oe to a suitably high positive value to saturate the film in the opposite direction. MOKE image collected for an out-of-plane field of -600 Oe was subtracted from all the subsequent images to remove the nonmagnetic contrast. Magnetization reversal for BiYIG films with thickness 70 nm grown on GSGG substrate and 25 nm grown on NGG substrate shown in Fig. 6-5 b and c proceed by formation of labyrinthine stripe domains. Similar domain structure has been reported for thulium iron garnet (TmIG) observed using scanning transmission x-ray microscopy [41] and yttrium-thulium iron garnet (YTmIG) observed using MOKE [42]. Magnetization reversal proceeds to near completion by 150 Oe for 70 nm thick BiYIG film grown on GSGG substrate and by 40 Oe for 25 nm thick BiYIG film grown on NGG substrate. Magnetization reversal for 28 nm thick BiYIG film grown on GSGG substrate proceeds by formation of triangular domains like those observed in its equilibrium domain structure along with stripe domains as shown in Fig. 6-5 a. However, this film has unreversed regions up to a magnetic field of 1000 Oe which is consistent with its VSM hysteresis loop shown in Fig. 6-3 d indicating a high saturation field.

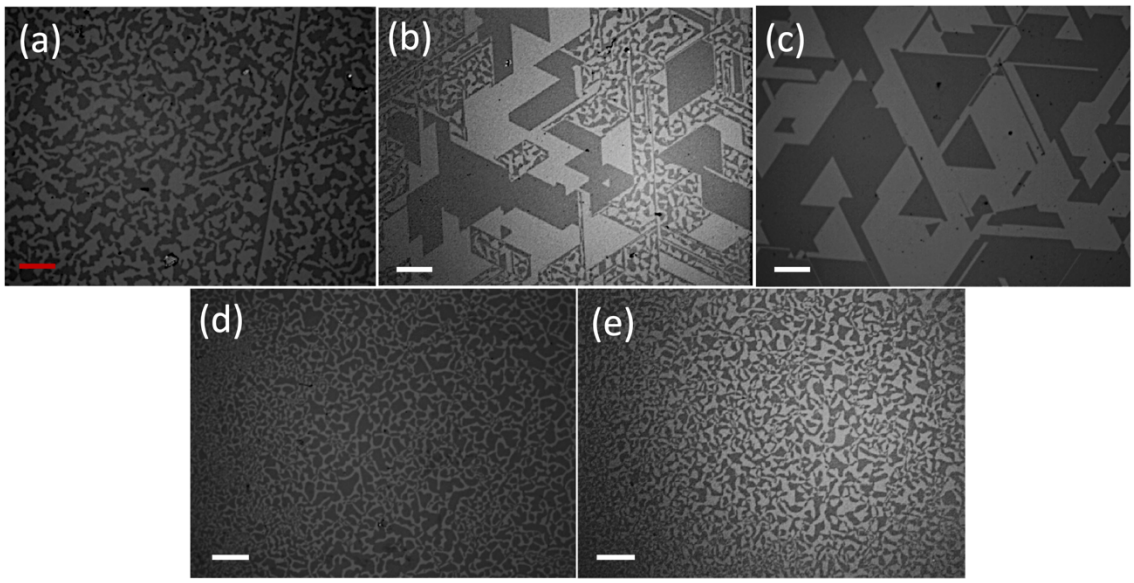

Figure 6-4: *MOKE images showing equilibrium domain structure after ac demagnetization of a) 25nm BiYIG/GSGG b) 28nm BiYIG/GSGG c) 33nm BiYIG/GSGG d) 26.5 nm BiYIG/NGG e) 25 nm BiYIG/NGG. The scale bar in red equals 50μm and the white scale bar equals 100μm.*

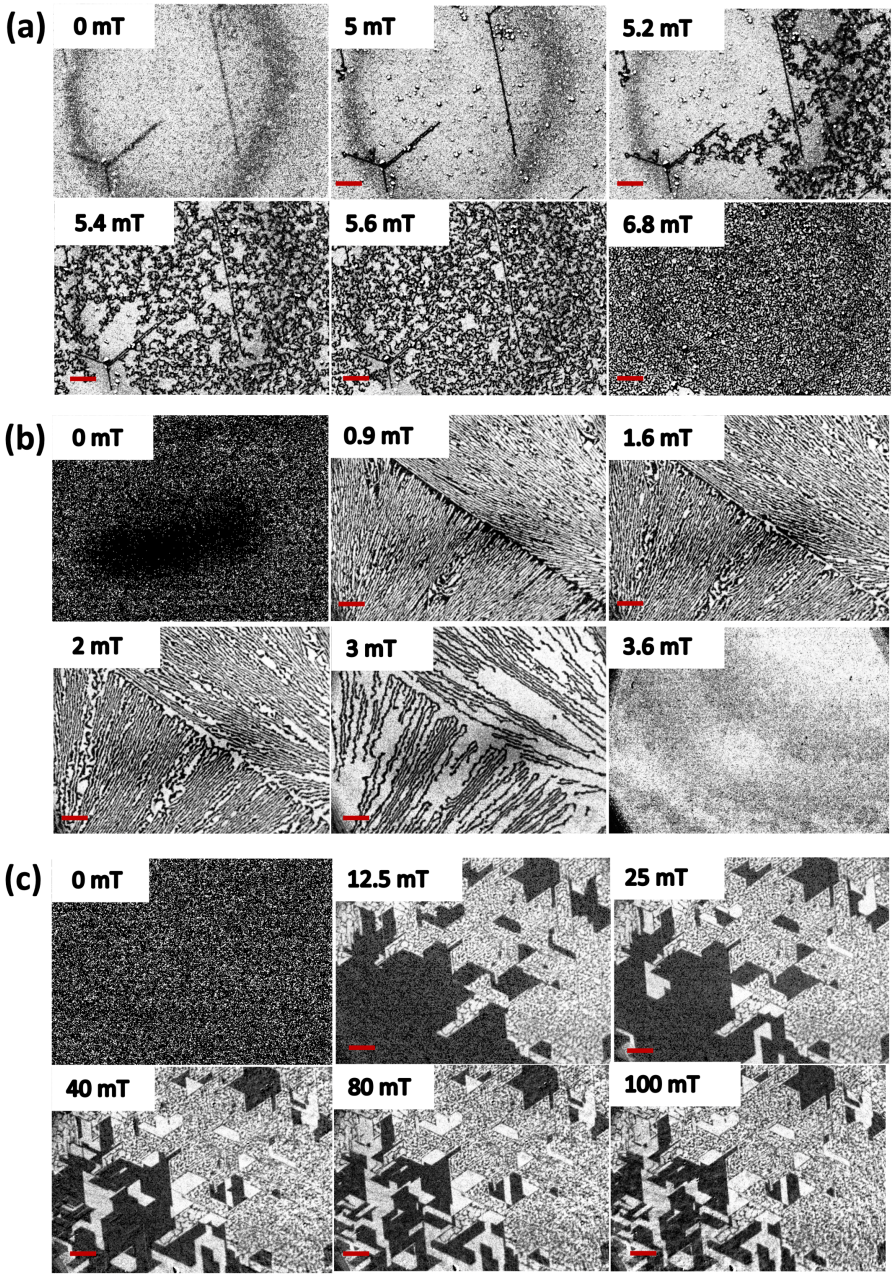

Figure 6-5: *MOKE images showing domain structure during reversal of a) 70 nm BiYIG/GSGG b) 25nm BiYIG/NGG c) 28 nm BiYIG/GSGG. The films were saturated at +60mT for a) and -60mT for b) and c). The red scale bar equals 100μm.*

6.3 Ferromagnetic Resonance (FMR) characterization

To extract the damping of the BiYIG thin films their dynamic magnetic properties were studied with broadband perpendicular FMR spectroscopy based on the vector network analyzer (VNA) technique [43-46]. The samples were placed face-down on a 50 Ω coplanar waveguide. A static out-of-plane magnetic field up to $\mu_0 H = 2.2$ T was swept to saturate the film in the out-of-plane direction. A variable microwave field was applied in-plane while the microwave transmission over a frequency from 10-40 GHz was measured. The complex transmission parameter S_{21} was measured at a fixed frequency while the external magnetic field was swept [43] as shown in Figure 6-3(a,b). The resonance field for the films were fitted to the Kittel equation for perpendicular geometry to extract the effective magnetization M_{eff} and the Landé g-factor g [47] as shown in Figure 3c for a chosen film. Here:

$$H_{res} = \frac{2\pi f}{|\gamma|\mu_0} + M_{eff}$$

where, H_{res} is the resonance field, f is the excitation frequency, and γ is the gyromagnetic ratio $(g\mu_B)/\hbar$ where μ_B is the Bohr magneton and ħ is the reduced Planck's constant. The anisotropy of the films , K_u, is extracted from M_{eff} from the equation [48,49]

$$M_{eff} = M_s - \frac{2K_u}{\mu_0 M_s}$$

The damping α was extracted by fitting the linewidth to the following expression:

$$\Delta H = \frac{4\pi\alpha f}{|\gamma|\mu_0} + \Delta H_0$$

where ΔH is the experimentally observed linewidth determined from fitting the S_{21} data with the complex susceptibility and ΔH_0 is the inhomogeneous broadening of the linewidth. Gilbert damping extracted from the BiYIG films were found to be as low as 1.3×10^{-4} with a linewidth as small as 3.4 mT as shown in Fig.6 (d-f).

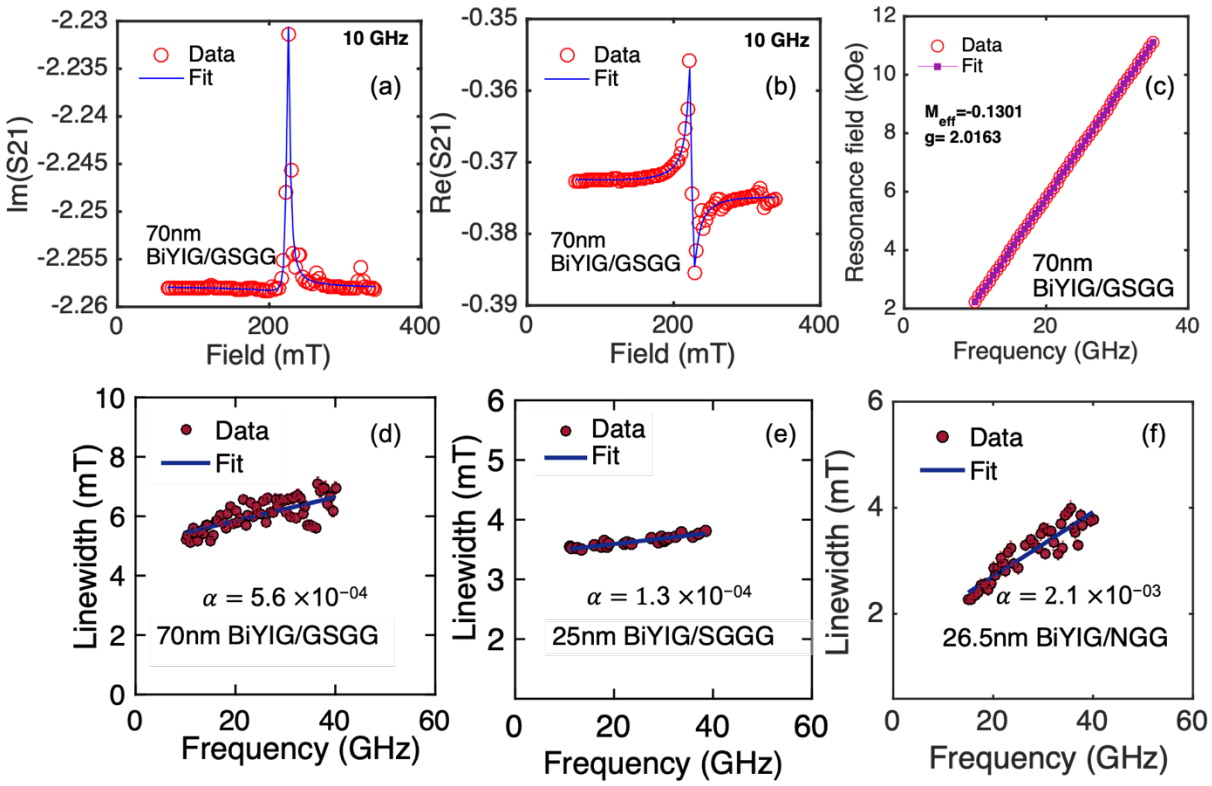

Figure. 6-6: *Representative FMR spectra taken at 10GHz showing the (a) imaginerary and (b) the real part of S_{21} for a 70nm BiYIG thin film grown on GSGG. (c) Representative fit of the resonant field, H_{res} , versus frequency for same film. FMR linewidth, ΔH, as a function of frequency for (d) 70nm BiYIG on GSGG, (e) 25nm BiYIG on SGGG and (f) 23nm BiYIG on NGG.*

6.4 Spintronic interface properties BiYIG/Pt heterostructures

Spin mixing conductance is the parameter that characterizes the transparency of a magnetic insulator (MI)|heavy metal (HM) interface to the flow of spin current through it. The flow of charge current through a HM layer generates a spin current perpendicular to it due to spin-Hall effect (SHE). This spin current gets partially reflected at the MI|HM interface based on the relative orientation of polarization of SHE induced spin current (σ) and magnetization of MI (m). The real component of spin mixing conductance $G_r^{\uparrow\downarrow}$ is associated with damping-like torque which is proportional to m × (σ × m) and the imaginary component of spin mixing conductance $G_i^{\uparrow\downarrow}$ is associated with field-like torque which is proportional to σ × m [50,51]. The reflected spin current produces charge current in the HM layer due to inverse spin-Hall effect (ISHE) and thus modulates the resistance of the HM layer. The resulting magnetoresistance with a symmetry different from that of anisotropic magnetoresistance is called SMR. Longitudinal and transverse components of SMR are given by the following equations [52,53]:

$$R = R_0 + \Delta R^{SMR} sin^2\theta \; sin^2\phi \qquad (2)$$

$$R_H = R_H^{SMR} sin^2\theta \sin 2\phi + R_H^{AHE,SMR} \cos\theta + R_H^{OHE} H_z \qquad (3)$$

Here R_0 is the m independent longitudinal resistance of the HM layer and ΔR^{SMR} is its modulation due to SMR. R_H^{SMR} and $R_H^{AHE,SMR}$ are transverse components of SMR and anomalous Hall effect (AHE)-like SMR respectively. R_H^{OHE} is the contribution from ordinary Hall effect of heavy metal and H_z is the out-of-plane magnetic field. The polar angle θ and azimuthal angle φ are shown in Fig. 6-7(a) along with a schematic of experimental setup used for SMR measurement. SMR measurements were performed to characterize the spin transport properties of Bi-YIG/Pt interface. Pt was used as the HM layer due to its low resistivity and strong spin-orbit interaction and spin-Hall angle which enable efficient conversion of charge current to spin current and vice versa. NGG(111)/Bi-YIG(4.3 nm)/Pt(4 nm) heterostructure was patterned into hall cross devices and a probe station was used to perform transverse SMR measurements with out-of-plane magnetic field. Hall resistance for the sample extracted from a hall cross device for an out-of-plane field sweep from -150 Oe to +150 Oe is shown in Fig.

6-7(a) & (b) after subtraction of a sample dependent offset and linear OHE signal. The loop shows 100% remanence which agrees with robust PMA observed from out-of-plane VSM measurements performed before patterning. Sharp switching can be observed with a coercivity of 30 ± 5 Oe. The difference between the coercivity before and after patterning of thin film sample may be attributed to geometrical effect associated with patterning. We obtained the values of $R_H^{AHE,SMR}$ = -0.86 mΩ and R_H^{OHE} = -10.7 mΩ T^{-1} which gives $\rho_{xy}^{AHE,SMR}$ = -3.44 × 10^{-4} μΩ cm and ρ_{xy}^{OHE} = -4.28 × 10^{-3} μΩ cm T^{-1}. The value of $\rho_{xy}^{AHE,SMR}$ obtained in this work is three times that reported for TmIG/Pt [11] from which we can deduce that it is likely to have better spin mixing conductance than TmIG/Pt. The maximum magnitude of magnetic field available in the probe station was 1000 Oe which was not sufficient to saturate the film in-plane. Thus, we were not able to perform in-plane SMR measurements.

According to model of Chen et al for spin mixing conductance [54]:

$$\frac{\rho_{xy}^{SMR}}{\rho_{xx}^{Pt}} = \frac{\theta_{SH}^2 \lambda_{Pt}}{d_N} \frac{2\lambda_{Pt} G_r \tanh^2 \frac{d_N}{2\lambda_{Pt}}}{\sigma_{xx}^{Pt} + 2\lambda_{Pt} G_r \coth \frac{d_N}{2\lambda_{Pt}}} \quad (4)$$

$$\frac{\rho_{xy}^{AHE,SMR}}{\rho_{xx}^{Pt}} = \frac{2\theta_{SH}^2 \lambda_{Pt}^2}{d_N} \frac{\sigma_{xx}^{Pt} G_i \tanh^2 \frac{d_N}{2\lambda_{Pt}}}{(\sigma_{xx}^{Pt} + 2\lambda_{Pt} G_r \coth \frac{d_N}{2\lambda_{Pt}})^2} \quad (5)$$

Here ρ_{xy}^{SMR} and $\rho_{xy}^{AHE,SMR}$ are Hall resistivities due to SMR and AHE-like SMR respectively, ρ_{xx}^{Pt} (σ_{xx}^{Pt}) is resistivity (conductivity) of Pt determined from longitudinal measurement on Hall bar device, θ_{SH} is the spin-Hall angle of Pt, λ_{Pt} is the spin diffusion length in Pt, d_N is the thickness of the Pt layer and G_r and G_i are real and imaginary components of spin mixing conductance respectively. Without being able to achieve in-plane saturation for the film we cannot obtain ρ_{xy}^{SMR} and hence G_r. However, $\lambda_{Pt} G_r$ is generally much lower than σ_{xx}^{Pt} [55,56]. Thus, if we drop G_r in the denominator of the second equation, we can obtain a lower bound for G_i. Inserting ρ_{xx}^{Pt} = 47.1 μΩ cm, θ_{SH} = 0.08 [57], λ_{Pt} = 1.4 nm [54] and d_N = 4 nm for the Pt layer we obtain a lower bound for Gi equal to 3.1 × 10^{12} Ω^{-1} m^{-2}. This value is comparable to previous results reported for several REIG/Pt interfaces [55] and indicates efficient transport of spin angular moment at Bi-YIG/Pt interface.

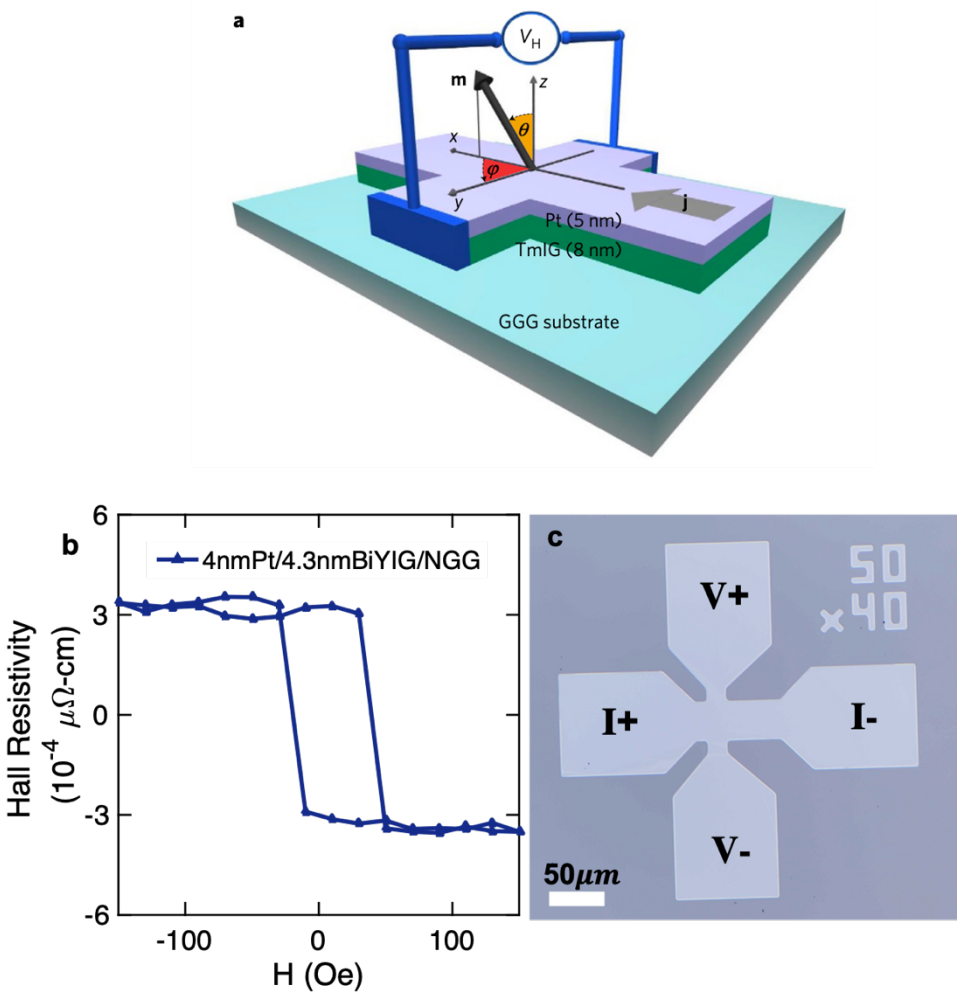

Figure 6-7: *a) Hall device schematic showing the coordinate systems angles θ and φ [58] b) Anomalous Hall effect (AHE)-like spin Hall magnetoresistance (SMR) hysteresis loops for NGG(111)\|Bi-YIG(4.3 nm)/Pt(4 nm) heterostructure. c) Optical micrograph of a representative Hall cross device used to measure SMR.*

6.5 Exceptionally high spin orbit torque driven domain wall velocities in BiYIG films

In iron garnets like thulium iron garnet (TmIG), DWs in Pt/TmIG bilayers can be translated by current even when there is no applied field [58]. This is because the DWs in TmIG have Néel character. The spin current from Pt acts on DWs but only if the DW has Néel character. If the current pushes all the DWs the same way, we deduce they are homochiral Néel walls. This implies there is a Dyaloshinskii-Moriya interaction as discussed in section 2.3.3. However, in pure BiYIG films due to a lack of rare-earth iron cations there is no DMI, and the equilibrium domain wall orientation is purely Bloch as shown in Figure 6-8a. As a result, the DWs in pure BiYIG/Pt films cannot be driven solely by current injection through Pt. However, application of an in-plane biased field induces Néel character (Fig. 6-8b) and allows exceptionally high current driven motion as large as 4300m/s as shown in Fig. 6-8d. This DW velocity approaches a theoretical maximum that is limited by magnon group velocity. This is 5 times higher compared to the 800m/s velocity reported in TmIG/Pt making BiYIG a very promising material for spintronics.

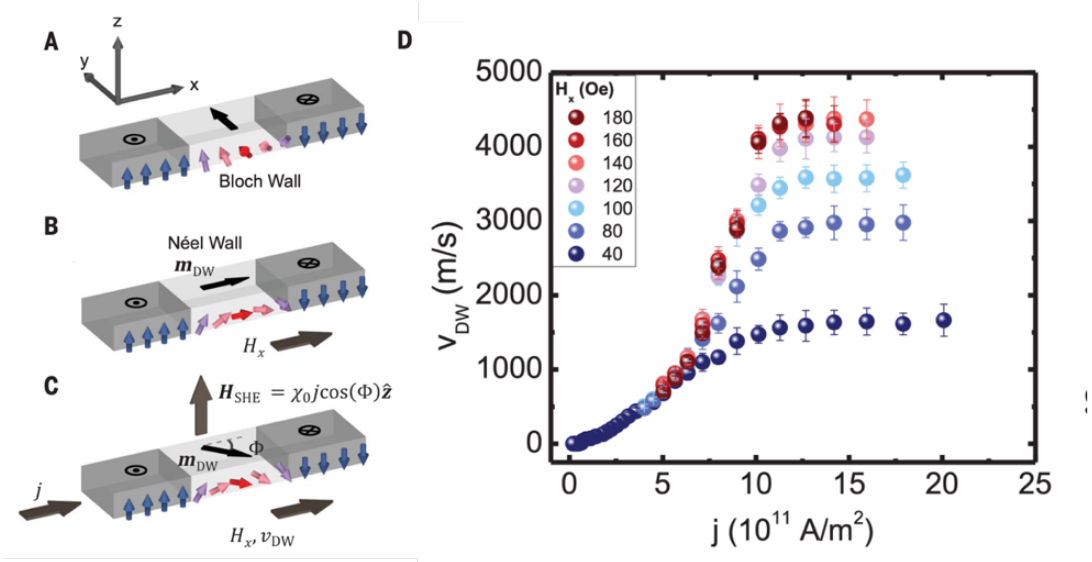

Figure 6-8: *A) Schematic of the equilibrium domain wall structure in GSGG/BiYIG(6.9 nm)/Pt(4.0 nm).* ***B)*** *Domain wall moment* $\mathbf{m}_{DW}$ *under an applied*

longitudinal in-plane field $\boldsymbol{H_x\hat{x}}$ *which forces Neel configuration.* ***C)*** *Equilibrium domain wall orientation* Φ *when traveling at velocity* v_{DW} *under applied* $\boldsymbol{H_x\hat{x}}$ *and driven by* $\boldsymbol{H_{SHE}} = \chi_0 j \cos\Phi\, \hat{\mathbf{z}}$. ***D)*** *Domain wall velocity* v_{DW} *versus current density j for various* H_x. *Error bars represent the standard deviation of three independent measurements of the domain wall velocity. Adapted from reference [23].*

6.6 Spin-wave driven domain wall motion for spin wave-based computing

Spin wave-based computing uses spin wave propagation for information processing and has garnered a lot of interest recently as a potential low-power computing alternative for conventional CMOS technology [59]. Most of the reported work on spin wave-based computing for logic relies on the interference of spin waves and modulating the spin wave amplitude or phase to encode information [60-62]. One way to modulate the spin wave is to use magnetic domain walls [59,63,64]. Recently, Han et al. shows that in Co/Ni PMA when spin waves were transmitted through a domain wall the amplitude was decreased ~20x and there was a phase shift close to 180° [65]. Magnetic metals are unfortunately not the optimal material for spin wave devices because of their large damping. YIG, while has the lowest reported damping does not have PMA to sustain stable magnetic DWs. BiYIG, is an ideal material because it has both low damping and PMA.

17 nm PMA BiYIG films are patterned to create spin wave transmission devices. The device consisted of a magnetic wire with 10 nm Ti/100 nm Cu/20 nm Au antennas deposited on top. A domain wall was nucleated by application of a small out-of-plane field between the two antennas as shown Fig.6-9a. It was observed that spin waves can drive domain walls when the frequency matched the resonant frequency of the channel, visible using MOKE as shown in Fig. 6-9b,c. The was no DW motion for 2GHz spin waves. This makes way for promising opportunities for use of garnets in logic devices as well.

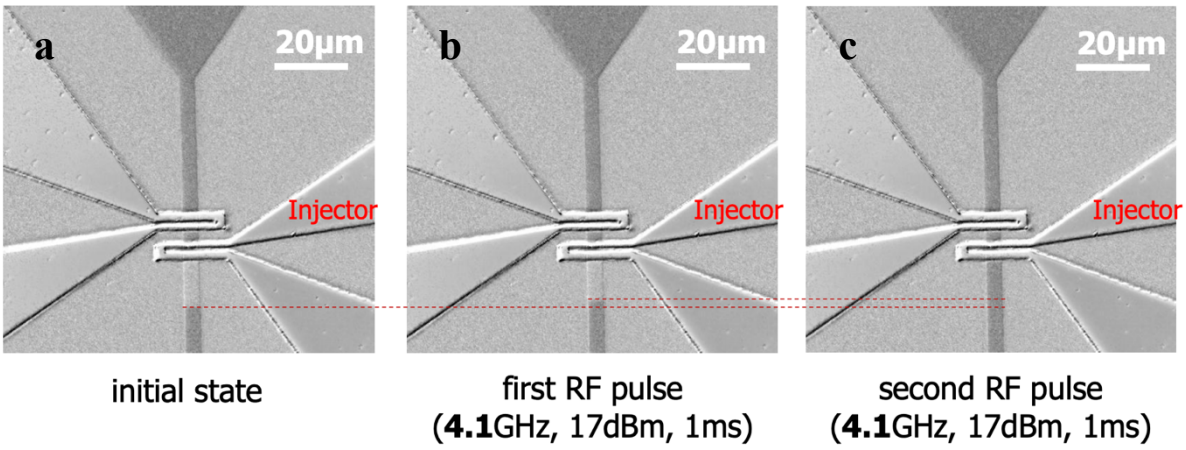

Figure 6-9: *MOKE images of a) domain wall nucleated between antennas on track b) After applying first 1ms RF pulse c) After applying second 1ms RF pulse.*

6.7 Summary

In summary in this work, we report the growth, structural and magnetic characterization of PMA single crystal BiYIG films with thicknesses ranging from 7-70nm. The thinner films under 10nm allow us to demonstrate record current-driven domain wall velocities of up to 4.3 km/s [23] . The equilibrium domains and reversal characteristics of the films show that while majority of the films reverse by nucleation of labyrinth domain walls, in BiYIG/GSGG films that have larger β and possibly larger amount of dislocation defects, the films reverse by nucleation of triangular domains. FMR characterization reveals a record low damping of 1.3×10^{-4} with a linewidth as small as 3.4 mT. We also report a lower bound for the spin mixing conductance is reported which is in par with previous reports for PMA rare earth iron garnets. The PMA BiYIG grown in this work has demonstrated not only record field-driven DW velocities but also can be driven by spin waves making it a promising candidate for both spintronic memory and spin-wave based logic devices.

References

[1] Mangin, S., Ravelosona, D., Katine, J.A., Carey, M.J., Terris, B.D. and Fullerton, E.E., 2006. Current-induced magnetization reversal in nanopillars with perpendicular anisotropy. *Nature materials*, *5*(3), pp.210-215.

[2] Beaujour, J.M., Ravelosona, D., Tudosa, I., Fullerton, E.E. and Kent, A.D., 2009. Ferromagnetic resonance linewidth in ultrathin films with perpendicular magnetic anisotropy. *Physical Review B*, *80*(18), p.180415.

[3] Sbiaa, R., Meng, H. and Piramanayagam, S.N., 2011. Materials with perpendicular magnetic anisotropy for magnetic random access memory. *physica status solidi (RRL)–Rapid Research Letters*, *5*(12), pp.413-419.

[4] Sander, D., Valenzuela, S.O., Makarov, D., Marrows, C.H., Fullerton, E.E., Fischer, P., McCord, J., Vavassori, P., Mangin, S., Pirro, P. and Hillebrands, B., 2017. The 2017 magnetism roadmap. *Journal of Physics D: Applied Physics*, *50*(36), p.363001.

[5] Vedmedenko, E.Y., Kawakami, R.K., Sheka, D.D., Gambardella, P., Kirilyuk, A., Hirohata, A., Binek, C., Chubykalo-Fesenko, O., Sanvito, S., Kirby, B.J. and Grollier, J., 2020. The 2020 magnetism roadmap. *Journal of Physics D: Applied Physics*, *53*(45), p.453001

[6] Mangin, S., Henry, Y., Ravelosona, D., Katine, J.A. and Fullerton, E.E., 2009. Reducing the critical current for spin-transfer switching of perpendicularly magnetized nanomagnets. *Applied Physics Letters*, *94*(1), p.012502.

[7] Shaw, J.M., Nembach, H.T. and Silva, T.J., 2011. Damping phenomena in Co90Fe10/Ni multilayers and alloys. *Applied Physics Letters*, *99*(1), p.012503.

[8] Yang, S.H., Ryu, K.S. and Parkin, S., 2015. Domain-wall velocities of up to 750 m s– 1 driven by exchange-coupling torque in synthetic antiferromagnets. *Nature nanotechnology*, *10*(3), pp.221-226.

[9] Caretta, L., Mann, M., Büttner, F., Ueda, K., Pfau, B., Günther, C.M., Hessing, P., Churikova, A., Klose, C., Schneider, M. and Engel, D., 2018. Fast current-driven domain walls and small skyrmions in a compensated ferrimagnet. *Nature nanotechnology*, *13*(12), pp.1154-1160.

[10] Ahmed, A.S., Lee, A.J., Bagués, N., McCullian, B.A., Thabt, A.M., Perrine, A., Wu, P.K., Rowland, J.R., Randeria, M., Hammel, P.C. and McComb, D.W., 2019. Spin-Hall topological Hall effect in highly tunable Pt/ferrimagnetic-insulator bilayers. *Nano letters*, *19*(8), pp.5683-5688.

[11] Quindeau, A., Avci, C.O., Liu, W., Sun, C., Mann, M., Tang, A.S., Onbasli, M.C., Bono, D., Voyles, P.M., Xu, Y. and Robinson, J., 2017. Tm3Fe5O12/Pt heterostructures with perpendicular magnetic anisotropy for spintronic applications. *Advanced Electronic Materials*, *3*(1), p.1600376.

[12] Avci, C.O., Rosenberg, E., Caretta, L., Büttner, F., Mann, M., Marcus, C., Bono, D., Ross, C.A. and Beach, G.S., 2019. Interface-driven chiral magnetism and current-driven domain walls in insulating magnetic garnets. *Nature nanotechnology*, *14*(6), pp.561-566.

[13] Bauer, J.J., Rosenberg, E.R. and Ross, C.A., 2019. Perpendicular magnetic anisotropy and spin mixing conductance in polycrystalline europium iron garnet thin films. *Applied Physics Letters*, *114*(5), p.052403.

[14] Ciubotariu, O., Semisalova, A., Lenz, K. and Albrecht, M., 2019. Strain-induced perpendicular magnetic anisotropy and Gilbert damping of Tm 3 Fe 5 O 12 thin films. *Scientific reports*, *9*(1), pp.1-8.

[15]Chang, H., Li, P., Zhang, W., Liu, T., Hoffmann, A., Deng, L. and Wu, M., 2014. Nanometer-thick yttrium iron garnet films with extremely low damping. *IEEE Magnetics Letters*, *5*, pp.1-4.

[16] Serga, A.A., Chumak, A.V. and Hillebrands, B., 2010. YIG magnonics. *Journal of Physics D: Applied Physics*, *43*(26), p.264002.

[17] Fu, J., Hua, M., Wen, X., Xue, M., Ding, S., Wang, M., Yu, P., Liu, S., Han, J., Wang, C. and Du, H., 2017. Epitaxial growth of Y3Fe5O12 thin films with perpendicular magnetic anisotropy. *Applied Physics Letters*, *110*(20), p.202403.

[18] Ding, J., Liu, C., Zhang, Y., Erugu, U., Quan, Z., Yu, R., McCollum, E., Mo, S., Yang, S., Ding, H. and Xu, X., 2020. Nanometer-thick yttrium iron garnet films with perpendicular anisotropy and low damping. *Physical Review Applied*, *14*(1), p.014017.

[19] Soumah, L., Beaulieu, N., Qassym, L., Carrétéro, C., Jacquet, E., Lebourgeois, R., Youssef, J.B., Bortolotti, P., Cros, V. and Anane, A., 2018. Ultra-low damping insulating magnetic thin films get perpendicular. *Nature communications*, *9*(1), pp.1-6.

[20] Lin, Y., Jin, L., Zhang, H., Zhong, Z., Yang, Q., Rao, Y. and Li, M., 2020. Bi-YIG ferrimagnetic insulator nanometer films with large perpendicular magnetic anisotropy and narrow ferromagnetic resonance linewidth. *Journal of Magnetism and Magnetic Materials*, *496*, p.165886.

[21] Nembach, H.T., Silva, T.J., Shaw, J.M., Schneider, M.L., Carey, M.J., Maat, S. and Childress, J.R., 2011. Perpendicular ferromagnetic resonance measurements of damping and

Land e ´ g– factor in sputtered (Co 2 Mn) 1– x Ge x thin films. *Physical Review B*, *84*(5), p.054424.

[22] Chen, H., De Gasperis, P., Marcelli, R., Pardavi-Horvath, M., McMichael, R. and Wigen, P.E., 1990. Wide-band linewidth measurements in yttrium iron garnet films. *Journal of applied physics*, *67*(9), pp.5530-5532.

[23] Caretta, L., Oh, S.H., Fakhrul, T., Lee, D.K., Lee, B.H., Kim, S.K., Ross, C.A., Lee, K.J. and Beach, G.S., 2020. Relativistic kinematics of a magnetic soliton. *Science*, *370*(6523), pp.1438-1442.

[24] Adachi, N., Denysenkov, V.P., Khartsev, S.I., Grishin, A.M. and Okuda, T., 2000. Epitaxial Bi 3 Fe 5 O 12 (001) films grown by pulsed laser deposition and reactive ion beam sputtering techniques. *Journal of Applied Physics*, *88*(5), pp.2734-2739.

[25] Fakhrul, T., Tazlaru, S., Beran, L., Zhang, Y., Veis, M. and Ross, C.A., 2019. Magneto-optical Bi: YIG films with high figure of merit for nonreciprocal photonics. *Advanced Optical Materials*, *7*(13), p.1900056.

[26] Khurana, B., Bauer, J.J., Zhang, P., Safi, T., Chou, C.T., Hou, J.T., Fakhrul, T., Fan, Y., Liu, L. and Ross, C.A., 2021. Magnetism and spin transport in platinum/scandium-substituted terbium iron garnet heterostructures. *Physical Review Materials*, *5*(8), p.084408.

[27] Hansen, P., Witter, K. and Tolksdorf, W., 1983. Magnetic and magneto-optic properties of lead-and bismuth-substituted yttrium iron garnet films. *Physical Review B*, *27*(11), p.6608.

[28] Callen, H. On growth-induced anisotropy in garnet crystals. Mater. Res. Bull. 6, 931–938 (1971).

[29] Wolfe, R., LeCraw, R. C., Blank, S. L. & Pierce, R. D. Growth-Induced Anisotropy in Bubble Garnet Films Containing Calcium. in AIP Conf. Proc 34, 172–174 (1976).

[30] Hansen, P., Klages, C.-P., Schuldt, J. & Witter, K. Magnetic and magneto-optical properties of bismuth-substituted lutetium iron garnet films. Phys. Rev. B 31, 5858–5864 (1985).

[31] Fratello, V. J., Slusky, S. E. G., Brandle, C. D. & Norelli, M. P. Growth-induced anisotropy in bismuth: Rare-earth iron garnets. J. Appl. Phys. 60, 2488–2497 (1986).

[32] Callen, H., 1971. Growth-induced anisotropy by preferential site ordering in garnet crystals. *Applied Physics Letters*, *18*(7), pp.311-313.

[33] Gyorgy, E. M., Rosencwaig, A., Blount, E. I., Tabor, W. J. & Lines, M. E. General conditions for growth-induced anisotropy in garnets. Appl. Phys. Lett. 18,479–480 (1971).

[34] Hansen, P., Klages, C. -P. & Witter, K. Magnetic and magneto-optic properties of praseodymium- and bismuth-substituted yttrium iron garnet films. J. Appl. Phys. 60, 721–727 (1986).

[35] Vedmedenko, E.Y., Kubetzka, A., Von Bergmann, K., Pietzsch, O., Bode, M., Kirschner, J., Oepen, H.P. and Wiesendanger, R., 2004. Domain wall orientation in magnetic nanowires. *Physical review letters*, *92*(7), p.077207.

[36] Moon, K.W., Choi, J.W., Kim, C., Yoon, J., Kim, D.O., Song, K.M., Chun, B.S., Kim, D. and Hwang, C., 2018. Triangular and Sawtooth Magnetic Domains in Measuring the Dzyaloshinskii-Moriya Interaction. *Physical Review Applied*, *10*(6), p.064014.

[37] Fratello, V.J., Licht, S.J., Brandle, C.D., O'Bryan, H.M. and Baiocchi, F.A., 1994. Effect of bismuth doping on thermal expansion and misfit dislocations in epitaxial iron garnets. *Journal of crystal growth*, *142*(1-2), pp.93-102.

[38] Machida, K. and Asahara, Y., 1987. Growth of Bi-substituted garnet thick epitaxial films for optical isolators. *Journal of the Magnetics Society of Japan*, *11*(S_1_ISMO), pp.S1_347-351.

[39] Miller, D.C. and Caruso, R., 1974. Stress relief in magnetic garnet films grown by liquid phase epitaxy. *Journal of Crystal Growth*, *27*, pp.274-281.

[40] Van Der Merwe, J.H., 1963. Crystal interfaces. Part ii. Finite overgrowths. *Journal of Applied Physics*, *34*(1), pp.123-127.

[41] Büttner, F., Mawass, M.A., Bauer, J., Rosenberg, E., Caretta, L., Avci, C.O., Gräfe, J., Finizio, S., Vaz, C.A.F., Novakovic, N. and Weigand, M., 2020. Thermal nucleation and high-resolution imaging of submicrometer magnetic bubbles in thin thulium iron garnet films with perpendicular anisotropy. *Physical Review Materials*, *4*(1), p.011401.

[42] Rosenberg, E.R., Litzius, K., Shaw, J.M., Riley, G.A., Beach, G.S., Nembach, H.T. and Ross, C.A., 2021. Magnetic Properties and Growth-Induced Anisotropy in Yttrium Thulium Iron Garnet Thin Films. *Advanced Electronic Materials*, p.2100452.

[43] Nembach, H.T., Silva, T.J., Shaw, J.M., Schneider, M.L., Carey, M.J., Maat, S. and Childress, J.R., 2011. Perpendicular ferromagnetic resonance measurements of damping and Land e ´ g– factor in sputtered (Co 2 Mn) 1– x Ge x thin films. *Physical Review B*, *84*(5), p.054424.

[44] Ding, Y., Klemmer, T.J. and Crawford, T.M., 2004. A coplanar waveguide permeameter for studying high-frequency properties of soft magnetic materials. *Journal of applied physics*, *96*(5), pp.2969-2972.

[45] Neudecker, I., Woltersdorf, G., Heinrich, B., Okuno, T., Gubbiotti, G. and Back, C.H., 2006. Comparison of frequency, field, and time domain ferromagnetic resonance methods. *Journal of Magnetism and Magnetic Materials*, *307*(1), pp.148-156.

[46] Kalarickal, S.S., Krivosik, P., Wu, M., Patton, C.E., Schneider, M.L., Kabos, P., Silva, T.J. and Nibarger, J.P., 2006. Ferromagnetic resonance linewidth in metallic thin films: Comparison of measurement methods. *Journal of Applied Physics*, *99*(9), p.093909.

[47] Nakamura, N., Ogi, H., Hirao, M., Fukuhara, T., Shiroki, K. and Imaizumi, N., 2008. Elastic constants of single-crystal rare-earth bismuth iron garnet films. *Japanese Journal of Applied Physics*, *47*(5S), p.3851.

[48] Wu, C.N., Tseng, C.C., Fanchiang, Y.T., Cheng, C.K., Lin, K.Y., Yeh, S.L., Yang, S.R., Wu, C.T., Liu, T., Wu, M. and Hong, M., 2018. High-quality thulium iron garnet films with tunable perpendicular magnetic anisotropy by off-axis sputtering–correlation between magnetic properties and film strain. *Scientific reports*, *8*(1), pp.1-8.

[49] R. O'Handley, *Modern Magnetic Materials: Principles and Applications*, 1st ed. (Wiley, New York, NY, 1999).

[50] Avci, C.O., Quindeau, A., Pai, C.F., Mann, M., Caretta, L., Tang, A.S., Onbasli, M.C., Ross, C.A. and Beach, G.S., 2017. Current-induced switching in a magnetic insulator. *Nature materials*, *16*(3), pp.309-314.

[51] Garello, K., Miron, I.M., Avci, C.O., Freimuth, F., Mokrousov, Y., Blügel, S., Auffret, S., Boulle, O., Gaudin, G. and Gambardella, P., 2013. Symmetry and magnitude of spin–orbit torques in ferromagnetic heterostructures. *Nature nanotechnology*, *8*(8), pp.587-593.

[52] Hahn, C., De Loubens, G., Klein, O., Viret, M., Naletov, V.V. and Youssef, J.B., 2013. Comparative measurements of inverse spin Hall effects and magnetoresistance in YIG/Pt and YIG/Ta. *Physical Review B*, *87*(17), p.174417.

[53] Vlietstra, N., Shan, J., Castel, V., Van Wees, B.J. and Youssef, J.B., 2013. Spin-Hall magnetoresistance in platinum on yttrium iron garnet: Dependence on platinum thickness and in-plane/out-of-plane magnetization. *Physical Review B*, *87*(18), p.184421.

[54] Chen, Y.T., Takahashi, S., Nakayama, H., Althammer, M., Goennenwein, S.T., Saitoh, E. and Bauer, G.E., 2013. Theory of spin Hall magnetoresistance. *Physical Review B*, *87*(14), p.144411.

[55] Rosenberg, E.R., Beran, L., Avci, C.O., Zeledon, C., Song, B., Gonzalez-Fuentes, C., Mendil, J., Gambardella, P., Veis, M., Garcia, C. and Beach, G.S., 2018. Magnetism and spin transport in rare-earth-rich epitaxial terbium and europium iron garnet films. *Physical Review Materials*, *2*(9), p.094405.

[56] Bauer, J.J., Rosenberg, E.R., Kundu, S., Mkhoyan, K.A., Quarterman, P., Grutter, A.J., Kirby, B.J., Borchers, J.A. and Ross, C.A., 2020. Dysprosium iron garnet thin films with perpendicular magnetic anisotropy on silicon. *Advanced Electronic Materials*, *6*(1), p.1900820.

[57] Liu, L., Moriyama, T., Ralph, D.C. and Buhrman, R.A., 2011. Spin-torque ferromagnetic resonance induced by the spin Hall effect. *Physical review letters*, *106*(3), p.036601.

[58] Avci, C.O., Rosenberg, E., Caretta, L., Büttner, F., Mann, M., Marcus, C., Bono, D., Ross, C.A. and Beach, G.S., 2019. Interface-driven chiral magnetism and current-driven domain walls in insulating magnetic garnets. *Nature nanotechnology*, *14*(6), pp.561-566.

[59] Hämäläinen, S.J., Madami, M., Qin, H., Gubbiotti, G. and van Dijken, S., 2018. Control of spin-wave transmission by a programmable domain wall. *Nature communications*, *9*(1), pp.1-8.

[60] Schneider, T., Serga, A.A., Leven, B., Hillebrands, B., Stamps, R.L. and Kostylev, M.P., 2008. Realization of spin-wave logic gates. *Applied Physics Letters*, *92*(2), p.022505.

[61] Lee, K.S. and Kim, S.K., 2008. Conceptual design of spin wave logic gates based on a Mach–Zehnder-type spin wave interferometer for universal logic functions. *Journal of Applied Physics*, *104*(5), p.053909.

[62]Vogt, K., Fradin, F.Y., Pearson, J.E., Sebastian, T., Bader, S.D., Hillebrands, B., Hoffmann, A. and Schultheiss, H., 2014. Realization of a spin-wave multiplexer. *Nature communications*, *5*(1), pp.1-5.

[63] Serga, A.A., Chumak, A.V. and Hillebrands, B., 2010. YIG magnonics. *Journal of Physics D: Applied Physics*, *43*(26), p.264002.

[64] Hertel, R., Wulfhekel, W. and Kirschner, J., 2004. Domain-wall induced phase shifts in spin waves. *Physical review letters*, *93*(25), p.257202.

[65] Han, J., Zhang, P., Hou, J.T., Siddiqui, S.A. and Liu, L., 2019. Mutual control of coherent spin waves and magnetic domain walls in a magnonic device. *Science*, *366*(6469), pp.1121-1125.

7. Field Free current induced DW motion and Room Temperature Skyrmions in BiYIG-TmIG heterostructures

As discussed in chapter 6, BiYIG films without rare-earth (RE) ions do not have DMI. The main ingredients for interfacial DMI is broken spatial inversion symmetry and strong spin-orbit coupling at the interface. While heavy metal (HM) in thin film bilayers usually provides the spin orbit coupling in HM/RE garnet heterostructures, it has been reported that the critical DMI is provided by the spin orbit coupling of the RE ion [1]. This is also evident from the work of Ding et al. where they observe DMI stabilized skyrmions in TmIG without any Pt capping layer [2]. Caretta et al. [1] also shows that the DMI predominantly comes from garnet/substrate interface and not the HM/garnet interface. This is evident from Fig. 7-1a where introducing a Cu spacer layer between the HM and RE garnet does not negatively impact the DMI strength. Because of the absence of a RE ion providing the critical spin orbit coupling and the fact that Bi^{3+} lacks both spin and orbital angular momentum, pure BiYIG has equilibrium Bloch walls. TmIG on the other hand, having the RE ion Tm^{3+} containing both spin and orbital angular momentum and a significant atomic number can provide the essential spin orbit coupling required for DMI and the formation of equilibrium Néel walls or walls having some Néel character. Hence, DWs in TmIG can be driven with current without the application of an in-plane field as shown in Fig. 7 b and c whereas BiYIG requires an in-plane field to induce Néel character (Fig. 7b, d).

The maximum field-driven DW velocity (V_{DW}) that is attainable in BiYIG is a record 4300m/s at an in-plane field of 160 Oe [4]. This is significantly higher than the current induced V_{DW} in TmIG ranging from 800-1500ms^{-1} [1,5] at current densities of $j = 12 \times 10^{11} - 20 \times 10^{11}Am^{-2}$. In metallic ferrimagnets V_{DW} up to 1300ms^{-1} [6] is reported but at angular compensation temperature of 259K and high current densities of j =20 $\times 10^{11}$Am^{-2}. While the low damping of BiYIG allows it to have very fast DW dynamics, the field driven domain wall motion makes it power inefficient and difficult to implement in applications like racetrack memory as discussed in 2.3.2. To have field-free current driven domain wall motion in BiYIG one would need to stabilize Néel walls in BiYIG. This can be achieved by introducing DMI into BiYIG.

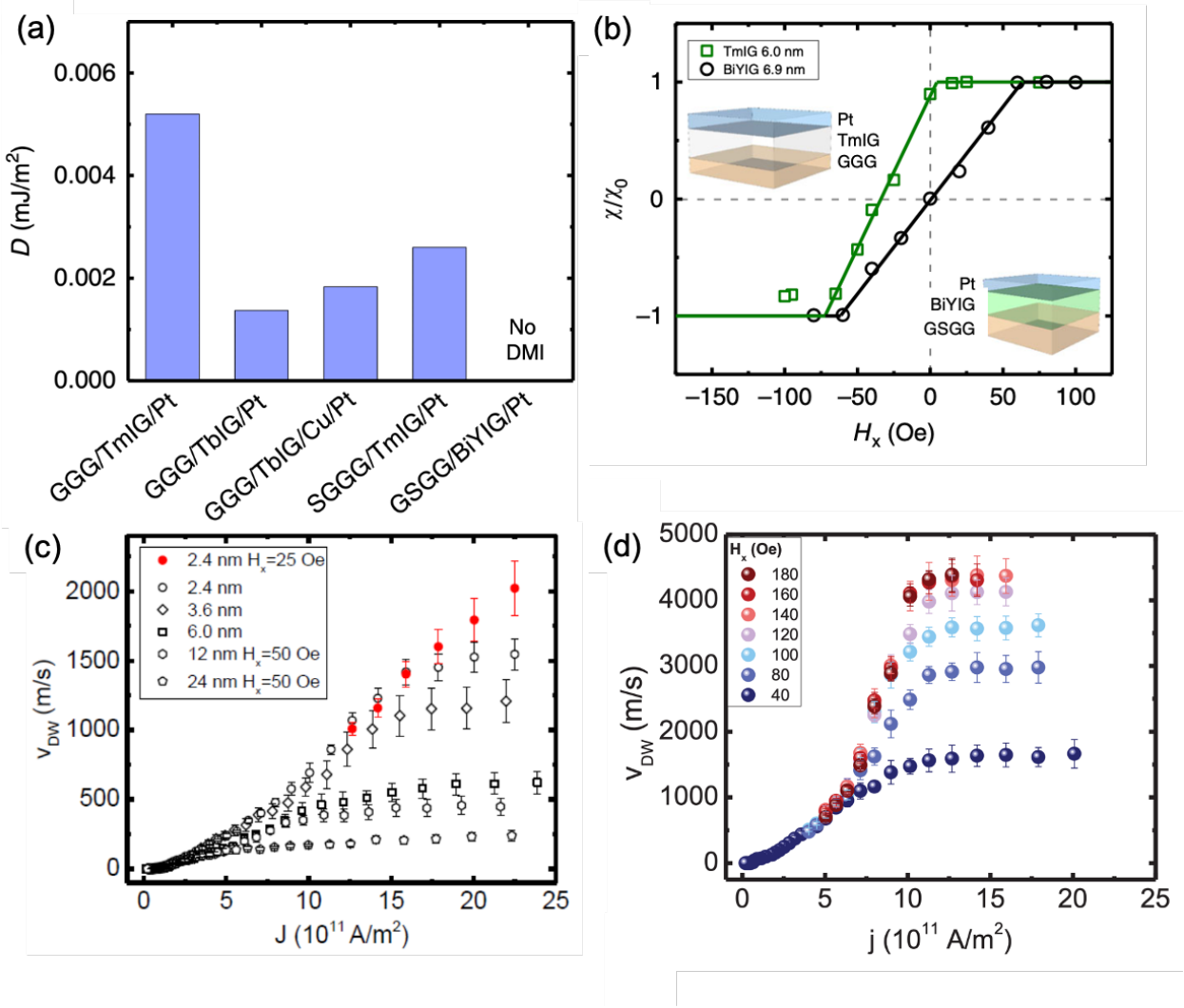

Figure 7-1: *a) Summary of DMI (D) strengths in GGG/TmIG (6.0 nm)/Pt (4.0 nm) , GGG/TbIG (7.1 nm)/Pt (4.0 nm), GGG/TbIG (7.1 nm)/Cu (2.0 nm)/Pt (4.0 nm), SGGG/TmIG (6.0 nm)/Pt (4.0 nm) and GSGG/BiYIG (6.9 nm)/Pt (4.0 nm) [1]. b) Normalized spin Hall efficiency (χ/χ_0) performed on up-down domain walls in GGG/TmIG (6.0 nm)/Pt (4.0 nm) and GSGG/BiYIG (6.9 nm)/Pt (4.0 nm) [1]. C) DW velocity V_{DW} versus current density (j) in TmIG/Pt films. 12 and 24 nm TmIG DWs are Bloch in character, thus an in-plane field is needed to drive them into motion. 2.4, 3.6, and 6.0 nm TmIG films velocity is limited by DMI strength. c) DW velocity V_{DW} versus current density (j) in BiYIG/Pt films that are Bloch in character and thus need in-plane field to drive [3].*

In this chapter we show that DMI can be introduced in BiYIG by making heterostructure of BiYIG and TmIG. In these bilayers, Tm^{3+} would provide the necessary spin orbit coupling required for DMI. Furthermore, the substrate used to provide PMA BiYIG has been GSGG where the RE ion Gd^{3+} has zero orbital magnetism (*l=0)*. In order to study the impact of the RE ion in the substrate on the interfacial DMI we also grow the BiYIG-TmIG heterostructures on NGG substrates where the RE ion Nd^{3+} has non-zero *l*.

The damping of TmIG has been reported to be 0.02 [7-9] which is two orders of magnitude higher than what we have found for BiYIG in this work. Thus, it would be important to strike a balance between introducing just enough Tm^{3+} into BiYIG such that it can stabilize Néel walls while having little impact on the damping of the BiYIG-TmIG heterostructures. After making BiYIG-TmIG bilayers, the damping of the films are measured by FMR and the DMI in the films is measured by BLS as explained in section 3.2.6. 4nm of Pt is then sputter deposited on to the films and they are then patterned into hall crosses and domain wall tracks as explained in section 3.2. The domain wall velocity is them measured by injecting current in the Pt overlayer to study field-free domain wall motion in these heterostructures. In this work we report, the first proof-of-concept of field-free domain wall motion in Pt/BiYIG/TmIG stacks with V_{DW} of 2000m/s. The same film shows room temperature DMI stabilized skyrmions by application of in-plane and out-plane fields.

7.1 Structural and Magnetic characterization

BiYIG-TmIG films of thicknesses below 10 nm were grown by pulsed laser deposition (PLD) on (111) oriented substituted gadolinium gallium garnets of composition $Gd_3Sc_2Ga_3O_{12}$ (GSGG) and $Nd_3Ga_5O_{12}$ (NGG). The targets used for the bilayers and codeposited films had composition of $Bi_{0.8}Y_{2.2}Fe_5O_{12}$ (BiYIG) and $Tm_3Fe_5O_{12}$ (TmIG). The growth conditions were the same used for BiYIG growth as described in section 6.1.

Two kinds of films were grown as shown in Fig. 7-2. One type of film was a codeposition between the BiYIG and TmIG by alternately ablating the targets using 25 laser shots on BiYIG target and between 2-5 laser shots on the TmIG target (Fig 7-2b). The other kind of films were bilayers of interfacial TmIG with a top BiYIG layer as shown in Fig. 7-2c. From the Laue fringes in the HRXRD $2\theta-\omega$ scans in Fig. 7-2 d-e it can be concluded that all the films are of high epitaxial quality growing under in-plane tensile strain. The STEM-EDS mapping of a 3.9nm thickness bilayer film (Fig. 7-3) of BiYIG/BiYIG-TmIG codeposition (25:2 shot ratio)/NGG shows that despite being deposited at the substrate interface only, the Tm^{3+} inter-diffuses through the entire bilayer.

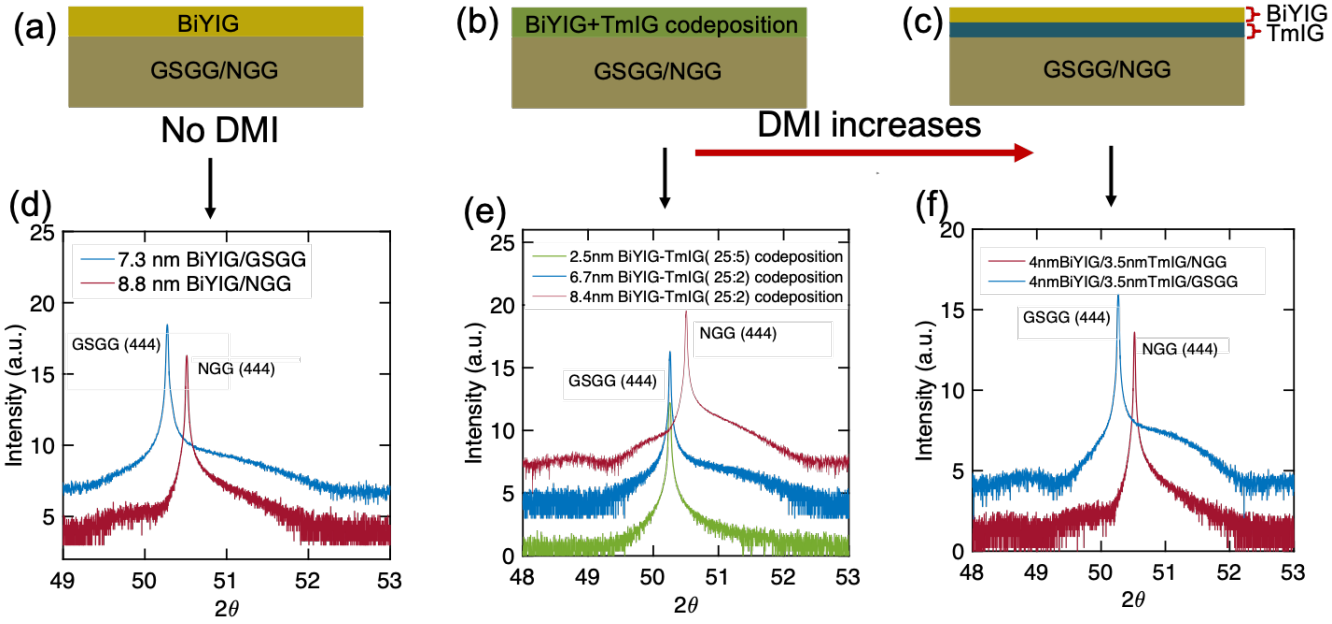

Figure 7-2: *BiYIG-TmIG heterostructures grown in this work are shown here. a) Pure BiYIG grown on NGG/GSGG having no DMI. b) BiYIG-TmIG codeposited films grown by alternatively ablating 25 shots from BiYIG target and 2-5 shots from TmIG. This heterostructure is expected to have little DMI which increases with increasing shots of TmIG. c) Bilayer of TmIG and BiYIG expected to have the most DMI based on the TmIG thickness. (d-e) HRXRD $2\theta-\omega$ scans of the respective films showing high crystal quality. All films are under 10nm in thickness to ensure interfacial DMI.*

The out-of-plane hysteresis loops of selected BiYIG-TmIG bilayers and codeposited films are shown in Fig. 7-4 a-b. The films demonstrate PMA with square hysteresis loops and very low coercivity of less than 5 Oe. The large paramagnetic background signal of the GSGG and NGG and SGGG substrates prevented background subtraction for the in-plane hysteresis loop of the films. The saturation magnetization of BiYIG-TmIG heterostructures was between 80-105kA/m.

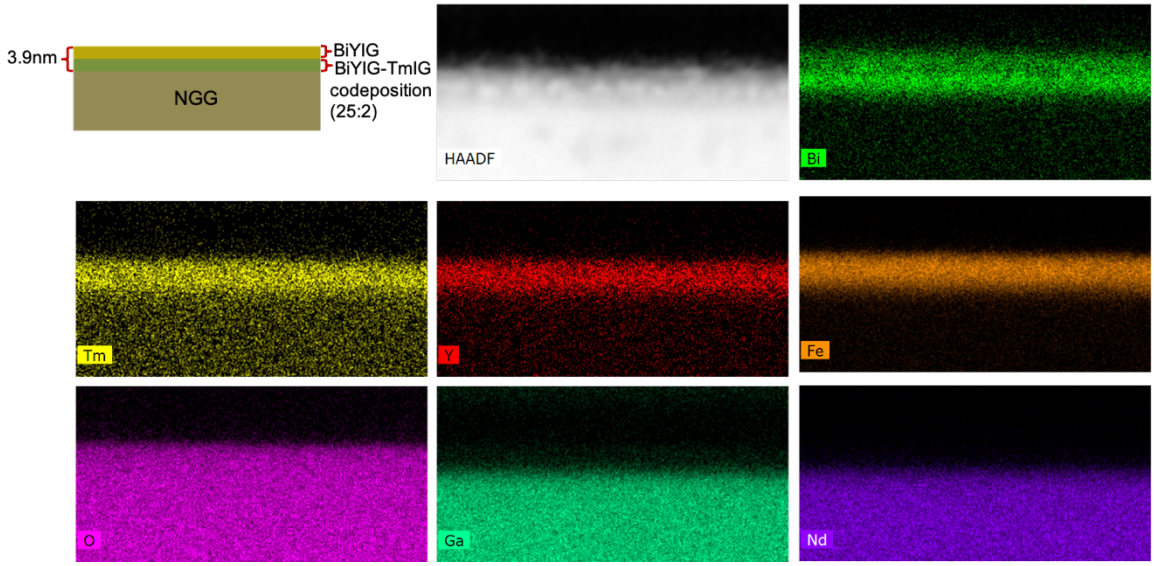

Figure 7-3: *STEM-EDX element mappings of a 3.9nm total thickness bilayer film of BiYIG/BiYIG-TmIG codeposition (25:2 shot ratio)/NGG showing the layer structure qualitatively.*

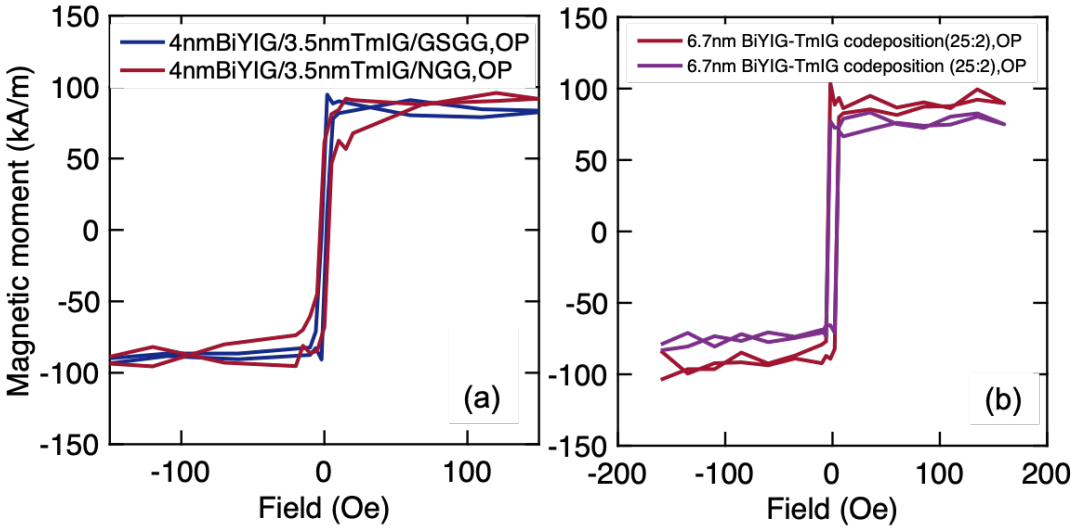

Figure 7-4: *(a) Out-of-plane (OP) VSM hysteresis loops for a) 4nmBiYIG/3.5nmTmIG on GSGG and NGG. (b) 6.7 nm BiYIG-TmIG codeposited films of BiYIG:TmIG shot ratio of 25:2.*

7.2 Ferromagnetic Resonance (FMR) characterization

The damping of a 15.5nmBiYIG/5.6nmTmIG/NGG thin film was measured with broadband perpendicular FMR spectroscopy as discussed in section 6.3. The damping of the film was found to be 5.6×10^{-3} with ΔH_0 of 9.1 mT as shown in Fig.7-5 (a). While this is one order of magnitude higher than what we have obtained for pure BiYIG (Fig. 7-5b), it is still an order of magnitude lower than what has been reported for pure TmIG [7-9] as shown in Fig. 7-5(c). All in all, introducing TmIG increases the damping of BiYIG as expected but the bilayers still have a significant improvement in damping compared to TmIG thus potentially allowing faster DW dynamics in BiYIG/TmIG bilayers compared to pure TmIG as shown in Fig. 7-5 (c-e). The codeposited BiYIG-TmIG films with very little Tm (Laser shot ratio 2:25 for TmIG: BiYIG) have a damping that is almost three time lower than the bilayers which shows that we can tune the damping by controlling the high SOC rare earth ion in the heterostructure films (Fig. 7-5f).

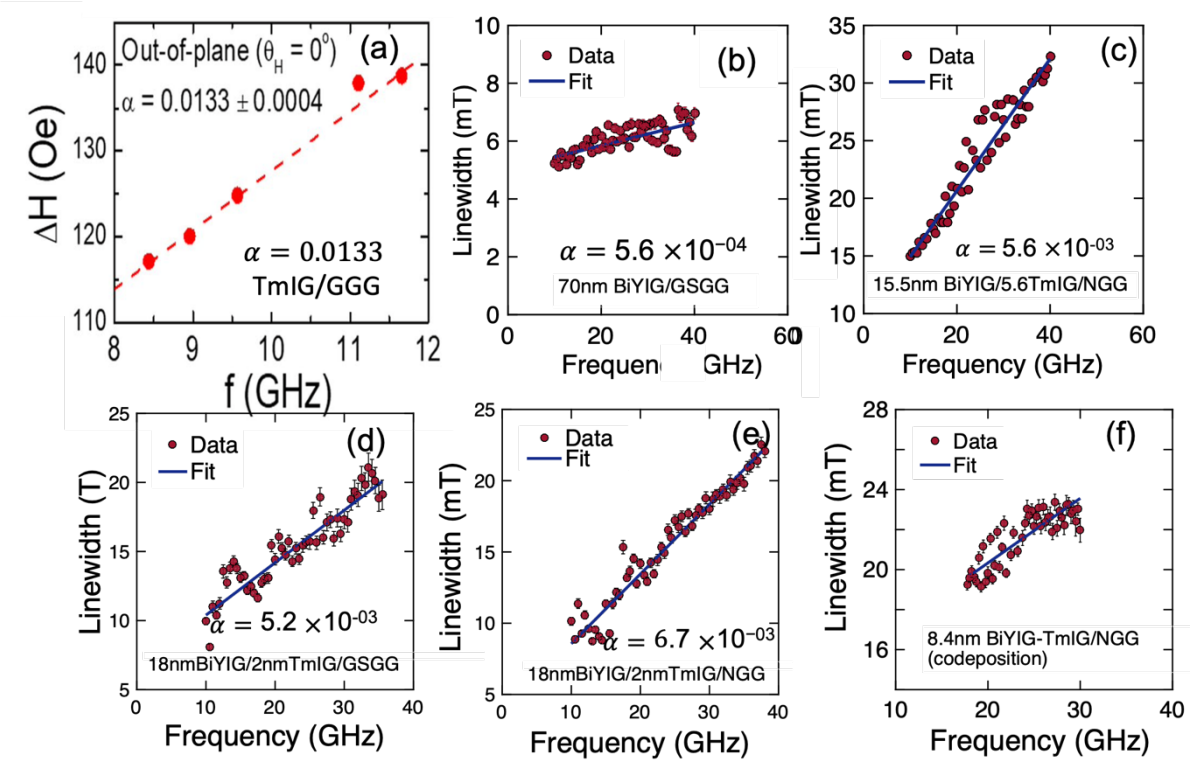

Figure 7-5: *FMR linewidth, ΔH, as a function of frequency for a) TmIG/GGG [8] b) 70nm BiYIG on GSGG and c-e) BiYIG/TmIG bilayers on GSGG and NGG f) BiYIG-TmIG codeposited on NGG.*

7.3 Brillouin light scattering (BLS) for DMI measurement

BLS was used to measure DMI in the BiYIG-TmIG bilayers as discussed in section 3.2.6. From the Δf versus wave vector (k) plots it is clear that BiYIG on either GSGG and NGG has no DMI. However, introducing 1.9nm TmIG at the interface results in a significant amount of DMI due to the strong spin orbit coupling of the Tm^{3+}. The DMI strength of D=0.0145 ± 0.0011 mJ/m^2 obtained for the 6.3 nm BiYIG/TmIG/NGG heterostructure is comparable to the DMI strength reported for Pt/TmIG/GGG in literature [1,2] but less than an order of magnitude lower than metallic ferrimagnetic systems [10] and two orders of magnitude lower than metallic ferromagnetic systems [11,12]. However, an interesting observation is that the RE

ion with non-zero l in the substrate did not contribute to the DMI as is obvious in Fig. 7 a,b. Here, we find $\Delta f = 0$ for both 4.3nm BiYIG/GSGG and 4.3nm BiYIG/NGG indicating that the non-zero l in Nd^{3+} in the substrate has no effect on DMI. It is possible that Nd^{3+} has no effect on the DMI of the stacks as it is in a paramagnetic host that has no magnetic order.

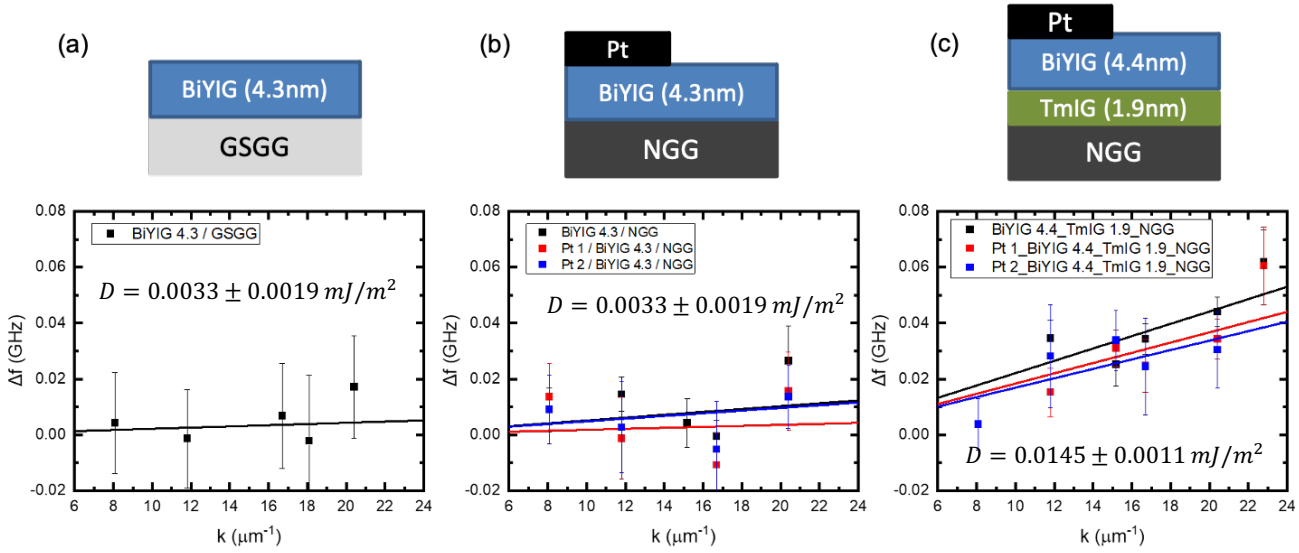

Figure 7-6: *The wave vector (k) versus frequency difference (Δf) for a) 4.3nmBiYIG/GSGG. b) 4.3nmBiYIG/NGG c) 4.4nmBiYIG/1.9nmTmIG/NGG The solid lines are linear fittings.*

7.4 Spintronic interface properties Pt/BiYIG/TmIG heterostructures

SMR measurements were performed to characterize the spin transport properties of the interface of a 4nmPt/4.4nmBiYIG/1.9nmTmIG/NGG film. We speculate the film was in-plane magnetized due to exposure to repeated thermal cycling. The heterostructure was patterned into hall cross devices and a probe station was used to perform transverse SMR measurements with in-plane magnetic field. Hall resistance for the sample was extracted from a hall cross device for a range of φ as defined in Fig. 6-7a. The real part of the spin mixing conductance is calculated from equation 4 in chapter 6 and found to be $G_r = 3.08 \times 10^{13}\ \Omega^{-1}\ m^{-2}$ which is comparable to previous reports for spin mixing conductance of RE iron garnets [13-17]. An important comparison would be that the in-plane SMR amplitude, R_H^{SMR}, is 16mΩ that is twice

that reported for TmIG as shown in Fig. 7-7 a,b. This reinforces that BiYIG-TmIG heterostructures are exciting for spintronic memory applications involving spin-orbit torques.

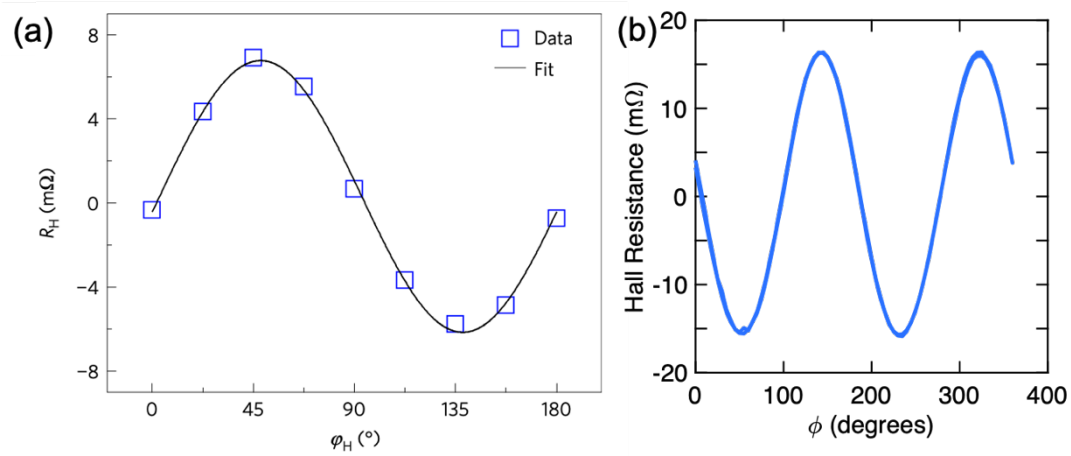

Figure 7-7: *Hall resistivity measurements performed at different φ in a) 5nmPt/8nmTmIG/GGG (111) [9] b) 4nmPt/4.4nmBiYIG/1.9nmTmIG/NGG.*

7.5 Domain wall motion measurements

To measure DW velocity in the Pt/BiYIG-TmIG films, the films are patterned into a domain wall racetrack geometry. The DW is nucleated by spin orbit torque switching by passing 5ms current pulses and an in-plane bias field H_x along the track as shown in Fig. 7-8a. Low duty cycle nano second current pulses were used to drive the nucleated domain walls which also reduces effects of heating of the sample. Fig. 7-7 (b-d) shows DW motion in a 4nm Pt/3.5nm BiYIG/3.1nmTmIG/GSGG stack by the application of an in-plane bias field of H_x=160 Oe and current density of j=10.1× 10^{11} Am^{-2} . For DW velocity measurement, current pulses are applied to drive a domain wall between sets of wide field MOKE image acquisitions. The velocity of the domain wall was determined by dividing the change in the position of the domain wall (as viewed by MOKE) by the duration of the current pulse, $v = \frac{\Delta x}{n t_{pulse}}$ where n is the number of pulses applied. During the measurement shown in Fig. 7-8, t_{pulse} is 1ns. We find

that with 160 Oe in-plane fields, the DW velocities in BiYIG/TmIG stacks are comparable to BiYIG and much higher than pure TmIG as shown in Fig. 7-8 9 (e) , 7-1 (c,d)

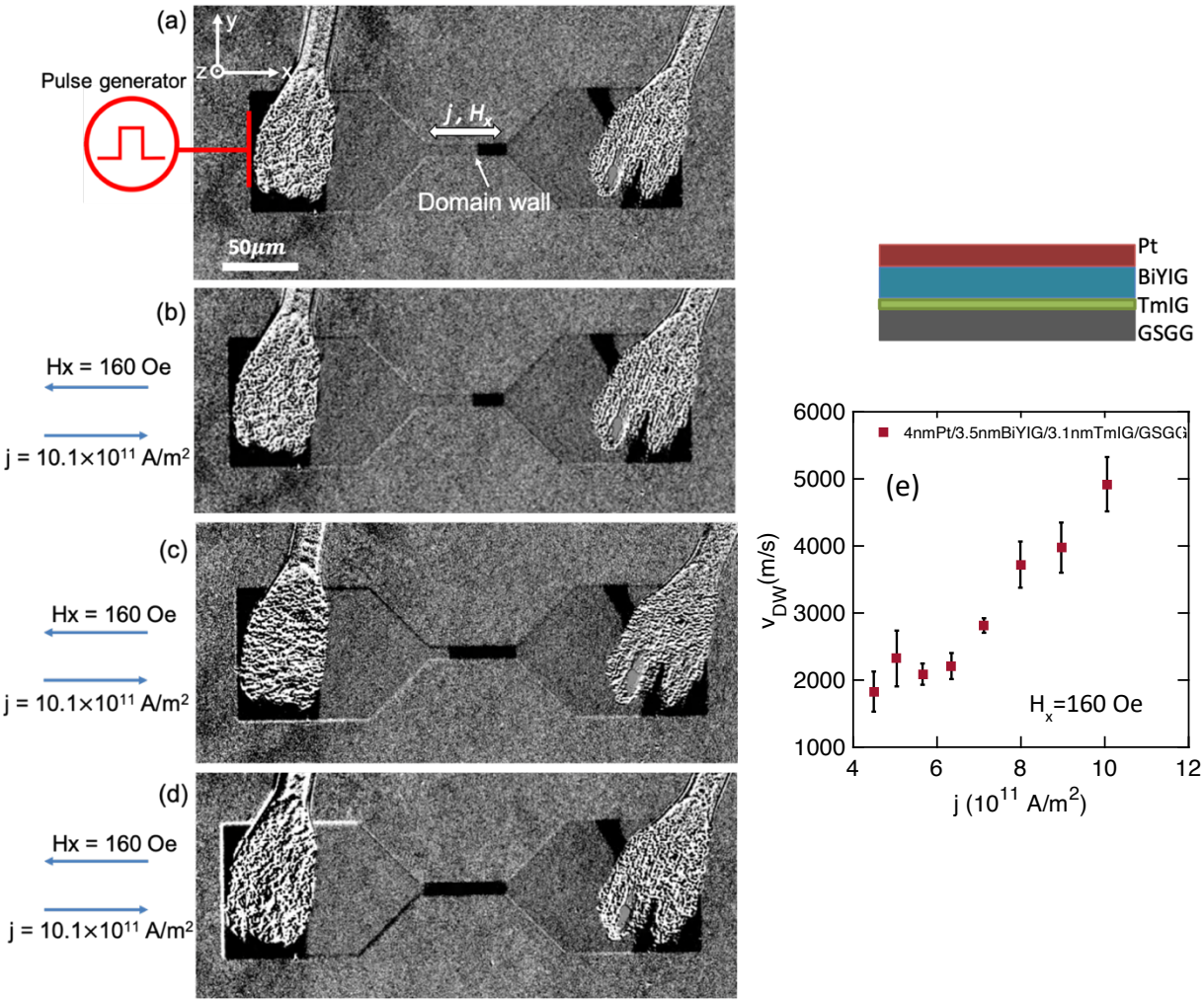

Figure 7-8: *a) MOKE image of a 50 × 10 μm DW track with schematically indicated electrical connections, pulse generator, domain wall and the coordinate system. Black refers to up domain while grey refers to down domain. White arrows show the direction of the DW drive currents and in-plane bias fields. (b-d) MOKE imaged of domain wall motion (by expansion of down domain) after an application of an in-plane bias field of H_x=160 Oe and current density of j=10.1× 10^{11} Am^{-2} in a 4nm Pt/3.5nm BiYIG/3.1nmTmIG/GSGG stack. e) DW velocity V_{DW} versus current density (j) in 4nmPt/3.5nmBiYIG/3.1nmTmIG/GSGG.*

Field-free domain wall motion is observed in a 4nmPt/4nmBiYIG/3.5nmTmIG/GSGG patterned device of dimensions 50 × 20μm track as shown in figure Fig. 7-9c). A current pulse of width 10 ns drives the domain wall about 40 μm corresponding to a speed of 4000m/s at j=8.9× 10^{11} Am^{-2}. This is significantly larger than the field-free DW motion of TmIG [5]. The implications of this is that BiYIG/TmIG heterstructures combining low damping and DMI are extremely promising materials for spintronic applications that require all electrical control and ultra-fast magnetization dynamics.

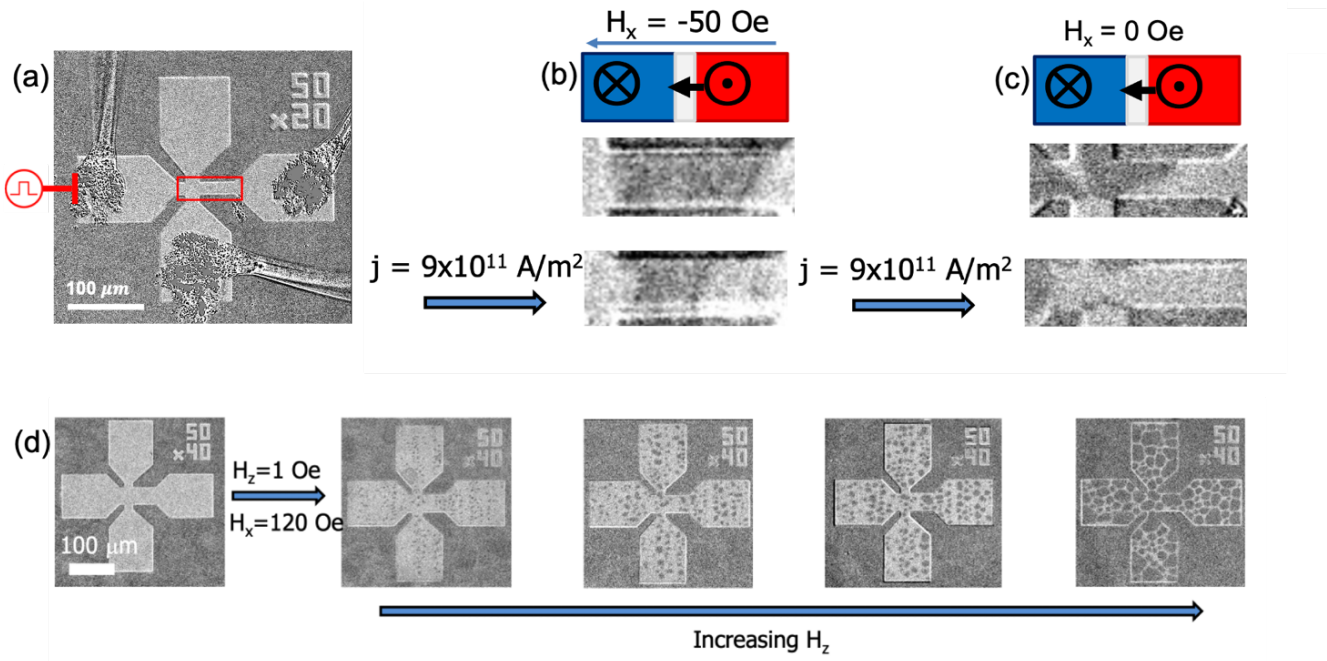

Figure 7-9: *(a) MOKE image of 50 × 20 μm track with the track highlight in the red box. Moke image of domain wall motion in the track after an application of an in-plane bias field and current density of b) H_x=50 Oe , j= 9× 10^{11} Am^{-2} c) H_x=0 Oe , j= 9× 10^{11} Am^{-2}. c) MOKE images of skyrmions nucleation on the same DW track by application of out-f plane (H_z) and in-plane fields (H_x).*

7.6 Room temperature DMI stabilized skyrmions in TmIG/BiYIG/Pt heterostructures

In-plane field was able to trigger room temperature skrymion/bubble nucleation in stacks of 4nmPt/4nmBiYIG/3.5nmTmIG/GSGG. Both in-plane and out-of-plane field were able to tune the skyrmion size over a wide range as shown in Fig. 7-9d and Fig. 7-10. These chiral structures exist below the MOKE resolution (~1μm) and are robust under out-of-plane fields of at least 80 Oe. The existence of skyrmions below 1μm is confirmed by the fact that applying an out-of-plane field to shrink the skyrmions until they are unresolvable followed by the reapplication of H_z in the opposite direction nucleates the skyrmions in the exact position as before. The domain morphology was found to be very sensitive to field magnitude and field sequence. Phase diagram of skyrmion sizes as a function of in-plane and out-of-plane fields is shown in Figure 7-10.

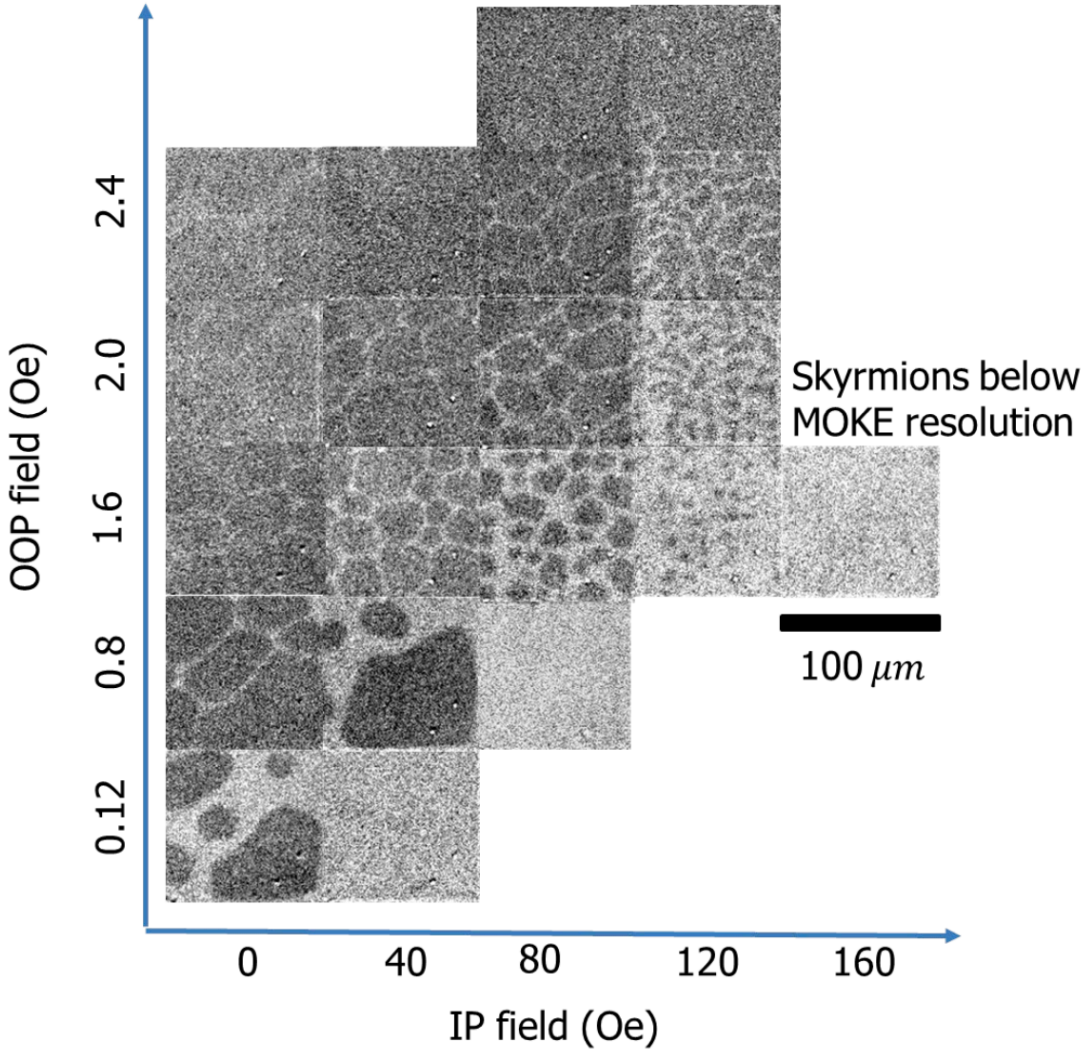

Figure 7-10: *(a) MOKE images of room temperature skyrmion showing their sizes at different out-of-plane (OOP) and in-plane (IP) fields.*

7.7 Summary

In summary, in this chapter we demonstrate that by introducing Tm^{3+} into BiYIG, it is possible to obtain a considerable amount of DMI and stabilize equilibrium walls with enough Néel character to undergo SOT-induced motion. The BiYIG/TmIG stacks also have a damping that is one order of magnitude lower than pure TmIG and also good spin mixing conductance comparable to well-studied RE iron garnets like TmIG. We demonstrate for the first time a proof-of-concept of field-free DW motion in these BiYIG-TmIG heterostructures with much faster DW dynamics that pure TmIG. Finally, we are also able to observe room temperature DMI stabilized skyrmions/bubbles by application of an in-plane field. Low damping, field-free DW motion, fast DW dynamics and the observation of skyrmions in BiYIG/TmIG stacks makes these heterostructures a promising new material for new generation spintronic memory that makes use of spin orbit torque.

References

[1] Caretta, L., Rosenberg, E., Büttner, F., Fakhrul, T., Gargiani, P., Valvidares, M., Chen, Z., Reddy, P., Muller, D.A., Ross, C.A. and Beach, G.S., 2020. Interfacial Dzyaloshinskii-Moriya interaction arising from rare-earth orbital magnetism in insulating magnetic oxides. *Nature communications*, *11*(1), pp.1-9.

[2] Ding, S., Ross, A., Lebrun, R., Becker, S., Lee, K., Boventer, I., Das, S., Kurokawa, Y., Gupta, S., Yang, J. and Jakob, G., 2019. Interfacial Dzyaloshinskii-Moriya interaction and chiral magnetic textures in a ferrimagnetic insulator. *Physical Review B*, *100*(10), p.100406.

[3] Caretta, L.M., 2019. *Chiral spin textures and dynamics in multi-sublattice magnetic materials* (Doctoral dissertation, Massachusetts Institute of Technology).

[4] Caretta, L., Oh, S.H., Fakhrul, T., Lee, D.K., Lee, B.H., Kim, S.K., Ross, C.A., Lee, K.J. and Beach, G.S., 2020. Relativistic kinematics of a magnetic soliton. *Science*, *370*(6523), pp.1438-1442.

[5] Avci, C.O., Rosenberg, E., Caretta, L., Büttner, F., Mann, M., Marcus, C., Bono, D., Ross, C.A. and Beach, G.S., 2019. Interface-driven chiral magnetism and current-driven domain walls in insulating magnetic garnets. *Nature nanotechnology*, *14*(6), pp.561-566.

[6] Caretta, L., Mann, M., Büttner, F., Ueda, K., Pfau, B., Günther, C.M., Hessing, P., Churikova, A., Klose, C., Schneider, M. and Engel, D., 2018. Fast current-driven domain walls and small skyrmions in a compensated ferrimagnet. *Nature nanotechnology*, *13*(12), pp.1154-1160.

[7] Ciubotariu, O., Semisalova, A., Lenz, K. and Albrecht, M., 2019. Strain-induced perpendicular magnetic anisotropy and Gilbert damping of Tm 3 Fe 5 O 12 thin films. *Scientific reports*, *9*(1), pp.1-8.

[8] Crossley, S., Quindeau, A., Swartz, A.G., Rosenberg, E.R., Beran, L., Avci, C.O., Hikita, Y., Ross, C.A. and Hwang, H.Y., 2019. Ferromagnetic resonance of perpendicularly magnetized Tm3Fe5O12/Pt heterostructures. *Applied Physics Letters*, *115*(17), p.172402.

[9] Wu, C.N., Tseng, C.C., Fanchiang, Y.T., Cheng, C.K., Lin, K.Y., Yeh, S.L., Yang, S.R., Wu, C.T., Liu, T., Wu, M. and Hong, M., 2018. High-quality thulium iron garnet films with tunable perpendicular magnetic anisotropy by off-axis sputtering–correlation between magnetic properties and film strain. *Scientific reports*, *8*(1), pp.1-8.

[10] Caretta, L., Mann, M., Büttner, F., Ueda, K., Pfau, B., Günther, C.M., Hessing, P., Churikova, A., Klose, C., Schneider, M. and Engel, D., 2018. Fast current-driven domain walls and small skyrmions in a compensated ferrimagnet. *Nature nanotechnology*, *13*(12), pp.1154-1160.

[11] Woo, S., Litzius, K., Krüger, B., Im, M.Y., Caretta, L., Richter, K., Mann, M., Krone, A., Reeve, R.M., Weigand, M. and Agrawal, P., 2016. Observation of room-temperature magnetic skyrmions and their current-driven dynamics in ultrathin metallic ferromagnets. *Nature materials*, *15*(5), pp.501-506.

[12] Moreau-Luchaire, C., Moutafis, C., Reyren, N., Sampaio, J., Vaz, C.A.F., Van Horne, N., Bouzehouane, K., Garcia, K., Deranlot, C., Warnicke, P. and Wohlhüter, P., 2016. Additive interfacial chiral interaction in multilayers for stabilization of small individual skyrmions at room temperature. *Nature nanotechnology*, *11*(5), pp.444-448.

[13]Avci, C.O., Quindeau, A., Pai, C.F., Mann, M., Caretta, L., Tang, A.S., Onbasli, M.C., Ross, C.A. and Beach, G.S., 2017. Current-induced switching in a magnetic insulator. *Nature materials*, *16*(3), pp.309-314.

[14] Bauer, J.J., Rosenberg, E.R. and Ross, C.A., 2019. Perpendicular magnetic anisotropy and spin mixing conductance in polycrystalline europium iron garnet thin films. *Applied Physics Letters*, *114*(5), p.052403.

[15] Rosenberg, E.R., Beran, L., Avci, C.O., Zeledon, C., Song, B., Gonzalez-Fuentes, C., Mendil, J., Gambardella, P., Veis, M., Garcia, C. and Beach, G.S., 2018. Magnetism and spin transport in rare-earth-rich epitaxial terbium and europium iron garnet films. *Physical Review Materials*, *2*(9), p.094405.

[16] Bauer, J.J., Rosenberg, E.R., Kundu, S., Mkhoyan, K.A., Quarterman, P., Grutter, A.J., Kirby, B.J., Borchers, J.A. and Ross, C.A., 2020. Dysprosium iron garnet thin films with perpendicular magnetic anisotropy on silicon. *Advanced Electronic Materials*, *6*(1), p.1900820.

[17] Khurana, B., Bauer, J.J., Zhang, P., Safi, T., Chou, C.T., Hou, J.T., Fakhrul, T., Fan, Y., Liu, L. and Ross, C.A., 2021. Magnetism and spin transport in platinum/scandium-substituted terbium iron garnet heterostructures. *Physical Review Materials*, *5*(8), p.084408.

8. Conclusions and future work

To facilitate the quest of computing beyond Moore's law, this thesis aims to provide material solutions for both integrated optical isolators and spintronic memory. Listed below are the major advances in terms of material development made in this thesis for integrated non-reciprocal photonic devices and spintronic memory:

1) **Magneto-optical BiYIG films with high figure of merit for nonreciprocal photonics**

Prior work has shown that BiYIG does not crystallize well on a non-garnet substrate, and instead, a thin YIG underlayer is typically used to promote the garnet phase growth. However, this bottom-up crystallization results in a weakly-magnetooptical YIG layer between the waveguide substrate and the Bi:YIG, which is undesirable. We show the first successful demonstration of top-down crystallized polycrystalline BiYIG/YIG films on Si, in which the YIG is placed on top of the BiYIG, allowing greater coupling of light from the underlying waveguide into the BiYIG cladding. As, the figure of merit of MO materials is defined as the ratio of Faraday rotation to optical absorption, therefore developing materials with high Faraday rotation and low optical absorption is critical. We demonstrate the highest reported figure of merit at 1550 nm of 769 $^{\circ}dB^{-1}$ for bottom-up crystallized films and 376$^{\circ}dB^{-1}$ for top-down crystallized films, more than one order of magnitude higher than previous reported FoM values for polycrystalline MO garnets.

Moreover, demonstrate sidewall growth of garnets for TE mode devices for the first time. On-chip lasers produce TE polarized light so it is essential to isolate the TE mode. However, all previous integrated isolator devices have incorporated the MO cladding on the top surface of the waveguide, which isolates the TM mode but has no effect on the TE mode. To create an integrated TE isolator or circulator, the MO material must grown on the sidewall, which presents challenges in terms of ensuring crystallinity, step coverage, and the correct properties.

2) **High FoM magneto-optical seedlayer-free Ce and Bi substituted terbium iron garnet films integrated on Si**

While MO garnets like CeYIG and BiYIG can be crystallized on Si with either a top or bottom weakly-magnetooptical YIG seed layer that reduces device performance. In this work we show that by PLD growth from very precise composition control, we are able to get Faraday rotations as high as +6200deg/cm in BiTbIG which is almost twice that of the previous record held by polycrystalline CeYIG of -3700deg/cm at 1550nm. We demonstrate a way to engineer low optical absorption in these garnets film. Our work shows that by adding Bi and Ce to TbIG we are able to reduce the absorption in these materials dramatically by potentially reducing absorption pathways related to Tb^{4+} and Fe^{2+}.

The FoM at 1550 nm is 720˚dB^{-1} for $Bi_{0.03}$TIG that is in the order of the highest reported so far for BiYIG (769 ˚dB^{-1}) which unfortuantely has a 20nm undesirable bottom seed layer. The high figure of merit and lack of any seed layer needed for crystallization determines the ultimate high performance of MO devices and these results show that BiTbIG and CeTbIG are both enablers for non-reciprocal integrated photonics with enhanced performance.

3) **Ultra-low damping PMA BiYIG films facilitating exceptionally high domain wall motion**

BiYIG films are grown epitaxially on a range of (111) oriented garnet substrates with varying lattice parameters that result in high quality single crystal PMA films due to magnetoelastic and growth induced anisotropy. FMR characterization reveals damping as low as 1.3×10^{-4} with a linewidth as small as 3.4 mT. The ultra-low damping PMA BiYIG allowed the demonstration of record high current induced field-driven domain wall velocities of up to 4.3 km/s . Moreover , we see spin wave driven domain wall motion

making it BiYIG a promising candidate for both spintronic memory and spin-wave based logic devices.

4) **Field-free current induced DW motion and room temperature skyrmions in BiYIG-TmIG heterostructures**

While the low damping of BiYIG allows it to have very fast DW dynamics, it requires an in-plane field to stabilize Néel domain walls, which allow for SOT driven motion. However, field driven DW motion is power inefficient and difficult to implement in applications liken racetrack memory. We show that DMI can be introduced in BiYIG by making heterostructure of BiYIG and TmIG where Tm^{3+} would provide the necessary spin orbit coupling required for DMI and to stabilize Néel walls. In this work we report, the first proof-of-concept of field-free current induced domain wall motion in Pt/BiYIG/TmIG stacks with a velocity of 4000m/s that is similar to velocities in pure BiYIG and higher than pure TmIG. The same film shows room temperature skyrmions by application of in-plane and out-plane fields. This is the first direct observation of skyrmions in magnetic insulators. All of these discoveries make BiYIG-TmIG a very important material for further research and applications in spintronic Néel memory.

While major progress has been made in this thesis in terms of developing high figure of merit magneto-optical materials that can be integrated to CMOS for photonic integrated circuits and also ultra-low damping PMA materials for new generation spintronic memory, there is room for further studies and improvement.

Future materials design for monolithic nonreciprocal photonic

1) BiYIG and Ce and Bi substituted TbIG crystalize on Si at high temperatures which is not compatible with front end or back end of the line CMOS processing. Therefore, the next logical step would be to deposit them at room temperature and then laser anneal on chip in order to reduce the thermal budget and make the process more CMOS compatible. Another option is to use a built-in heater to crystallize. We already have results that show the growth of non-seedlayer BiYIG at room temperature that crystallizes after RTA at 700°C.

2) In terms of composition of the garnets, it would also be interesting to get higher amounts of Bi^{3+} into TbIG in order to lower the optical absorption to as low as BiYIG.
3) BiYIG currently only crystallized with a seed-layer. It would be interesting to try to crystallize BiYIG directly on silicon and be able to crystallize with laser annealing on chip.

Future materials design for magnetic insulators for spintronic memory

1) The field-free domain wall motion was only a proof-of-concept demonstration so more research is needed to optimize the bilayer. Currenly, the BiYIG/TmIG have almost 50% TmIG. In order, to further reduce the damping the TmIG can be reduced to less than 25%, resulting in faster DW dynamics.
2) The skyrmions observed in this work are in the micron range whereas desirable skyrmions for racetrack should be in the nm range (<10nm). By tuning the anisotropy and the composition of the films one can potentially make smaller skyrmions. A full analysis of skyrmion stability and dynamics is needed for garnet parameters of K, M_s, DMI, etc to better understand the physics of their formation as prior work has focused on metallic systems like Co/Pt .
3) The next logical step in terms of skyrmions would be to drive them and measure the speed. This speed is expected to be faster than skyrmion speed in metallic ferrimagnet because of the lower damping in garnets.